NASA CR-159813

NASA

INERT GAS THRUSTERS

Prepared for
LEWIS RESEARCH CENTER
NATIONAL AERONAUTICS AND SPACE ADMINISTRATION
GRANT NSG 3011

Annual Report
November 1979

Harold R. Kaufman and Raymond S. Robinson
Department of Mechanical Engineering
Colorado State University
Fort Collins, Colorado

1. Report No.	2. Government Accession No.	3. Recipient's Catalog No.
CR-159813		

4. Title and Subtitle	5. Report Date
INERT GAS THRUSTERS (U)	November 1979
	6. Performing Organization Code

7. Author(s)	8. Performing Organization Report No.
Harold R. Kaufman and Raymond S. Robinson	
	10. Work Unit No.

9. Performing Organization Name and Address	11. Contract or Grant No.
Department of Mechanical Engineering Colorado State University Fort Collins, Colorado 80523	NSG 3011
	13. Type of Report and Period Covered
12. Sponsoring Agency Name and Address	Contractor Report
National Aeronautics and Space Administration Washington, D.C. 20546	14. Sponsoring Agency Code

15. Supplementary Notes

Grant Manager: William R. Kerslake
NASA Lewis Research Center
Cleveland, Ohio 44135

16. Abstract

Inert gas thrusters are of increasing interest for space propulsion systems. Substantial progress has been made in the understanding of electron diffusion across a magnetic field. The basic model used is a two-step one in which the first step is density-gradient driven. The second step encompasses a potential difference and consists of single-particle escape orbits. If the diffusion is to a region of substantial plasma density, constant density diffusion may be assumed for the second step.

The production of doubly charged ions has been correlated using only overall performance parameters. The use of this correlation is therefore possible in the design stage of large gas thrusters, where detailed plasma properties are not available.

Argon hollow cathode performance was investigated over a range of emission currents, with the positions of the insert, keeper, and anode varied. A general trend observed was that the maximum ratio of emission to flow rate increased at higher propellant flow rates. It was also found that an enclosed keeper enhances maximum cathode emission at high flow rates. The maximum cathode emission at a given flow rate was associated with a noisy high voltage mode. Although this mode has some similarities to the plume mode found at low flows and emissions, it is encountered by being initially in the spot mode and increasing emission. No similar high current mode has been observed with mercury propellant.

A detailed analysis of large, inert-gas thruster performance was carried out, with the results presented in both graphical and tabular form. For maximum thruster efficiency, the optimum beam diameter increases from less than a meter at under 2000 sec specific impulse to several meters at 10,000 sec. The corresponding range in input power ranges from several kilowatts to megawatts.

17. Key Words (Suggested by Author(s))	18. Distribution Statement
Electric Propulsion Ion Beams Ion Sources Plasma Physics	Unclassified - Unlimited

19. Security Classif. (of this report)	20. Security Classif. (of this page)	21. No. of Pages	22. Price*
Unclassified	Unclassified		

* For sale by the National Technical Information Service, Springfield, Virginia 22161

NASA-C-168 (Rev. 10-75)

N80-24362#

TABLE OF CONTENTS

I. INTRODUCTION

Inert gas thrusters are of increasing interest for space propulsion systems. Xenon is of interest in that its physical characteristics are well suited to thruster operation. If a large amount of propellant is required, argon is a more economical alternative.

This report covers the progress made since the last annual report.[1] The progress in the area of electron diffusion across a magnetic field has been particularly impressive, in that many processes can now be calculated that previously were understood in only a qualitative manner. The first section (after the introduction) deals with electron diffusion, and includes a review of work from the previous annual report[1] for completeness. Much of the recent progress in the electron diffusion area was also presented elsewhere.[2]

The next section deals with the production of doubly charged ions. This subject has been studied in a comprehensive manner,[3] but the associated theory was difficult to apply during the design stage due to a requirement for detailed plasma surveys. The theory presented herein is based on the same fundamental processes, but is presented in terms of overall performance parameters that should be readily available, even in the design stage. The work in this section was also presented elsewhere.[2]

The last sections include experimental work on hollow cathodes and a theoretical study of large, inert-gas thruster performance.

II. ELECTRON CONDUCTION ACROSS A MAGNETIC FIELD

A model has been developed to describe electron diffusion across a magnetic field that is driven by both density and potential gradients, with Bohm diffusion[1] used to predict the diffusion rate. This model has applications to conduction across magnetic fields inside a discharge chamber, as well as through a magnetic baffle region[2] used to isolate a hollow cathode from the main discharge chamber. In particular, this model has been applied to conduction across the fringe field near the anodes in a multipole discharge chamber. Single-particle motions appear to be applicable in the region near the anode where the plasma density is reduced and the electron energy increased.

The use of inert gas propellants has been associated recently with the development of the multipole discharge chamber concept.[3-7] The multipole design tends to decouple ion production in the bulk plasma from the current conduction processes taking place in the fringe magnetic fields near the anodes. Primarily, this is because the fringe fields occupy a small part of the total discharge chamber volume. This decoupling of processes facilitates the theoretical analysis of plasma processes in a multipole thruster.

The electron current to discharge chamber anodes is provided by the diffusion of electrons through the magnetic field shielding the anodes. The magnetic field is usually set at a value that will deflect primary electrons back into the discharge chamber, with the primary electron energy assumed to correspond to the discharge potential. The electron current provided by Bohm diffusion can be limited by the strength of the magnetic field above the anode when no appreciable electric fields are

present to enhance conduction. This limiting condition (no appreciable electric fields), is characterized by smaller current densities and is termed density-gradient driven electron diffusion. Operation at higher current densities results in what is termed potential- and density-gradient driven diffusion. The density-gradient electron diffusion was covered initially in the previous annual report on this grant,[8] but is included here for completeness.

Density-Gradient Driven Electron Diffusion

The electron current to a discharge-chamber anode can be limited by the diffusion of electrons through the magnetic field above the anode. This condition can be thought of as either an anode area limitation or a diffusion current limitation to that anode. The current approach is more convenient for derivation of the effect, while considering the area limitation appears to be more useful for discussing experimental performance.

The Bohm electron diffusion is discussed herein primarily in connection with the multipole magnetic field. Bohm diffusion, though, appears to be involved wherever electrons must cross magnetic field lines to reach a discharge-chamber anode.

Before developing the model describing electron diffusion, it should be emphasized that the current collection area involved may, or may not, be a physical area. The electron mobility along magnetic field lines is much greater than the mobility across field lines. The effective area is therefore that area from which electrons can be drained from the discharge plasma by traveling along field lines to reach an anode. This effective area is indicated in Fig. 2-1 for a multipole chamber.

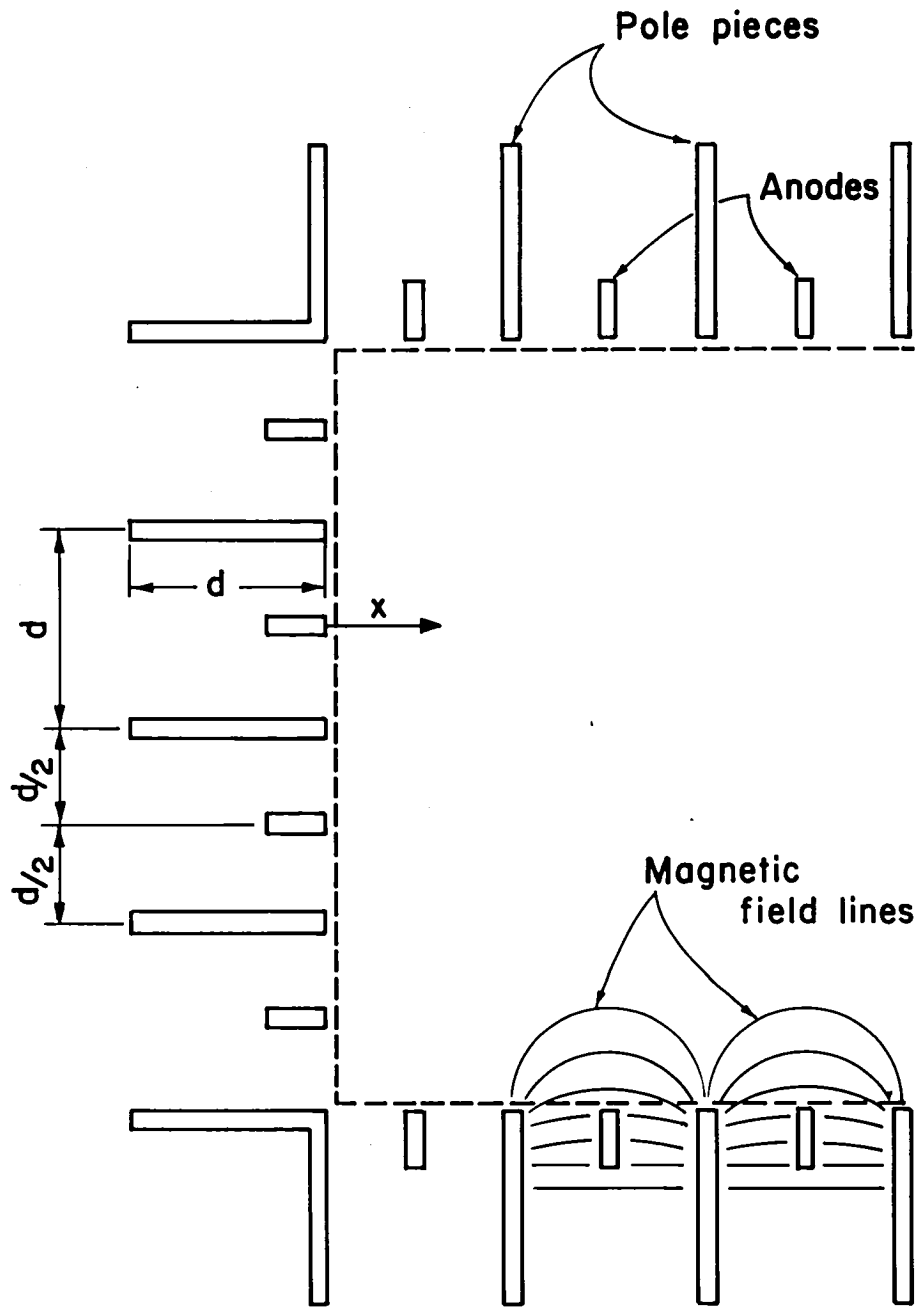

Fig. 2-1. Multipole discharge chamber. Dashed line shows assumed outer surface of discharge chamber.

Electrons emitted from the cathode, together with electrons liberated in the ionization process, must diffuse to the anodes to sustain a discharge. In doing so, the electrons must cross magnetic fields sufficient to contain electrons of primary energy. The basic relation for electron diffusion in the presence of a density gradient is

$$\vec{\Gamma} = - D\vec{\nabla}n_e \tag{2-1}$$

where $\vec{\Gamma}$ represents the particle flux of electrons, n_e is the electron number density, and D is the electron diffusion coefficient. The classical diffusion coefficient in the absence of (or parallel to) a magnetic field is

$$D = kT_e/m_e\nu_e \tag{2-2}$$

with m_e the electron mass and ν_e the electron collision frequency.

The classical diffusion coefficient normal to a magnetic field is

$$D_\perp = D/(1 + \omega^2\tau^2) \tag{2-3}$$

where ω is the electron cyclotron frequency and τ is the mean time between collisions ($\tau = 1/\nu$). This reduces in the strong field limit of $\omega\tau >> 1$ to

$$D_\perp = D/\omega^2\tau^2 = kT_e m_e \nu_e/e^2B^2 \tag{2-4}$$

Experimental measurements of electron diffusion across a magnetic field with $\omega\tau>>1$ usually correspond to larger diffusion coefficients than Eq. 2-4, often by orders of magnitude. These larger values are attributed to "anomalous" or "turbulent" diffusion. A simple and well-known, semiempirical approach to turbulent electron diffusion was given by Bohm.[1] The Bohm diffusion coefficient given in other, later publications[9,10] is

$$D_B = kT_e/16\ eB\ . \tag{2-5}$$

Bohm diffusion is proportional to 1/B, while classical diffusion for the same strong field condition is proportional to $1/B^2$. In fact, the Bohm value of diffusion is obtained if it is assumed that turbulence increases the effective collision frequency to $\omega/16$. Despite the apparent simplicity of the Bohm diffusion coefficient, it effectively correlates experimental observations over a wide range of conditions.[10]

It should be noted that the diffusion of interest herein is primarily of Maxwellian electrons. Whether we are concerned with the Coulomb collisions of classical diffusion or the collective collisions of turbulent diffusion, the lower energy electrons have almost all the collisions, hence diffuse across a magnetic field preferentially compared to higher energy primary electrons.

The diffusion condition for anodes that is under consideration in this section is the maximum diffusion that can be obtained without the assistance of a forward electric field. A reasonable assumption for this limiting condition appears to be zero electric field in the region of

interest close to the anodes of a multipole discharge chamber. This condition of nearly uniform potential in the diffusion region has been observed experimentally.[11] Using the assumption of uniform potential together with the Bohm diffusion coefficient, Eq. (2-1) can be written in one dimension as

$$\Gamma_x = -D_B \, dn_e/dx \; . \tag{2-6}$$

In terms of current density, this becomes

$$j = e \, D_B \, dn_e/dx \; . \tag{2-7}$$

With the substitution of Eq. (2-5), we find

$$j = \frac{kT_e}{16B} \frac{dn_e}{dx} \; . \tag{2-8}$$

Prior knowledge of the variation of n_e with x is not assumed. Instead, continuity of current flow in the diffusion region is used, which results from the small depth of that region compared to chamber diameter and the small fraction of total ionization therein. Noting also that the electron temperature is also nearly constant in the diffusion region,[11] the constants of Eq. (2-8) can be collected on the left side to obtain

$$\frac{16j}{kT_e} = \frac{dn_e}{Bdx} \; . \tag{2-9}$$

Details of the variation of n_e with x are still not known but the

differential expressions can be formally integrated over the diffusion depth to obtain

$$\frac{dn_e}{Bdx} = \frac{n_e}{\int Bdx} \quad , \tag{2-10}$$

where $\int Bdx$ is the same integral that applies to the containment of high-energy primary electrons.[12] With this substitution, the electron current density becomes

$$j = \frac{kT_e n_e}{16 \int Bdx} \cdot \tag{2-11}$$

In calculating this current density, the fringe magnetic field area above the anodes is important, while the projected physical area of the anodes is not. As mentioned earlier, this is because the diffusion coefficient parallel to the magnetic field is so much greater than that normal to the field. The absence of any significant effect of anode projected area has also been established experimentally.[13]

An additional diffusion correction can be made for the variation in area normal to the electron current flow j. The magnetic field lines close to the inner anode edges follow paths nearly parallel to the smoothed outer surface of the discharge chamber (see dashed line in Fig. 2-1)). Farther away from the anodes, though, the field lines follow longer, looping paths. This variation in field line length results in a similar variation in area normal to the diffusing electron current. A numerical integration through increments of $\int Bdx$ can be used to correct for this area variation. A numerical expression for the current density is

$$j = \frac{kT_e}{16} \frac{\sum_{i=1}^{N} \Delta\eta_{e_i}}{\sum_{i=1}^{N} (\Delta\int Bdx)_i \, d/\ell_{B_i}} \quad , \tag{2-12}$$

where Δn_{e_i} is the increment in electron density required to drive the current j through an increment in magnetic field integral $(\Delta\int Bdx)_i$ with an area $d\ell_{B_i}$ where ℓ_{B_i} is the length of the i^{th} field line and d is a unit length. The local current density thus equals j where $\ell_{B_i}/d = 1$. Solving Eq. (2-12) is facilitated if advantage is taken of the analogy with current flow through resistors connected in series. The increment Δn_e is analogous to the voltage across a resistor, while the resistance is analogous to $(\Delta\int Bdx)_i \, d/\ell_{B_i}$. It can be shown then that an effective overall value for ℓ_{B_i}/d is

$$\frac{\ell_{B_{eff}}}{d} = \frac{\int Bdx}{\int B \frac{d}{\ell_B(x)} dx} \tag{2-13}$$

where the integral is over the region between the anode and the nearly field-free main volume of the discharge chamber. An appropriate expression for the multipole field is[12]

$$B = B_{max} \exp[-1.5(x/d+1/2)^2] \quad , \tag{2-14}$$

where x is indicated in Fig. 2-1. Assuming parabolic arc paths for field lines between the ends of pole pieces, it can be found by integrating Eq. (2-13) that the area correction yields a current density expression,

$$j \approx \frac{kT_e n_e}{13\int B dx} \qquad (2\text{-}15)$$

where j is based on the area indicated by the dashed line in Fig. 2-1. Equation (2-15), then, can be used to find the maximum electron current that will diffuse to the anodes without causing the anodes to become more positive than the discharge-chamber plasma. In view of the relatively small difference between Eqs. (2-11) and (2-15), a more accurate correction for the area effect does not appear necessary. Also, a separate correction for corner pole pieces, which have a slightly different variation of B with x, is not required.

Comparison with Experimental Results

The first comparison is with data obtained using the 30-cm multipole discharge chamber (configuration described in Ref. 12). This discharge chamber was operated using a variable number of anodes connected to the positive potential of the discharge supply. The plasma was initially close to anode potential with all the anodes connected. As more anodes were disconnected, the plasma assumed a potential substantially negative of the anodes. This effect is shown in Fig. 2-2. Figure 2-2 was obtained at close to the minimum discharge voltage for each fraction of total anode length. The minimum discharge voltage was determined by operating at a constant discharge current of 1.0 A and slowly decreasing discharge voltage until the discharge was extinguished. The value of this minimum voltage ranged from 34-35 V at an anode length fraction of 1.0 to 72-85 V at an anode length fraction of 0.5. Data obtained at discharge voltages about 10 V higher than minimum exhibited the same behavior. The two propellant densities shown in Fig. 2-2 cover the usual range of interest

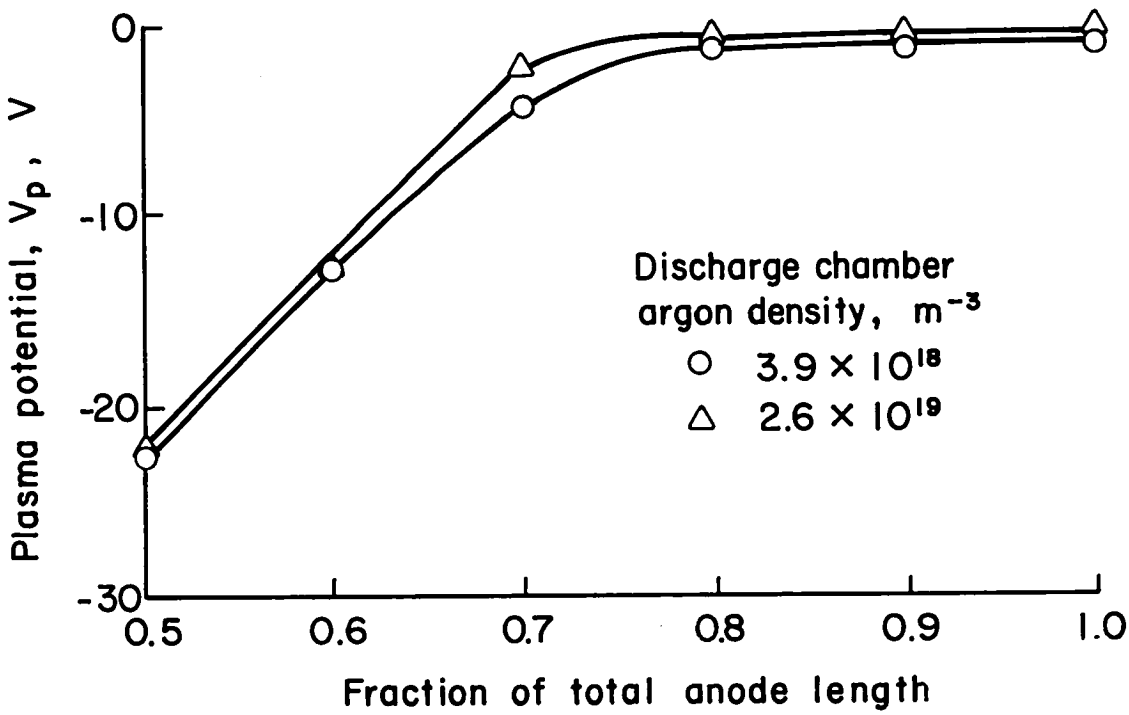

Fig. 2-2. Plasma potential (relative to the anode) as a function of anode configuration near the minimum discharge voltage. Discharge current was 1.0 A.

for thruster operation. When the effective anode area (proportional to active anode length) is reduced below an approximate critical value, the plasma potential apparently must become increasingly negative of the anodes to maintain the desired electron current to the anodes. Because electron diffusion can result from both potential and density gradients, the added contribution of the potential gradient is the amount required to compensate for the reduced anode area. This contribution is treated later.

Theoretical electron currents to the anodes were calculated using Eq. (2-15), the effective anode area for the active anodes, and plasma properties from a centrally located Langmuir probe. The experimental anode currents were assumed to be the sums of discharge (emission) and beam currents. The ratios of experimental-to-theoretical anode currents were then plotted in Fig. 2-3. The trends appear clear. The anode current ratio, J_{exp}/J_{th}, becomes greater than unity at close to the anode fraction where the plasma becomes negative of the anodes. The agreement between J_{exp} and J_{th} shown in Fig. 2-3 for electron diffusion without assistance from a potential gradient indicates that the physical process is being appropriately modeled in this regime.

Operation with a plasma significantly negative of the anodes was observed to be marginally stable, or even unstable. The data of Figs. 2-2 and 2-3 were obtained by using rheostats to gradually disconnect anodes, thereby minimizing switching transients. Without these rheostats, switching of anodes without extinguishing the discharge was reliable only above $\sim$70% of total anode length.[12] That is, it was reliable only at anode lengths where the plasma was not significantly negative of the anodes.

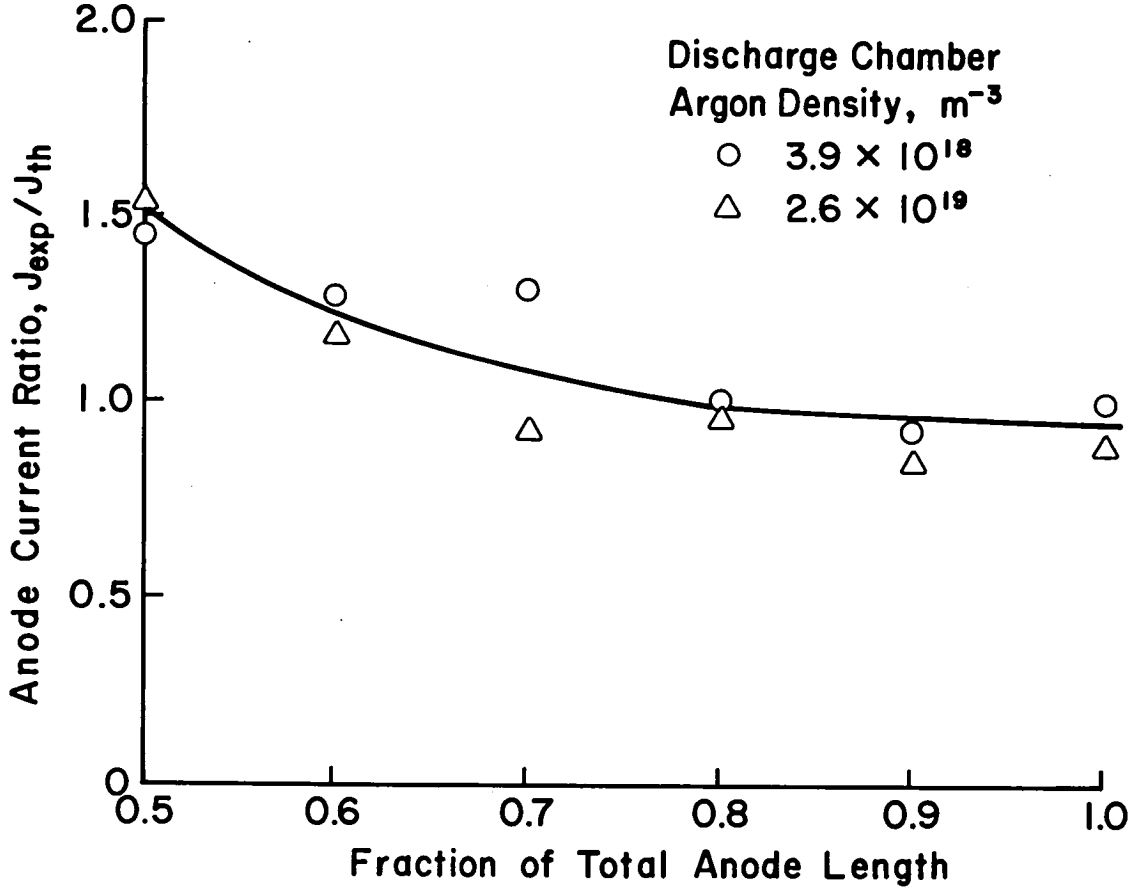

Fig. 2-3. Experimental to theoretical anode current ratios.

Other tests were also conducted with both 15-cm and 7.5-cm multipole discharge chambers (configurations described in Refs. 14 and 15). Because plasma probe data were not obtained with these smaller discharge chambers, it was necessary to estimate electron temperature from other tests and electron density from beam current. To the latter end, the beam current extracted can be expressed as

$$J_b = A_{scr}\, n_e v_B e \ , \tag{2-16}$$

where n_e is the electron/ion density, v_B is the Bohm critical sheath velocity, e is the absolute electronic charge, and A_{scr} is the effective open screen area for extraction. This area can be somewhat above or below the geometrical open area, but the latter should be a good approximation. Replacing the Bohm velocity with the equivalent expression $(kT_e/m_i)^{\frac{1}{2}}$, Eq. (2-16) becomes

$$J_b = A_{scr} n_e e (kT_e/m_i)^{\frac{1}{2}} \ . \tag{2-17}$$

Using K_{ab} as the anode-to-beam current ratio, the anode current required to generate the ion beam can be written as

$$J_a = K_{ab} A_{scr} n_e e (kT_e/m_i)^{\frac{1}{2}} \ . \tag{2-18}$$

From Eq. (2-15), the current permitted to diffuse to the anode (or anodes) without the anode becoming substantially more positive than the discharge-chamber plasma is

$$J_a = A_a kT_e n_e / 13 \int B dx \ . \tag{2-19}$$

Equating these two anode currents to obtain the minimum anode area for stable operation,

$$A_a = 13\ K_{ab} A_{scr} e\int B dx/(kT_e m_i)^{\frac{1}{2}} . \qquad (2\text{-}20)$$

This, then, is the relationship that can be used in the absence of plasma probe data.

In earlier tests of the 15-cm discharge chamber with argon[13] the mean electron temperature ranged from about 5 to 15 eV. Using 10 eV as a typical value, together with measured values for the magnetic field integral, screen open area, and anode-to-beam current ratio at the minimum stable discharge voltage, Eq. (2-20) was used to estimate anode area. For a 48 magnet configuration of the 15-cm chamber, an anode area of 390-570 cm^2 was estimated; while for a 24 magnet configuration an anode area of 430-510 cm^2 was estimated. The measured anode area for both magnet configurations was 471 cm^2, which is in agreement with the estimates from Eq. (2-20).

Minimum discharge voltage tests, similar to those discussed in connection with Fig. 2-2, were conducted with the 7.5-cm discharge chamber. Inasmuch as electron temperature generally increases as thruster size becomes smaller, an electron temperature of 15 eV was felt to be a better estimate for this thruster size. With this temperature and discharge data similar to those obtained for the 15-cm tests, Eq. (2-20) indicated an anode area of 70-130 cm^2. The measured anode area was 118 cm^2, which again is in agreement.

Potential- and Density-Gradient Driven Conduction

Certain aspects of thruster operation involve strong potential gradients that could substantially enhance the electron diffusion. A general approach to electron diffusion across magnetic fields, which includes effects of both potential and density gradients, is therefore of interest. One such aspect is the diffusion of electrons through a magnetic baffle orifice to the discharge chamber. Yet another is the possible use of anodes more positive than the discharge plasma to provide electrostatic containment of the ions produced, thereby lowering the discharge losses.[7] The data shown in Fig. 2-2 were adequately described by density-gradient driven diffusion only down to the operating condition where the plasma remained positive of the anodes; to understand the remainder of the experimental data, it is necessary to introduce the effect of potential gradients.

The basic relation governing electron diffusion in the presence of both potential and density gradients is

$$\vec{\Gamma} = \mu n_e \vec{\nabla} V - D \vec{\nabla} n_e \qquad (2\text{-}21)$$

where V is the potential and μ is the electron mobility. The mobility and diffusion coefficients are connected by the Einstein relation.[16]

$$\mu = eD/kT_e \qquad (2\text{-}22)$$

Using the Bohm diffusion coefficient Eq. (2-21) can yield a one-dimensional current density

$$j = -\frac{en_e}{16B}\frac{dV}{dx} + \frac{kT_e}{16B}\frac{dn_e}{dx} \quad . \tag{2-23}$$

The volume under consideration is small, so that electron production (through electron-atom impacts) is small and can be ignored. Also, the current density is approximately constant. Using this, we can write

$$16jBdx = kT_e dn_e - en_e dV \quad . \tag{2-24}$$

Integrating both sides over the diffusion depth,

$$16j\int Bdx = k\int T_e dn_e - e\int n_e dV \ . \tag{2-25}$$

Solving for the current density, we find

$$j = (k\int T_e dn_e - e\int n_e dV)/16\int Bdx \ . \tag{2-26}$$

It has been shown previously (Eq. (2-15)) that the factor of 16 should be replaced by 13 when dealing with a multipole design. If both potential and density gradients are present driving the electron diffusion, then most of the potential difference will occur at the lowest density region (see the first term in Eq. (2-23)). A situation involving both of these gradients will therefore tend to have most of the density difference near the source of electrons (plasma) and most of the potential difference at low density after the electrons have passed through almost all of the density difference.

This problem was examined from a number of different viewpoints using Eqs. (2-23) through (2-26) and similar approaches, but no minimum

thickness of the potential gradient region was evident from these equations, for diffusion to anodes. But these equations all implicitly assumed continuum processes, hence did not include the effect of finite orbit size. The realistic lower limit for the thickness of the potential gradient region in the anode problem was picked to be small enough to permit escape of a thermal electron to the anode without a collision. This means that the magnitude of $\int Bdx$ in this thickness would be obtained from the total ΔV between the plasma and the anode.

The first region, dominated by density gradient, is described by the diffusion equation developed for no potential difference that was derived earlier. This equation can be derived from Eq. (2-26) by letting T_e be a constant and dV be zero. Integrating from the initial electron density down to zero density, we obtain for a multipole configuration

$$j = kTn_o/13\int Bdx \qquad (2\text{-}27)$$

where n_o is the bulk plasma density. But we need to remember that $\int Bdx$ is no longer the total integral, but is just that fraction of the integral over which diffusion dominated by the density gradient takes place. To obtain this portion of the integral we must subtract from the total integral the value that can be crossed by an initially motionless electron due to a potential difference of ΔV. This portion was found by analysis to be

$$\Delta\int Bdx = (2m\Delta V/e)^{\frac{1}{2}} . \qquad (2\text{-}28)$$

This result is independent of the variation of V with B and x, as long as the ΔV from the initial to any intermediate condition is equal to or

greater than the ΔV from Eq. (2-28) for the portion of $\int Bdx$ traversed.[17] The best agreement with experimental data was obtained if an additional increment of $\int Bdx$ was also subtracted out due to thermal electrons on the high density (n_o) side having sufficient energy to penetrate magnetic field due to their thermal energy alone. This increment is governed by essentially the same equation as that for the penetration of magnetic field by primary electrons,[6]

$$\Delta \int Bdx = (8mkT/e^2)^{\frac{1}{2}} . \qquad (2\text{-}29)$$

Subtracting the increments given by Eqs. (2-28) and (2-29) from the total value of $\int Bdx$, then, gives the value to use in Eq. (2-27).

Comparison with Experimental Results

The diffusion model described herein was used to calculate a diffusion current density, hence an anode-area requirement for the experimental data of Fig. 2-2. Using mean electron temperatures of 4.7 and 3.2 eV and mean electron densities of 1.1 and 1.8×10^{16} m^{-3} for the argon neutral densities of 3.9 and $26. \times 10^{18}$ m^{-3}, the curves shown in Fig. 2-4 were calculated. (The temperatures and electron densities given were the average values for the experimental data shown for each neutral density. The anode current averaged about 1.2 A for all the data.) The experimental data are shown by the open symbols. The closed symbols without tails show the current density predicted by Eq. (2-27) with the full value of $\int Bdx$ used. The closed symbols with tails show the same current density, except $\int Bdx$ is reduced by the increments of Eqs. (2-28) and (2-29). The agreement between theory and experiment is good over the entire range of operating conditions.

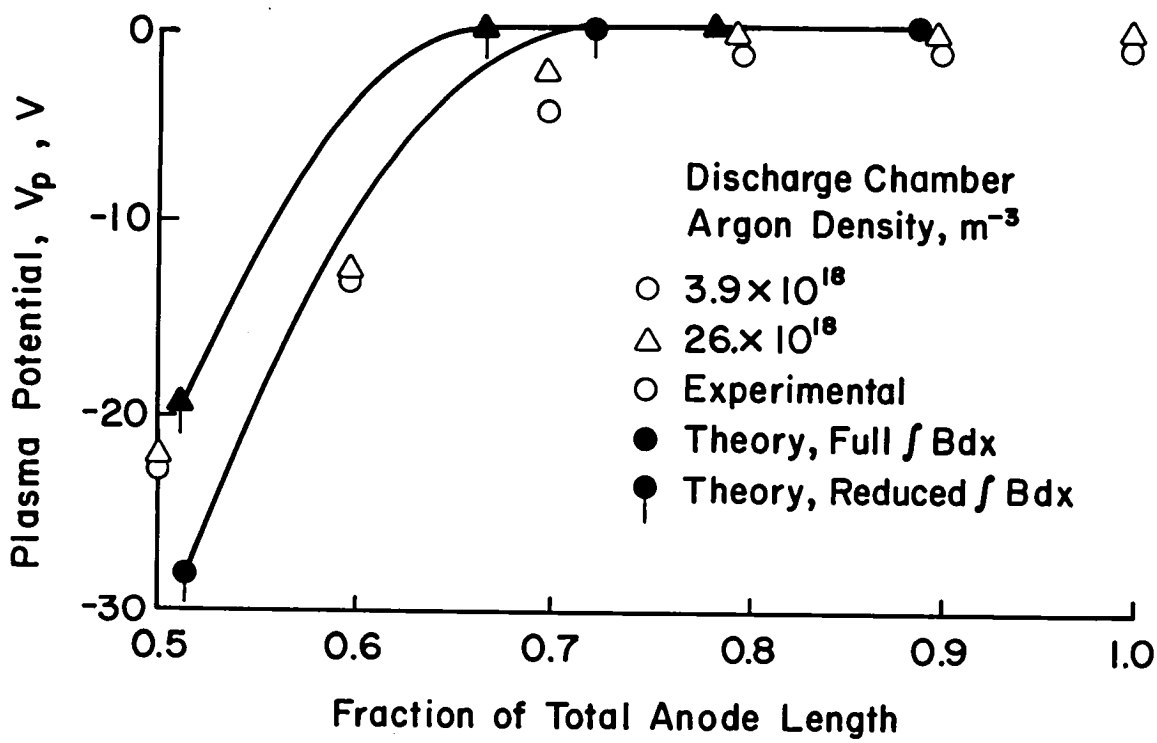

Fig. 2-4. Comparison between theoretical and experimental plasma potentials as a function of anode configuration.

The simplest density-gradient diffusion, Eq. (2-15), appears to give adequate accuracy in the absence of any large potential gradient. The reduction of $\int Bdx$ used in Eq. (2-15) by the increment of Eq. (2-29) appears to give slightly better accuracy for the same conditions. When a significant potential gradient is present, the value of $\int Bdx$ used in Eq. (2-15) must be reduced further by the increment of Eq. (2-28).

Applications

As mentioned earlier in this section, the diffusion theory presented appears to be applicable wherever electrons must cross magnetic field lines to reach a discharge chamber anode. For example, we can apply this theory to mildly divergent magnetic field thrusters. Because the magnetic field lines of such a thruster do not follow long looping paths, a constant of 16 should replace the constant of 13 in the equations. With this change, a Maxwellian electron temperature of 5 eV, the atomic weight of mercury, a moderate magnetic-field integral of 75×10^{-6} Tesla-m, and a typical anode-to-beam current ratio of 11, the minimum ratio of A_a/A_{scr} is about 4. For the usual 50% open screen of early thrusters, this ratio translates into a minimum anode that is about twice the total beam area. Or expressed somewhat differently, a minimum length-to-diameter ratio of about 0.5 for the discharge chamber. This result is in qualitative agreement with observations of early thrusters, where a length-to-diameter ratio of unity, or slightly less, showed stable operation. Shorter chambers, though, were hard to start and tended to extinguish easily.

This diffusion model is also applicable to general performance trends. For example, the minimum permissible discharge voltage tends to

increase as neutral pressure in the discharge chamber is decreased. It is also known that, in most operating ranges of interest, the discharge losses tend to increase as neutral density is decreased. This increase would result in an increase in required anode current at constant discharge voltage, which, in itself, would result in an increased requirement for anode area. If this increased anode area is not available, then the minimum discharge voltage increases until the anode current becomes consistent with the anode area available.

As another example of performance trends, operation with lighter gases has been observed to result in more difficulty in maintaining a discharge, usually with higher minimum discharge voltages. We know that electron temperature usually increases somewhat with lighter ion masses, but not as rapidly as the mass decreases. From Eq. (2-20), then, the net effect of electron temperature and ion mass changes should be to require more anode area for a lighter gas. This result is consistent with the observed operational problems described above.

The electrostatic containment of ions (to reduce required discharge losses) was proposed by Moore[18] and Ramsey.[19] Although a significant fraction of the anodes were operated substantially positive of the discharge-chamber plasma in the multipole tests described earlier, no decrease in discharge losses was noted. It would appear that the turbulence expected with Bohm diffusion is probably sufficient to scatter a significant number of ions into the anodes and pole pieces despite the average adverse electric field. The advantage of electrostatic containment thus appears to be offset, at least in part, by the effects of plasma turbulence. However, because a positive ion bias was only obtained with a portion of the anodes at a time, firm conclusions are difficult to draw from the data presented.

The diffusion model presented here assumes continuous paths (closed loops) for electron drift velocity normal to any applied electric field. For the observed magnitude of Bohm diffusion, this drift velocity is about 16 times the diffusion velocity in the direction of the applied electric field. This means that, in the presence of an electric field near anodes, the electron drift velocity parallel to the anodes is much greater than the diffusion velocity toward the anodes. When the drift velocity path is interrupted, an electric field is produced normal to the original electric field, which increases electron diffusion due to the original electric field. Translated into multipole anode design, interrupted drift paths should increase the desired diffusion of Maxwellian electrons, easing collection area limitations for the anode as well as reducing minimum discharge voltages.

The general case of electron diffusion across magnetic fields includes diffusion through a baffle gap. For this application, the use of diffusion at constant density (equal to the discharge chamber value) gives more consistently accurate results than single particle orbits when used as the second step of the diffusion process.[20] The first step is again density-gradient driven, but the driving density difference is the difference between the baffle region and the discharge chamber value, not the total baffle region density.

III. DOUBLY CHARGED ION PRODUCTION

Doubly charged ions constitute a significant lifetime problem for inert-gas ion thrusters. A theory exists for the prediction of the doubly charged ion production rate,[1,2] but the utility of this theory is limited by the requirement for prior detailed plasma probe data.

There is a major need for the prediction of the doubly charged ion production rate in the absence of plasma probe data, preferably even in the absence of any experimental data (in the design phase). The requirement for plasma probe data can perhaps be offset by correlations of plasma properties. The correlations of plasma properties could then be used to estimate these properties in the absence of probe data.

It would be simpler, though, to correlate the production of doubly charged ions directly, instead of calculating from the correlated plasma properties. This approach should be more effective for a family of similar discharge chambers, where the operation of different chambers would be expected to have a basic similarity. Multipole chambers constitute such a family, in addition to having very uniform plasmas throughout most of the chamber volumes.

The ratio of doubly to singly charged ion beam currents is related to the ratio of number densities of the corresponding species in the discharge chamber.

$$I^{++}/I^{-} = 2^{3/2}\, n_{++}/n_{+} \tag{3-1}$$

The ratio of number densities in the discharge chamber has been described, in turn, by[2]

$$\frac{n_{++}}{n_+} = \frac{\Omega_p}{A_p} F_{++} \quad \frac{n_p[P_+^{++}+(n_o/n_+)P_o^{++}]+n_m[Q_+^{++}+(n_o/n_+)Q_o^{++}]}{[2\ T_m(e/m_i)(1+n_p/n_m)]^{\frac{1}{2}}} \qquad (3\text{-}2)$$

where Ω_p/A_p is the ratio of volume to outside area for the primary electron region, n_p is the density of primary electrons, n_m is the density of Maxwellian electrons, n_+ is the singly charged ion density (for $n_{++} << n_+$, $n_+ \approx n_p + n_m$), F_{++} is a uniformity factor for doubly charged ions, T_m is the Maxwellian electron temperature, e/m_i is the charge-to-mass ratio for singly charged ions, P_o^{++} and P_+^{++} are the primary electron rate factors for neutral to doubly ionized and singly to doubly ionized, and Q_o^{++} and Q_+^{++} are the Maxwellian electron rate factors for the same two ionization processes. For a multipole chamber, the primary electron region can be treated as the smoothed-off geometrical shape that will just fit inside the anodes, screen grid, and (if any) the cathode pole piece. The rate factors P_o^{++} and P_+^{++} are functions of primary electron energy, while the rate factors Q_o^{++} and Q_+^{++} are functions of Maxwellian electron temperature. The ratio n_o/n_+ in Eq. (3-2) can be determined from

$$\frac{n_o}{n_+} = \frac{A_p}{\Omega_p} \frac{[T_m(e/m_i)(1+n_p/n_m)]^{\frac{1}{2}}}{F_{++}[n_p P_o^{+}+n_m Q_o^{+}]}, \qquad (3\text{-}3)$$

where P_o^{+} and Q_o^{+} are the primary and Maxwellian electron rate factors for neutral to singly ionized processes.

As shown previously,[2,3] production of doubly charged inert-gas ions can be significant from both primary and Maxwellian electrons, and from both the neutral and singly ionized states. The prediction of most

interest is for larger thrusters, with larger values of Ω_p/A_p. From Eq. (3-1), the ratio of n_o/n_+ becomes smaller with increasing Ω_p/A_p. From this trend and Eq. (3-2), the P_o^{++} and Q_o^{++} processes will become negligible compared to the P_+^{++} and Q_+^{++} processes as Ω_p/A_p increases.[1] Rewriting Eq. (3-2) with the P_o^{++} and Q_o^{++} processes omitted,

$$\frac{n_{++}}{n_+} = \frac{\Omega_p}{A_p} F_{++} \frac{n_p P_+^{++} + n_m Q_+^{++}}{[2T_m(e/m_i)(1+n_p/n_m)]^{\frac{1}{2}}} \quad . \tag{3-4}$$

Substitution of Eq. (3-4) into Eq. (3-1) gives

$$\frac{I^{++}}{I^+} = 2 \frac{\Omega_p}{A_p} F_{++} n_p \frac{P_+^{++} + (n_m/n_p) Q_+^{++}}{[T_m(e/m_i)(1+n_p/n_m)]^{\frac{1}{2}}} \quad . \tag{3-5}$$

A further change that takes place with increasing thruster size is a decrease in Maxwellian electron temperature, T_m.[1,4,5] The major effect of this change is that the Q_+^{++} process becomes less important than the P_+^{++} process. The primary electron density, n_p, should be (for large thrusters) more important than the Maxwellian electron density, n_m. From an overall performance viewpoint, the primary electron density, n_p, is the major unknown. This density can be related to the total singly charged ion production rate, R^+,

$$R^+ = n_o n_p P_o^+ \Omega_p \quad , \tag{3-6}$$

where P_o^+ is the primary electron rate factor for neutral to singly ionized. This production rate can, in turn, be related to the ion beam current. For this approximate derivation, the doubly ionized contribution

to the ion beam current can be ignored, giving

$$J_o = eR^+(A_s/A_p) \ , \tag{3-7}$$

where the fraction of ions produced that leave in the ion beam is the ratio of screen open area to primary electron region area, A_s/A_p. The neutral density in Eq. (3-6) can be related to the total neutral flow, J_o, the propellant utilization, η_u, the most probable neutral velocity, $\bar{v}_o$, and the effective sharp-edged orifice area of the ion optics to the escape of neutrals, A_o.

$$J_o(1-\eta_u) = A_o e n_o \bar{v}_o/4 \tag{3-8}$$

Combining Eqs. (3-6) through (3-8), the primary electron density is found equal to

$$n_p = A_o A_p J_b \bar{v}_o/4A_s J_o P_o^+(1-\eta_u)\Omega_p \ . \tag{3-9}$$

Substitution of this expression in Eq. (3-5) yields

$$\frac{I^{++}}{I^+} = \frac{A_o F_{++} J_b \bar{v}_o}{2A_s P_o^+ J_o(1-\eta_u)} \ \frac{P_+^{++}+(n_m/n_p)Q_+^{++}}{[T_m(e/m_i)(1+n_p/n_m)]^{\frac{1}{2}}} \ . \tag{3-10}$$

An approximate solution can be obtained by moving A_o, A_s, J_b, $J_o(1-\eta_u)$, and P_+^{++} to the left side.

$$\frac{(I^{++}/I^{+})j_o(1-\eta_u)}{(J_b/A_s)A_o P_+^{++}} = \frac{F_{++}v_o}{2\,P_o^{+}} \frac{1 + (n_m/n_p)Q_+^{++}/P_+^{++}}{[T_m(e/m_i)(1+n_p/n_m)]^{\frac{1}{2}}} \qquad (3\text{-}11)$$

Note that there is still a P_+^{++} on the right side, but, under the conditions assumed for the derivation, the term $(n_m/n_p)Q_+^{++}/P_+^{++}$ should be small compared to unity. All other factors on the right side should be constants, or vary over only a small range. For correlation purposes, the P_+^{++} can be approximated by

$$P_+^{++} = K(eV_d - \phi_2) \ , \qquad (3\text{-}12)$$

where the primary electron energy is the product of electronic charge and discharge voltage, and ϕ_2 is the second ionization potential. Substitution of Eq. (3-12) into Eq. (3-11)
yields

$$\frac{(I^{++}/I^{+}J_o(1-\eta_u)}{(J_b/A_s)A_o(eV_d-\phi_2)} = \frac{F_{++}K\bar{v}_o}{2P_o^{+}} \left(\frac{1+(n_m/n_p)Q_+^{++}/P_+^{++}}{[T_m(e/m_i)(1+n_p/n_m)]^{\frac{1}{2}}}\right) . \qquad (3\text{-}13)$$

The right side of Eq. (3-13) should not vary over a wide range, but it should vary with n_p/n_m, as well as some variation with other parameters.

Preliminary correlation attempts indicated a strong effect of discharge power on double ion production. Discharge losses can be correlated in a fairly general manner, particularly for a family of

similar discharge chambers.[4] Using a 15-cm multipole discharge chamber, performance data that were obtained at the same time as double ion production data[2,4,6] were used for the performance correlations shown in Figs. 3-1 and 3-2 for xenon and argon.

The left side of Eq. (3-13) was used as a correlation parameter for doubly charged ions. To approximate the effects of different discharge losses, this correlation parameter is plotted against the neutral loss parameter in Figs. 3-3 and 3-4 for xenon and argon in a 15-cm multipole thruster.[4] Because a particular value of neutral loss parameter is associated with a particular value of discharge loss (see Figs. 3-1 and 3-2) the correlations of Figs. 3-3 and 3-4 are equivalent to plotting against discharge loss.

Another double ion correlation parameter can be obtained by dividing the left side of Eq. (3-13) by the neutral loss parameter.

$$\frac{(I^{++}/I^{+})A_s J_o}{A_o J_b (eV_d - \phi_2)} \quad \frac{J_o(1-\eta_u)}{A_o} \quad \frac{\Omega_p}{A_p} = \frac{(I^{++}/I^{+})A_p A_s}{J_b (eV_d - \phi_2)\Omega_p} \tag{3-14}$$

Correlations based on this parameter are shown in Figs. 3-5 and 3-6 for the same 15-cm multipole data. An advantage of these modified correlations is that the data are nearly constant above a certain value of neutral loss parameter ($\sim$0.5 for xenon and $\sim$2 for argon).

The correlation of Figs. 3-5 and 3-6 can be used to check the accuracy of the assumed correction for discharge voltage, which is $1/(eV_d - \phi_2)$. The average values of $(I^{++}/I^{+})A_p A_s/J_b\Omega$ above a neutral loss parameter of 0.5 are shown in Fig. 3-7 for xenon and the three different discharge voltages investigated. The same is shown for argon above a

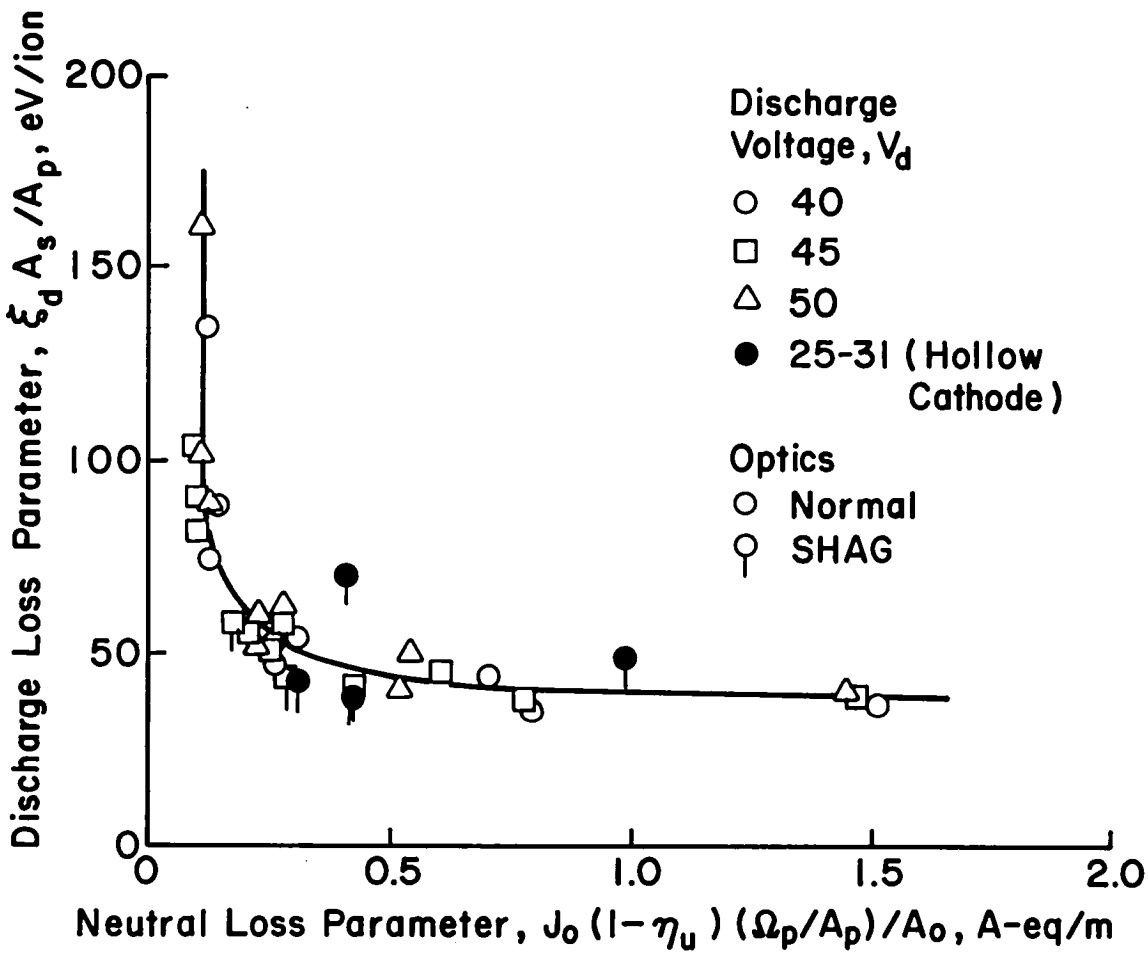

Fig. 3.1. Discharge loss correlation for xenon.

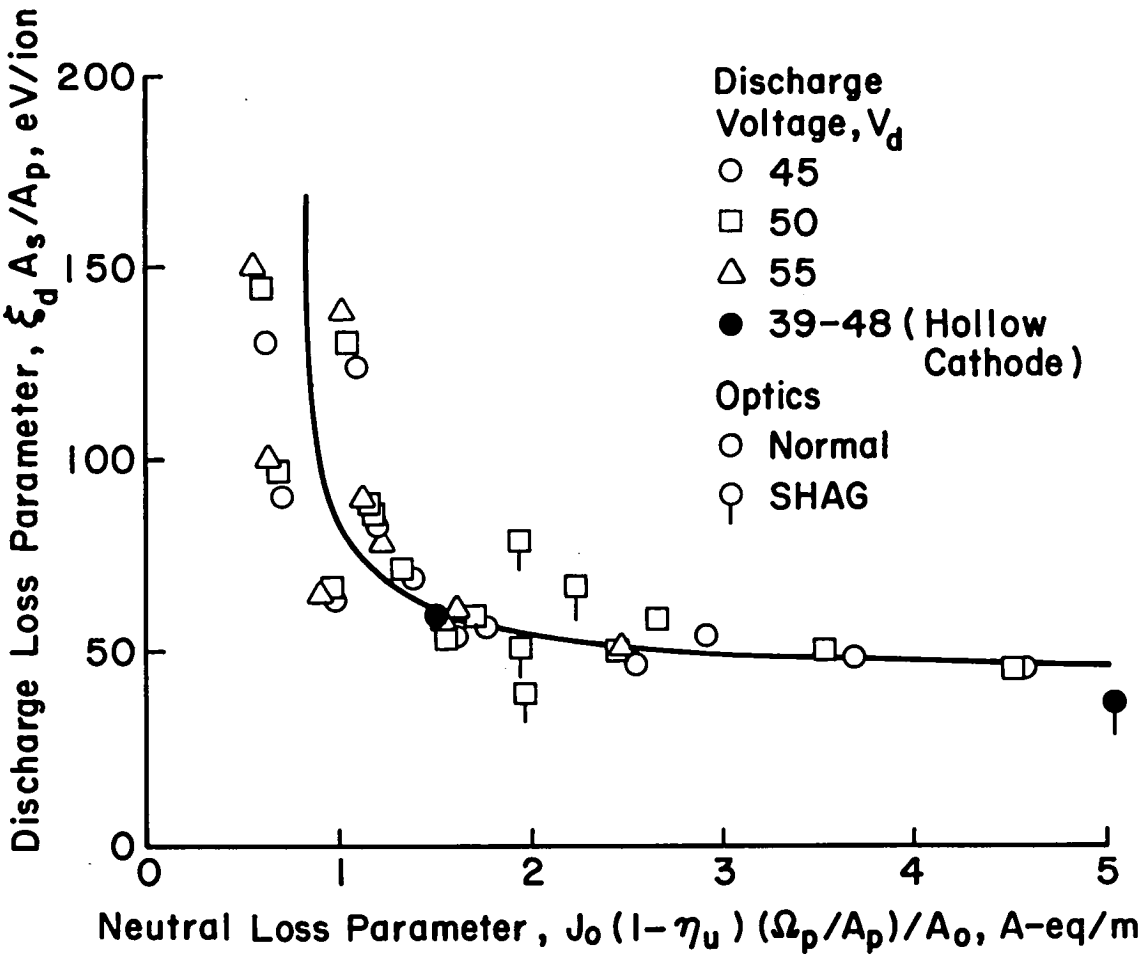

Fig. 3-2. Discharge loss correlation for argon.

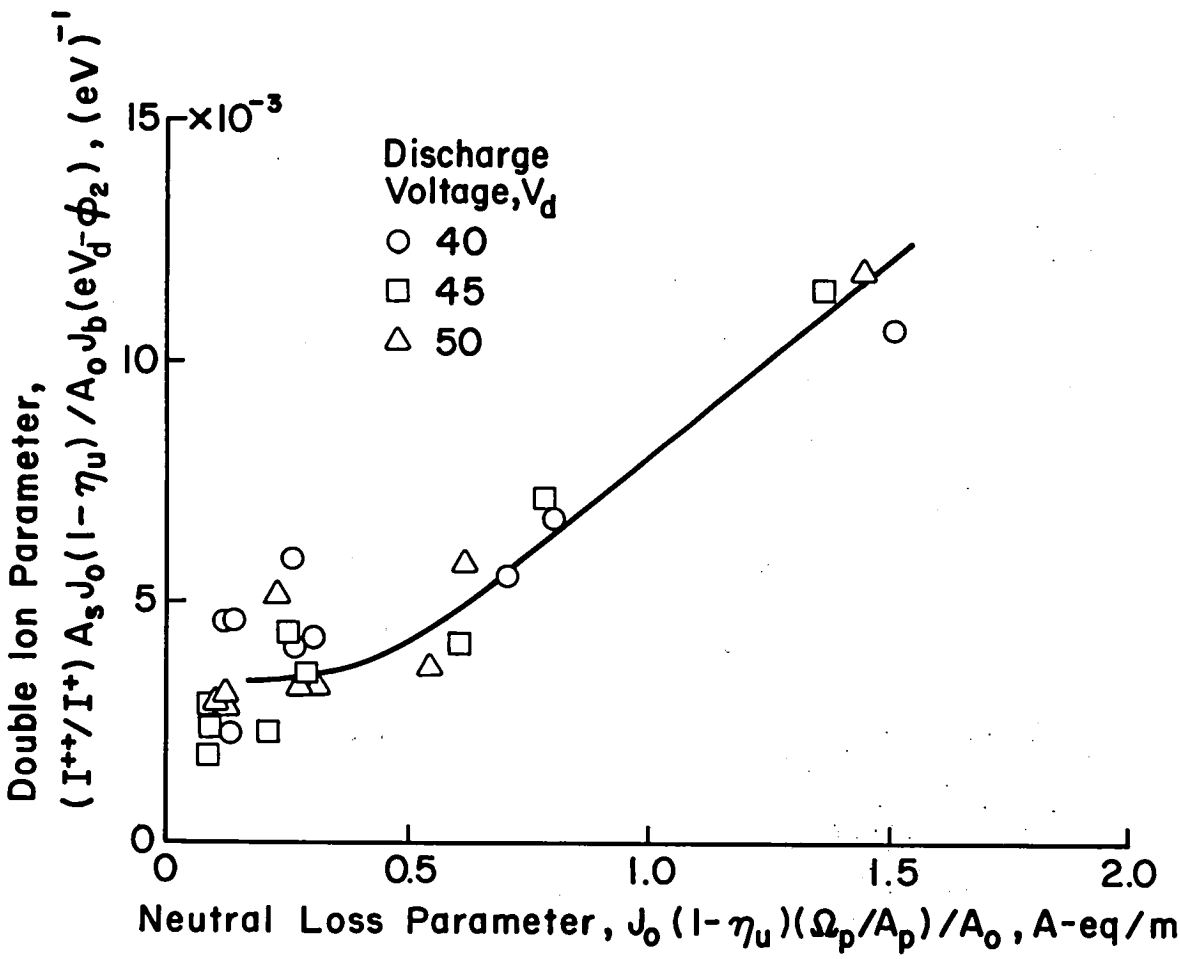

Fig. 3-3. Double ion correlation for xenon using $(I^{++}/I^{+})A_s J_o(1-\eta_u)/A_o J_b(eV_d-\phi_2)$ as the correlating parameter.

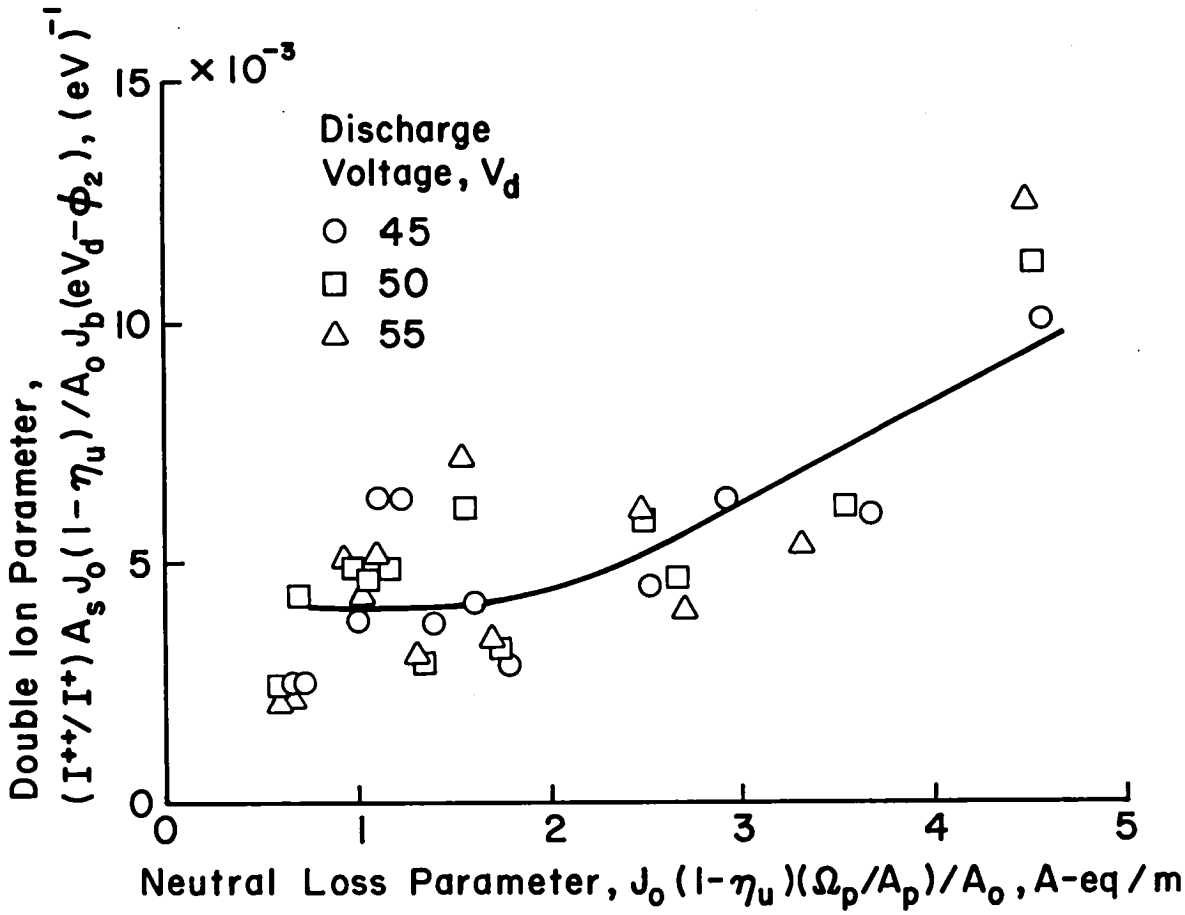

Fig. 3-4. Double ion correlation for argon using $(I^{++}/I^{+})A_s J_o(1-\eta_u)/A_o J_b(eV_d-\phi_2)$ as the correlating parameter.

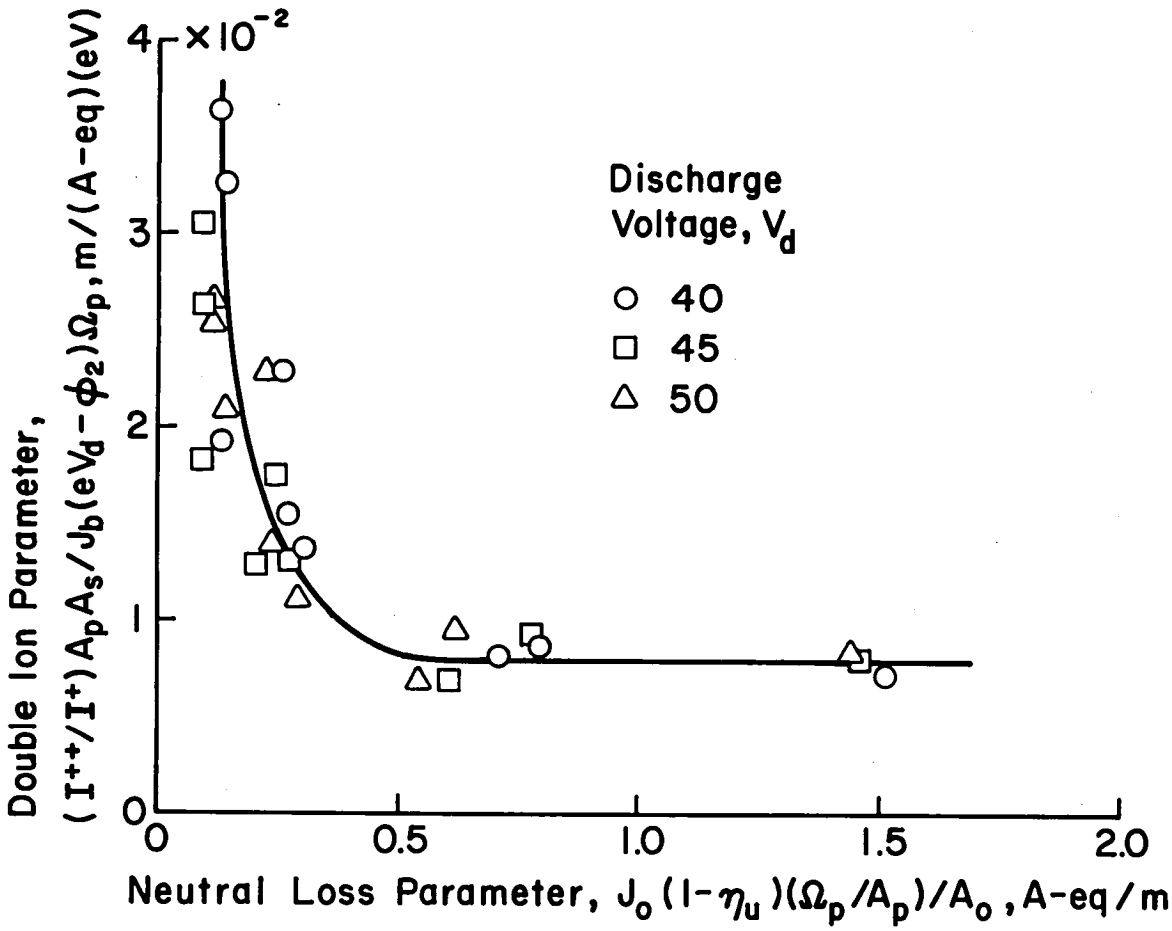

Fig. 3-5. Double ion correlation for xenon using $(I^{++}/I^{+})A_pA_s/J_b(eV_d-\phi_2)\Omega_p$ as the correlating parameter.

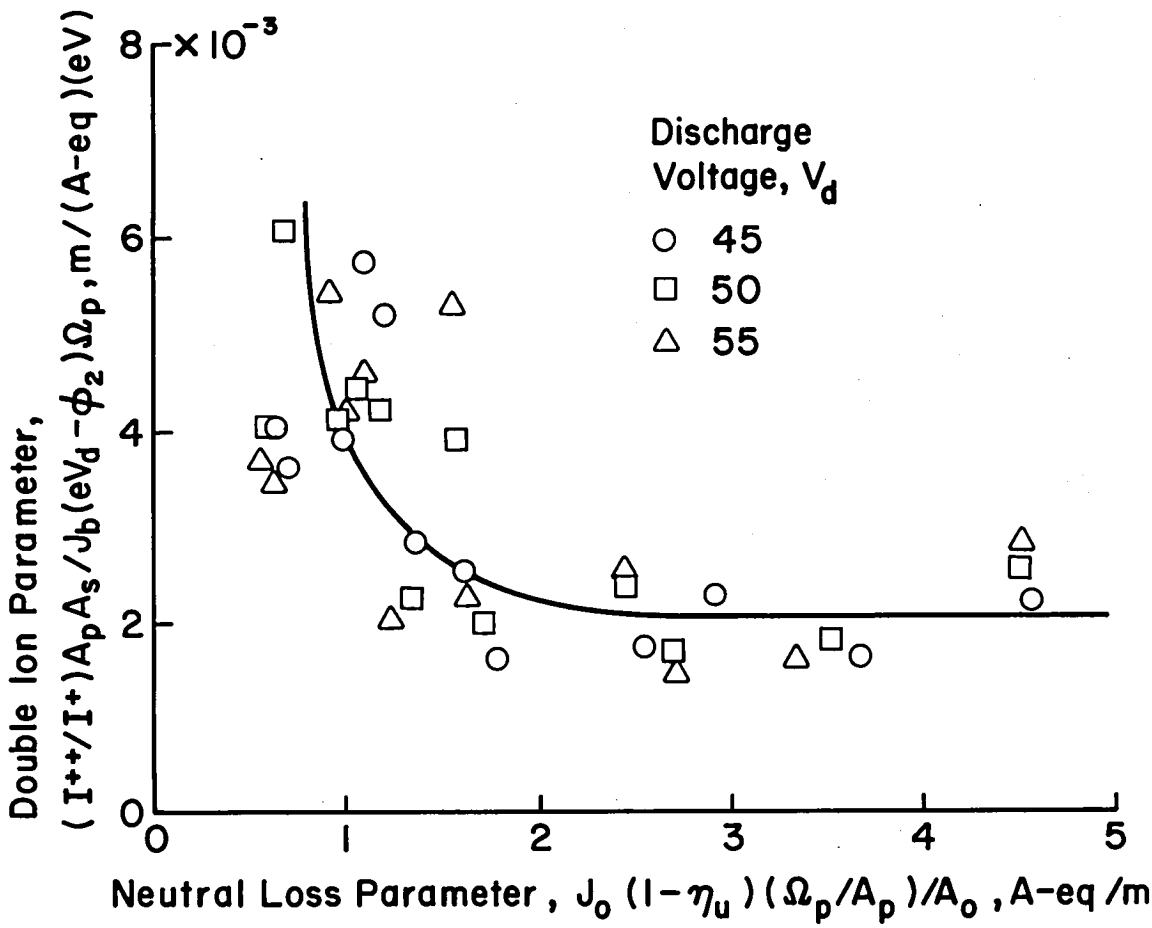

Fig. 3-6. Double ion correlation for argon using $(I^{++}/I^{+})A_pA_s/J_b(eV_d-\phi_2)\Omega_p$ as the correlating parameter.

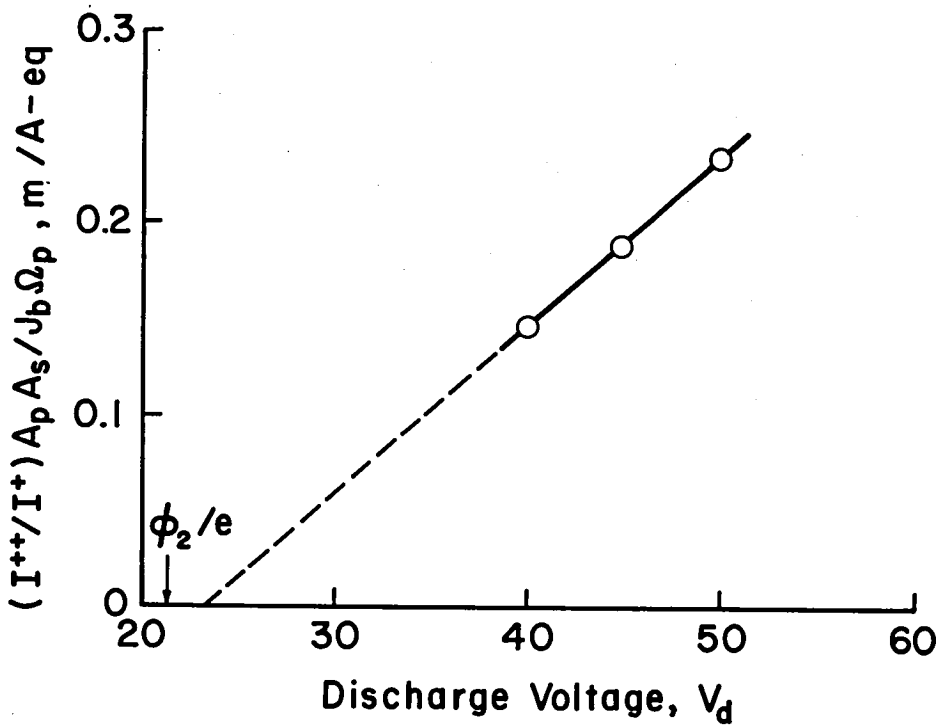

Fig. 3-7. Effect of discharge voltage on double ion parameter (neutral loss parameter ≥ 0.5, xenon).

neutral parameter of 2 in Fig. 3-8. The extrapolations back to zero double ions in Figs. 3-7 and 3-8 are close to the double ionization energy divided by electronic charge. These results are consistent with the correction used.

The 15-cm thruster used for the double ion data is far smaller than the sizes anticipated for many future large thruster applications. The trend that might be expected for larger thruster sizes is therefore of interest. A theoretical estimate of double ion production for large thrusters can be made from Eq. 3-13. For this theoretical estimate we assume both $(n_m/n_p)Q_+^{++}/P_+^{++}$ and n_p/n_m negligible compared to unity. This modifies Eq. 3-13 to

$$\frac{(I^{++}/I^{+})A_s J_o(1-\eta_u)}{A_o J_b(eV_d-\phi_2)} = \frac{F_{++}K\bar{v}_o}{2P_o^{+}(T_m e/m_i)^{\frac{1}{2}}} \quad . \tag{3-15}$$

For F_{++}, the average value of 7 can be used from previous studies with multipole chambers.[7] For K, the value is about 3.0×10^{-15} m^3/eV-sec for xenon and about 1.6×10^{-15} m^3/eV-sec for argon. For $\bar{v}_o$, the effective neutral temperature can be assumed to be about 600°K. For P_o^{+}, 1.4×10^{-13} m^3/sec for xenon and 9.7×10^{-14} m^3/sec for argon. (P_o^{+} does not vary rapidly with primary electron energy in the range of interest, but an electron energy of $\phi_1 + \phi_2$ was used for the preceding values.) For Maxwellian electron temperature, a value of $\phi_1/4$ was assumed. This value is in rough agreement with the 30-cm Maxwellian temperatures observed for mercury and argon propellant.[1,5] Using these values in Eq. (3-15), we find

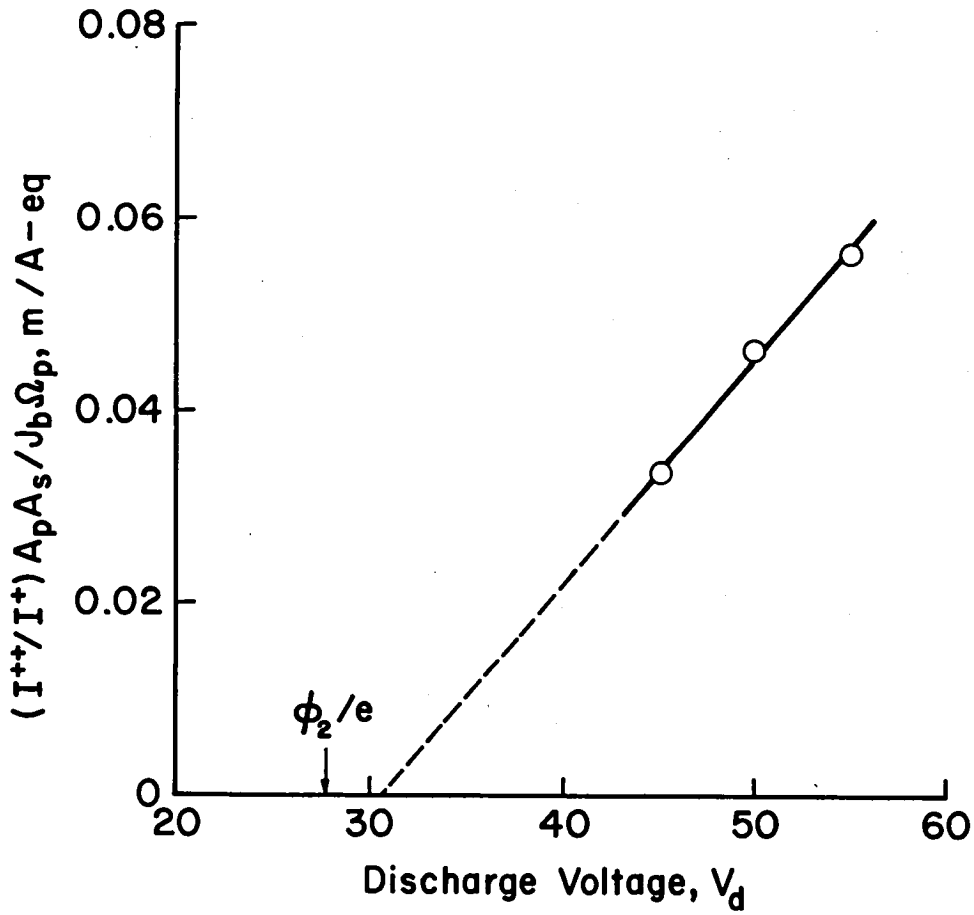

Fig. 3-8. Effect of discharge voltage on double ion parameter (neutral loss parameter ≥ 2, argon).

$$\frac{(I^{++}/I^{+})J_o(1-\eta_u)}{(J_b/A_s)A_o(eV_d-\phi_2)} = 0.0157(Xe),\ 0.0105(Ar)\ . \qquad (3\text{-}16)$$

Dividing both sides by the neutral loss parameter,

$$\frac{(I^{++}/I^{+})A_pA_s}{J_b(eV_d-\phi_2)\Omega_p} = 0.0157/\ \frac{J_o(1-\eta_u)\Omega_p}{A_oA_p}\ ,\ (Xe)\ , \qquad (3\text{-}17a)$$

$$\frac{(I^{++}/I^{+})A_pA_s}{J_b(eV_d-\phi_2)\Omega_p} = 0.0105/\ \frac{J_o(1-\eta_u)\Omega_p}{A_oA_p}\ ,\ (Ar)\ . \qquad (3\text{-}17b)$$

These equations are plotted in Figs. 3-9 and 3-10. The experimental data fall below the theory for both propellants, but come closest at high neutral loss parameters where low Maxwellian temperatures and low values of n_p/n_m would be expected. Increasing the thruster size from the 15-cm size used for the data presented herein would be expected to give closer agreement with the theory. Predictions for thrusters larger than the 15-cm size should therefore be between the experimental and theoretical curves.

Some additional double ion data were also included in Figs. 3-9 and 3-10. These were some small-hole-accelerator-grid (SHAG) data,[2] and some hollow cathode data.[6] Except for the latter, all the rest of the data were obtained with refractory cathodes. One might expect a lower double ion production with a hollow cathode (other parameters being the same), because some primary electron energy should be lost in the baffle region plasma. This effect does not appear significant for xenon, but may be the cause of the two argon hollow cathode points being

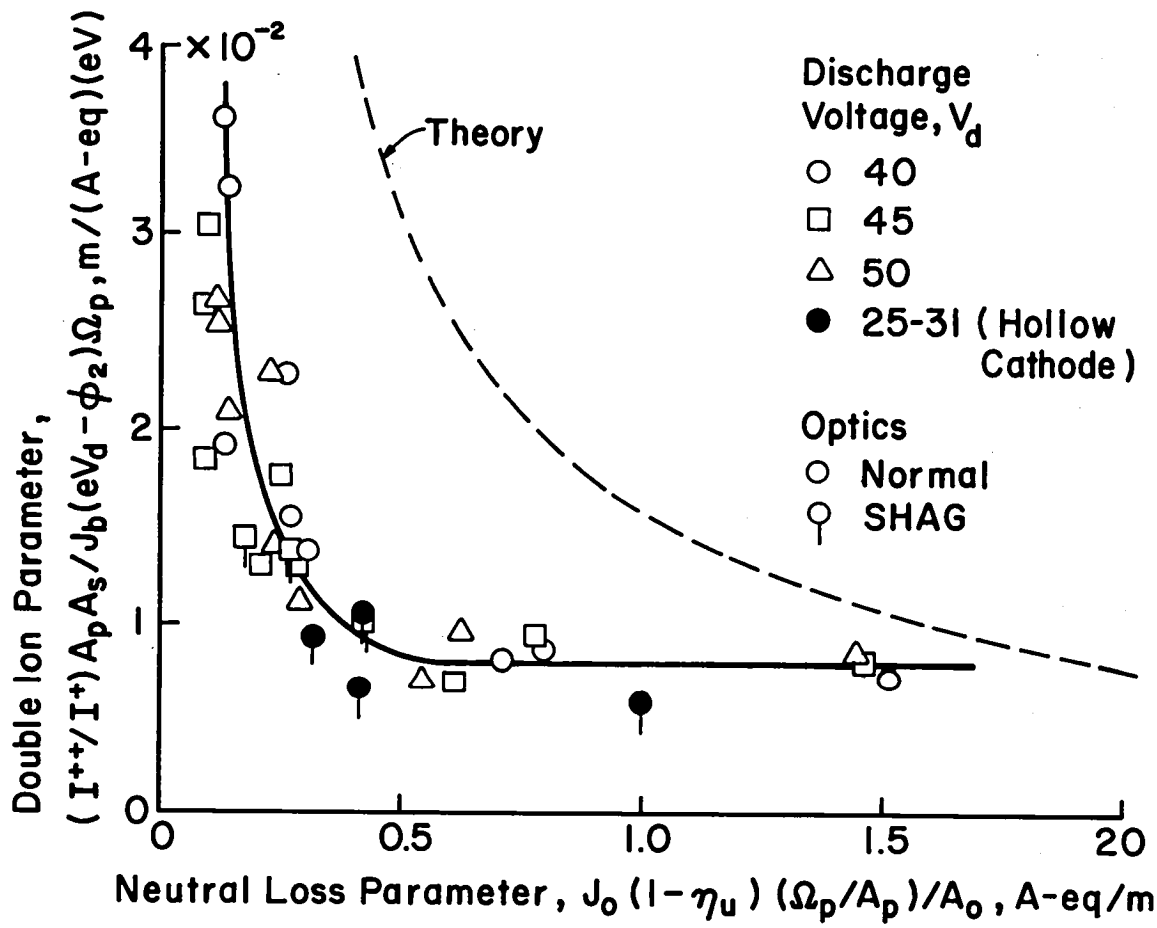

Fig. 3-9. Double ion correlation for xenon showing comparison with theory for large thrusters.

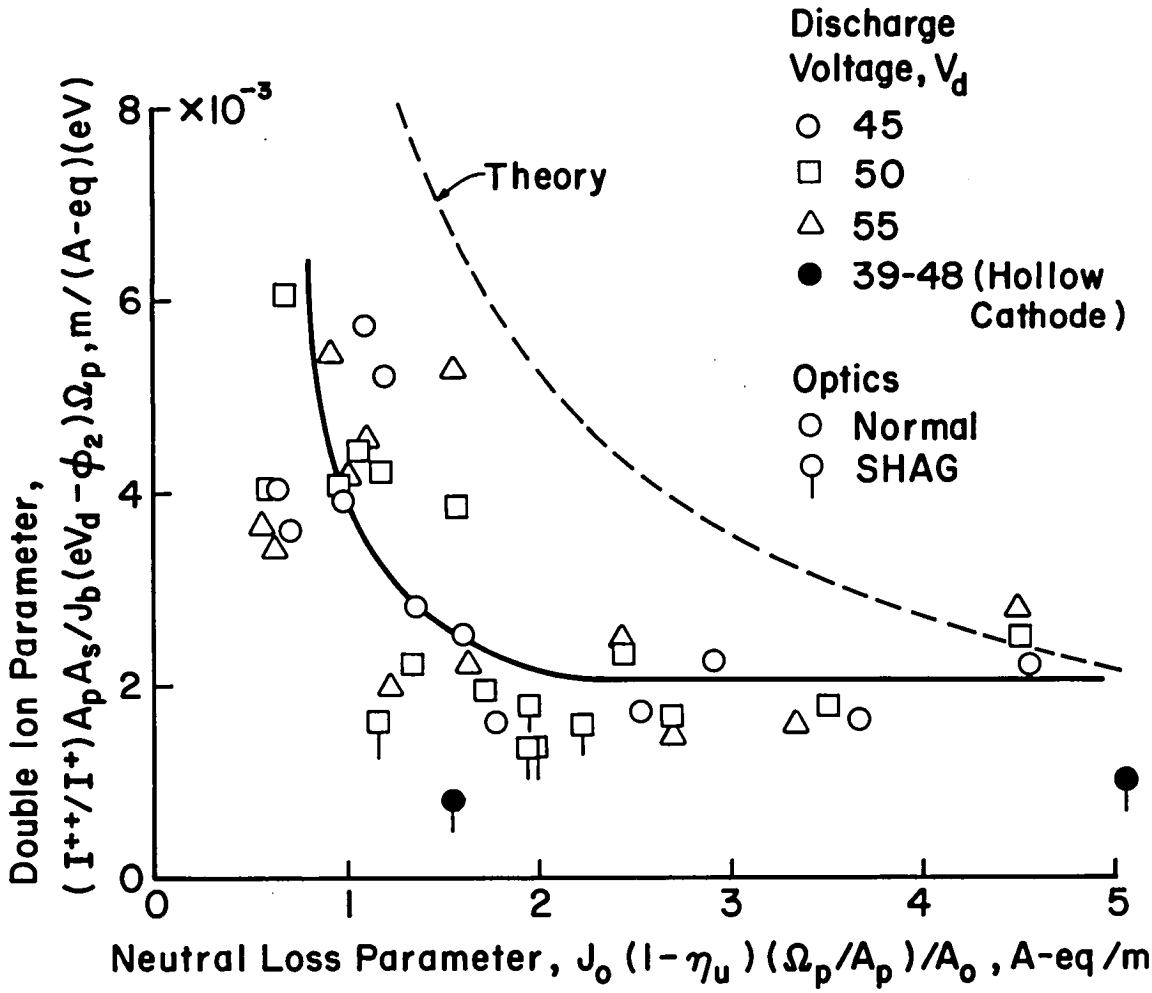

Fig. 3-10. Double ion correlation for argon, showing comparison with theory for large thrusters.

lower in Fig. 3-10. It is probably significant that coupling voltages (cathode to adjacent plasma) are larger for argon than for xenon.

From the data correlations presented in Figs. 3-9 and 3-10, the double ion production of a multipole discharge chamber can be predicted from overall performance parameters and geometrical considerations of the discharge chamber and ion optics. The experimental data were all obtained with 15-cm diameter discharge chambers. The theoretical curves in Figs. 3-9 and 3-10 were included to indicate the trends that would be expected for much larger thrusters.

IV. HOLLOW CATHODE RESEARCH

by Donald C. Trock

A series of tests were performed on hollow cathodes using argon as the propellant. With a view toward using this type of cathode in a new generation of larger thrusters, the tests investigated the operational characteristics with discharge currents up to 20 amperes. The objective in these tests was to optimize hollow cathode operation for minimum propellant flow and minimum discharge voltage.

The first group of data were gathered to determine or verify the optimum positions of the insert, keeper and anode used in the "conventional" hollow cathode used for the remaining tests. The second group of data presents the operational characteristics with an enclosed keeper replacing the more usual ring keeper. Both of these groups of data were obtained with a boron nitrude block around the neutralizer tip. The final group of data represents baseline characteristics taken with the hollow cathode returned to "conventional" configuration, but without the boron nitride block. A comparison is also made using a "post" (straight wire) keeper in place of the ring keeper. Some observations made with an oscilloscope are also described.

Apparatus and Procedure

All tests were performed in a vacuum facility with a 45 cm diameter bell jar (Fig. 4-1). A diffusion pump with a mechanical backing pump provided background pressures not exceeding 5×10^{4} torr at the highest argon flow rates used, and typically 1×10^{-4} torr at 500 mA-equiv. argon flow. No-flow pressures of 1×10^{-6} torr could be achieved.

Electronic grade E-1 argon was used with flow rates electronically set and regulated by a solid state flow control system designed and fabricated under the previous support period of this grant.

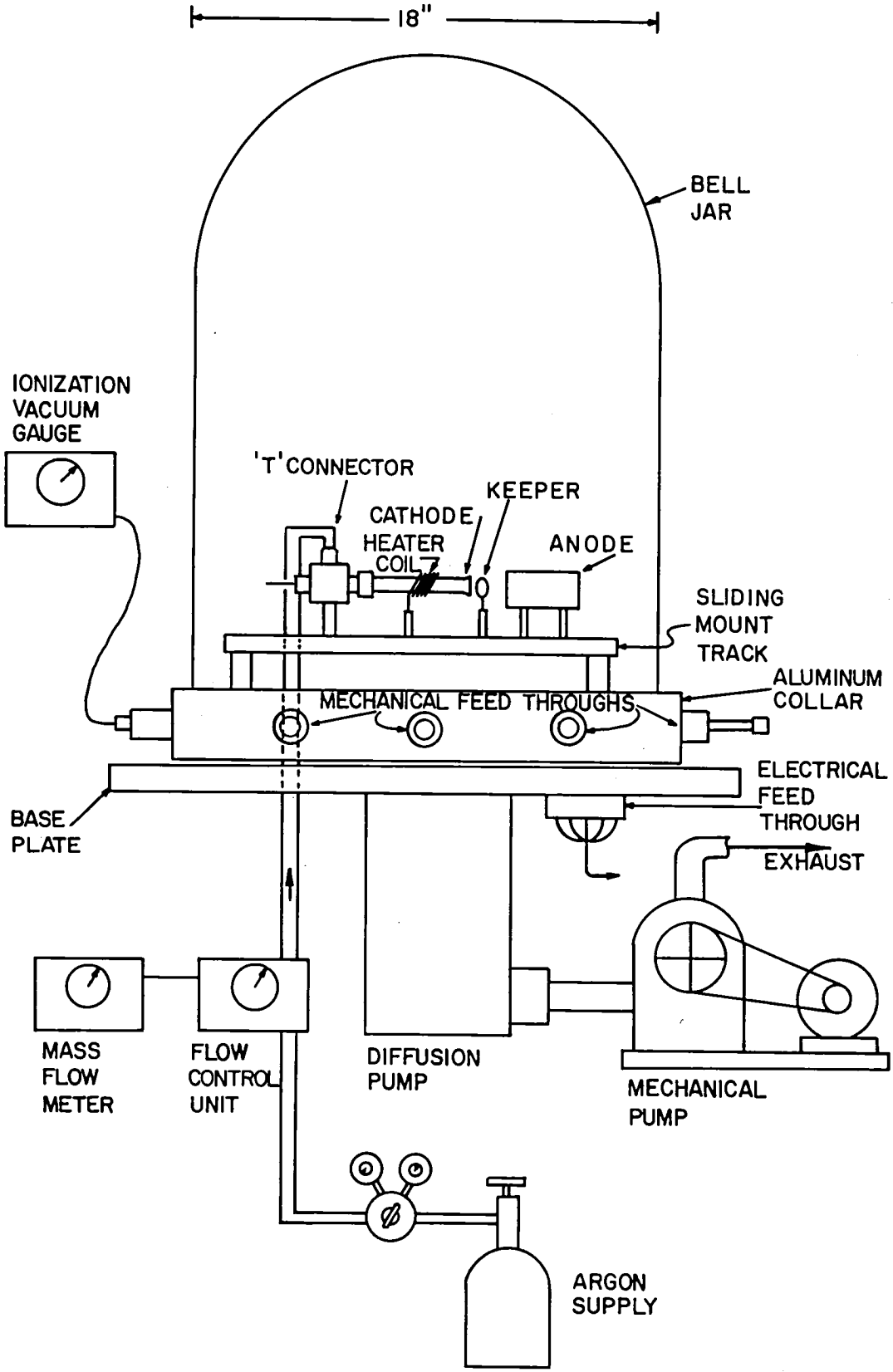

Fig. 4-1. Vacuum facility.

An aluminum collar 4 inches in height mounted between the glass bell jar and the steel base plate provided ports for mechanical feedthroughs to manipulate the test components during operation.

A hollow cathode (Fig. 4-2) was assembled and mounted with a cylindrical anode within the bell jar. With the cathode body held fixed, the insert position, keeper position, and anode position could be varied with relation to the orifice plate by means of the mechanical feedthroughs during operation. For the initial tests, a boron nitride cylinder surrounded the tip of the cathode leaving the orifice plate exposed. This boron nitride cylinder provided electrical insulation to permit mounting an enclosed keeper (Fig. 4-3). A tantalum sheathed tungsten heater coil was mounted adjacent to the boron nitride cylinder to provide initial starting temperatures. A thermocouple was spot-welded to the orifice plate to monitor operating temperatures.

Power supplies and instrumentation are shown schematically in Fig. 4-4. The anode power supply was usually operated in the current limited mode to permit positive control of discharge current while monitoring the discharge voltage. In a few cases, where the discharge voltage changed rapidly for small changes in discharge current, the voltage limited mode was used. This anode power supply could provide up to 60 V. The keeper power supply could provide up to 500 V to enhance initial starting and was placed in series with a variable resistance to restrict keeper operating current to 0-450 mA.

The oscilloscope connected to the keeper element was found to be useful to monitor the stability of operation of the cathode. During stable operation, a few volts of continuous white noise was observed, while marginal operating conditions would typically result in low

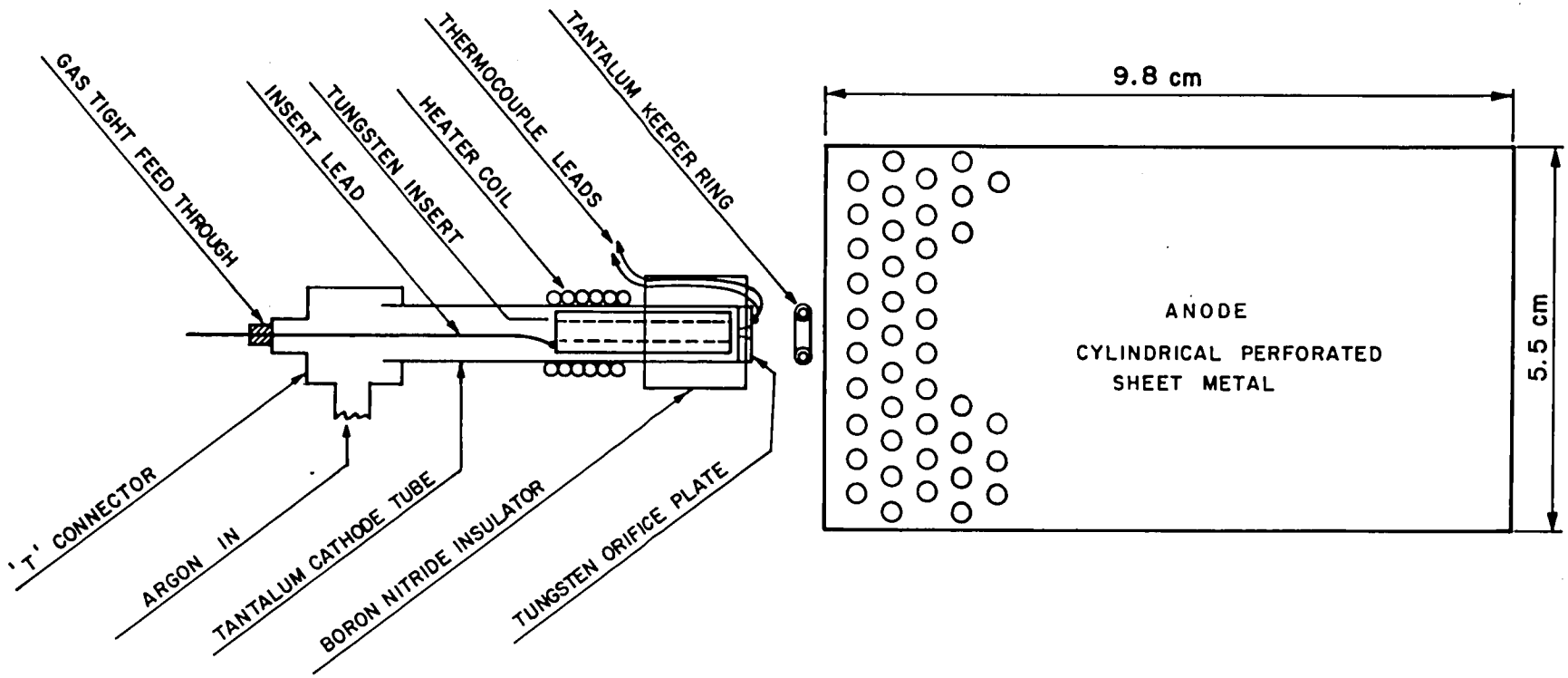

CATHODE : 6.35 mm DIAMETER Ta TUBE, TUNGSTEN ORIFICE PLATE, 0.76mm CHAMFERED ORIFICE.

KEEPER : Ta WIRE RING 4 mm INTERNAL DIAMETER, VARIABLE IN POSITION 0 – 3 cm FROM ORIFICE PLATE.

INSERT : SINTERED TUNGSTEN CYLINDER 25 mm LONG, 5 mm DIAMETER OUTSIDE, 4 mm DIAMETER INSIDE, VARIABLE IN POSITION 0 – 2 cm FROM ORIFICE PLATE.

INSULATOR: BORON NITRIDE CYLINDER 17 mm IN DIAMETER SURROUNDING CATHODE TIP FOR ELECTRICAL ISOLATION OF ENCLOSED KEEPER USED IN COMPARISON TESTS.

ANODE : 5.5 cm DIAMETER CYLINDER 9.8 cm LONG, CONSTRUCTED OF PERFORATED SHEET METAL, VARIABLE IN POSITION 0 – 3 cm FROM ORIFICE.

Fig. 4-2. Inert gas hollow cathode configuration.

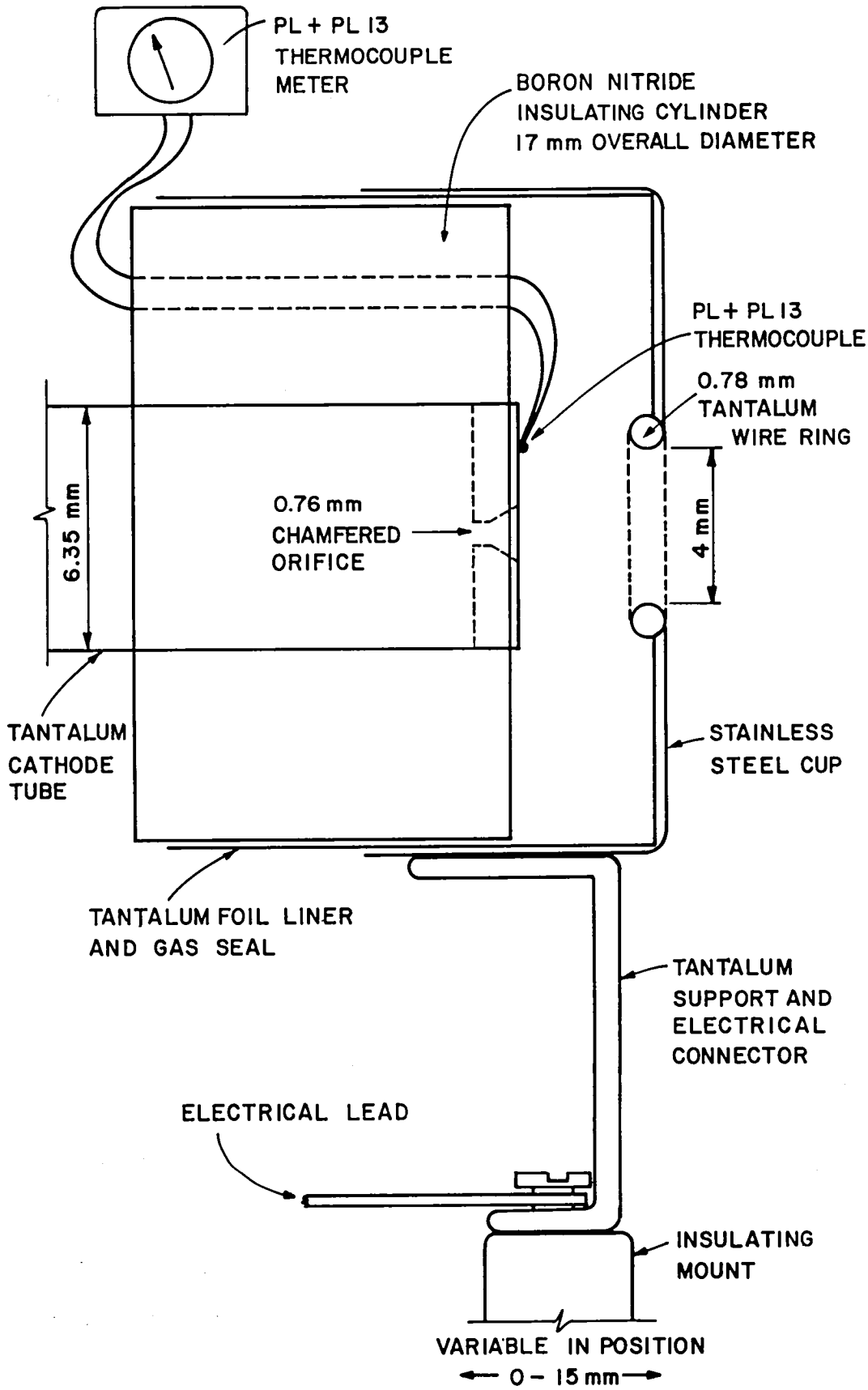

Fig. 4-3. Enclosed keeper configuration.

frequency modulation patterns on the white noise. This permitted identification of marginal operating conditions often not otherwise apparent from visual observations of the cathode or monitor meters.

All voltages and currents for the anode, keeper, and heater were monitored during all tests by calibrated panel meters. Cathode orifice plate temperatures were continuously monitored by a thermocouple connected to a calibrated direct indicating panel mounted meter. Argon flow was monitored by a mass-flow meter which is an integral part of the flow control system. This mass-flow meter was calibrated to indicate argon flow in mA-equiv.

The primary characteristic used to evaluate the effectiveness of introduced variables was discharge voltage V_D versus discharge current I_D, although all parameters were recorded.

Position of Components

The initial series of tests were performed to determine the optimum positions of the assembled components. (See Fig. 4-2.) Arbitrary starting positions were selected as follows:

Insert - 1 mm from upstream surface of orifice plate.

Keeper (tantalum wire ring) - 2 mm from downstream surface of orifice plate.

Anode - concentric with cathode and with upstream edge of anode just even with the plane of the orifice plate.

With keeper current set at 300 mA, the current regulated anode power supply was set to either 1 A or 5 A as indicated on graphs. As each component was individually moved throughout its range, the resulting variations in anode voltage were recorded along with any variations in orifice plate temperature and keeper voltage.

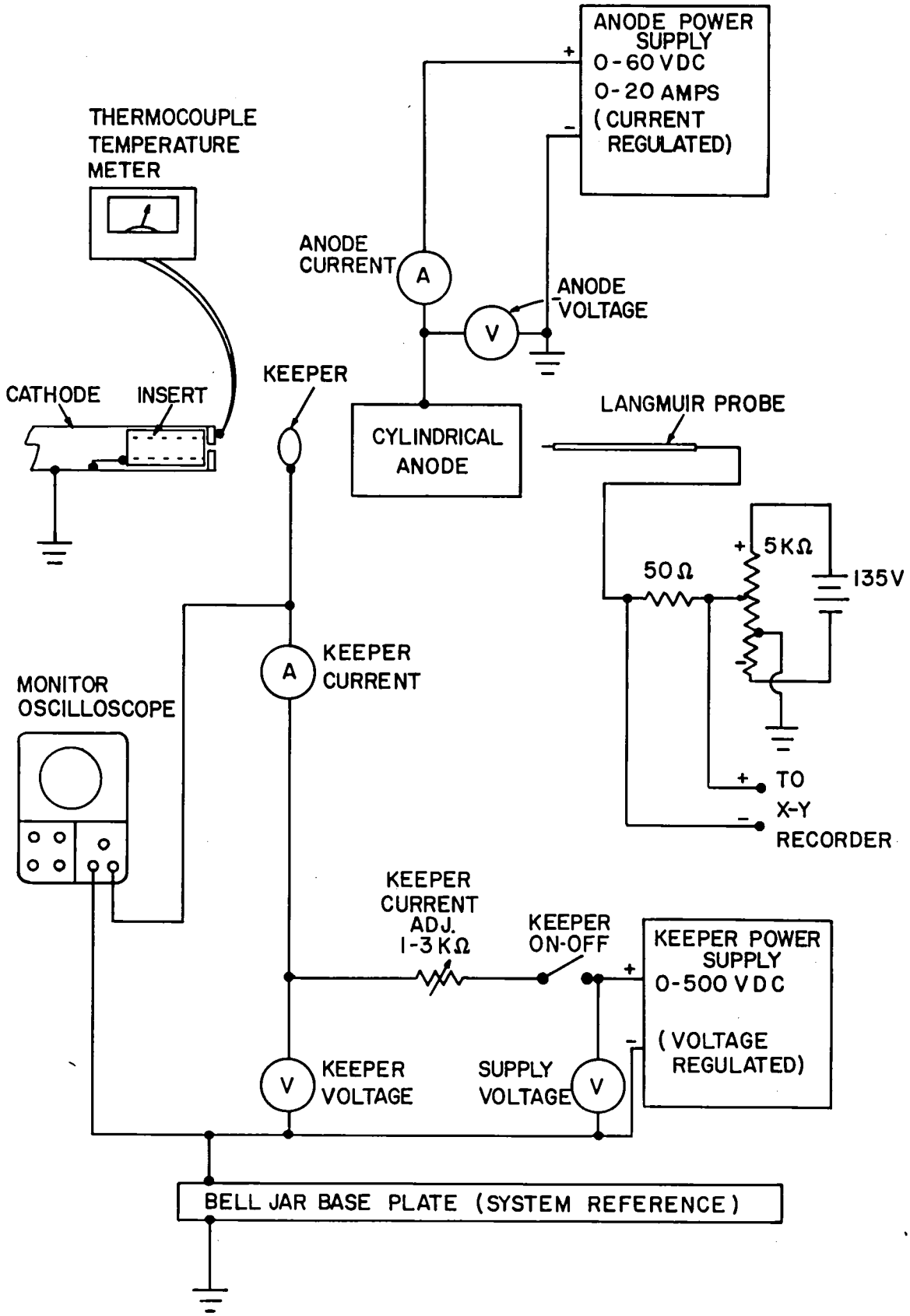

Fig. 4-4. Cathode circuit schematic.

Figure 4-5 shows the effect on anode voltage as the insert was moved with respect to the upstream surface of the orifice plate, while representative anode currents of 1 A and 5 A were maintained. The main feature of these results is the lack of sensitivity to insert position. It should also be noted that the easiest starting occurred when the insert was very close to, or in contact with, the upstream surface of the orifice plate. The insert was left in contact with the orifice plate for all other tests.

It should be noted that the data taken with 1 A of anode current required the use of the external heater to maintain an orifice plate temperature close to 1000°C. The value of 1000°C was selected as being high enough for normal operation, but not so high as to cause excessive evaporation of the oxide. At 5 A of anode current, sufficient internal heat was generated to permit the external heater to be turned off with orifice plate temperature reaching as much as 1050°C. The results shown, although abbreviated, do not appear inconsistent with the views of Siegfried and Wilbur,[1,2] who present a view of internal emission as a combination of thermionic and field enhanced emission, with the principal site of electron emission within a few millimeters of the upstream surface of the orifice plate. More complete tests are required to determine optimum pressures and insert configurations for argon hollow cathodes operated at high emission currents. Siegfried and Wilbur also present strong evidence that the orifice and orifice plate may be treated separately from the insert as sources of emission and heat. Additional tests in this area could result in a model to aid in designing hollow cathodes for high current inert-gas applications.

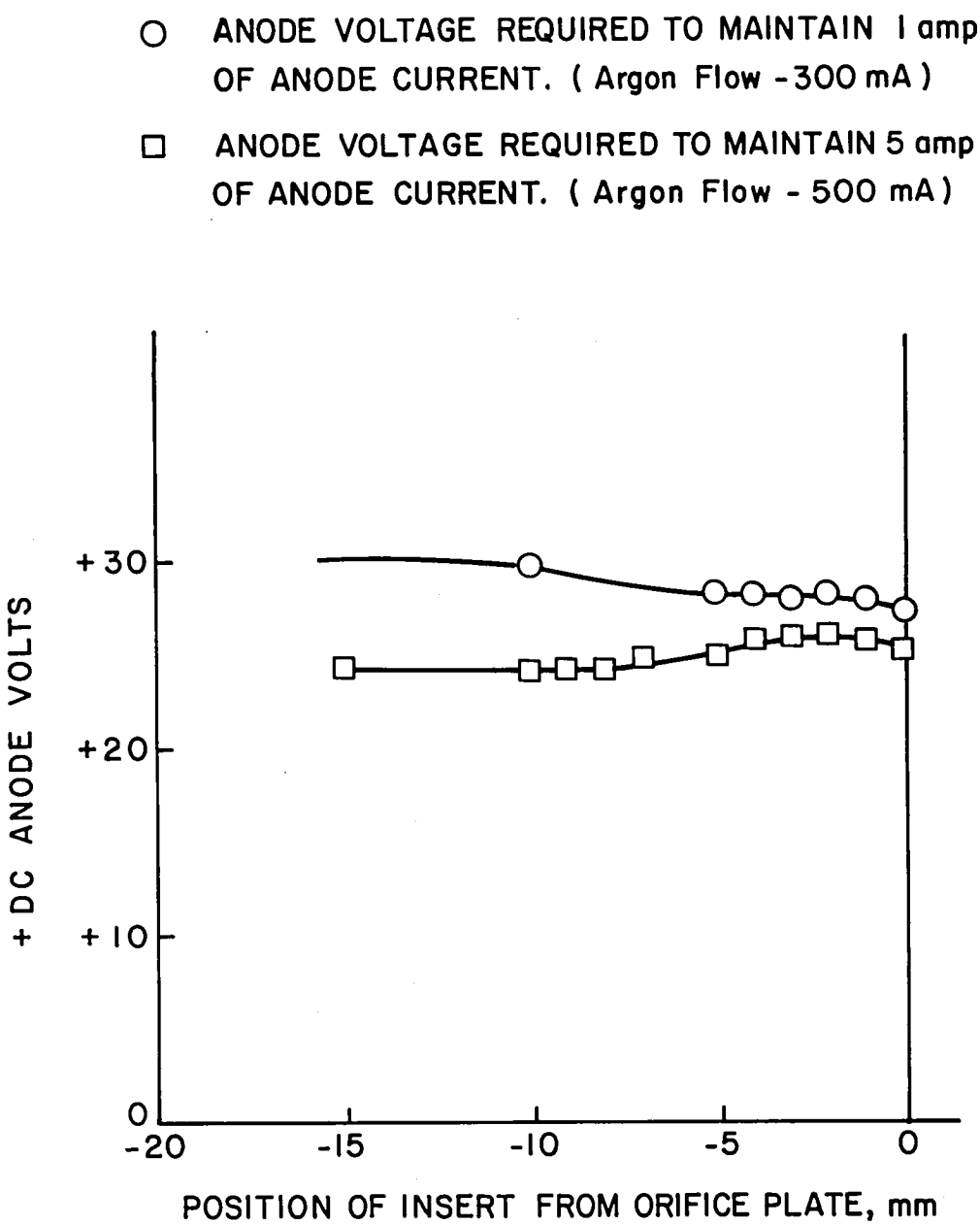

Fig. 4-5. Operating characteristics as a function of insert position.

Figure 4-6 shows the results of varying keeper position with respect to the orifice plate for one representative set of operating conditions. For this test, anode current was set at 5 A and keeper current at 0.3 A, and anode voltage and keeper voltage were monitored as the keeper position was adjusted. It was noted during all tests that the keeper should be within 1 mm of the orifice plate to enhance initial starting of the cathode. Since the data indicate that within 5 mm, a close keeper proximity also results in a lower anode voltage for a given anode current, the keeper was positioned 1 mm from the orifice plate for all subsequent tests.

As shown in Fig. 4-7, with the keeper positioned 1 mm from the orifice plate, varying keeper current had only a small effect on anode voltage for low anode currents (below 2 A), and no apparent effect at higher anode current. Except to maintain cathode emission during very marginal operating conditions, the keeper could be turned off or physically removed once the cathode was started with little or no effect on cathode operation. For better comparison with past data the keeper was operated at 300 mA for subsequent tests.

Varying the position of the anode over its 3 cm range produced only minor variations of less than 1 V of anode voltage, so it was arbitrarily positioned so that the cathode protruded 1 cm into the center of the cylinder for all remaining tests.

Enclosed Keeper Versus Ring Keeper

The primary purpose of this series of tests was to compare cathode operation using a tantalum wire ring keeper with cathode operation with

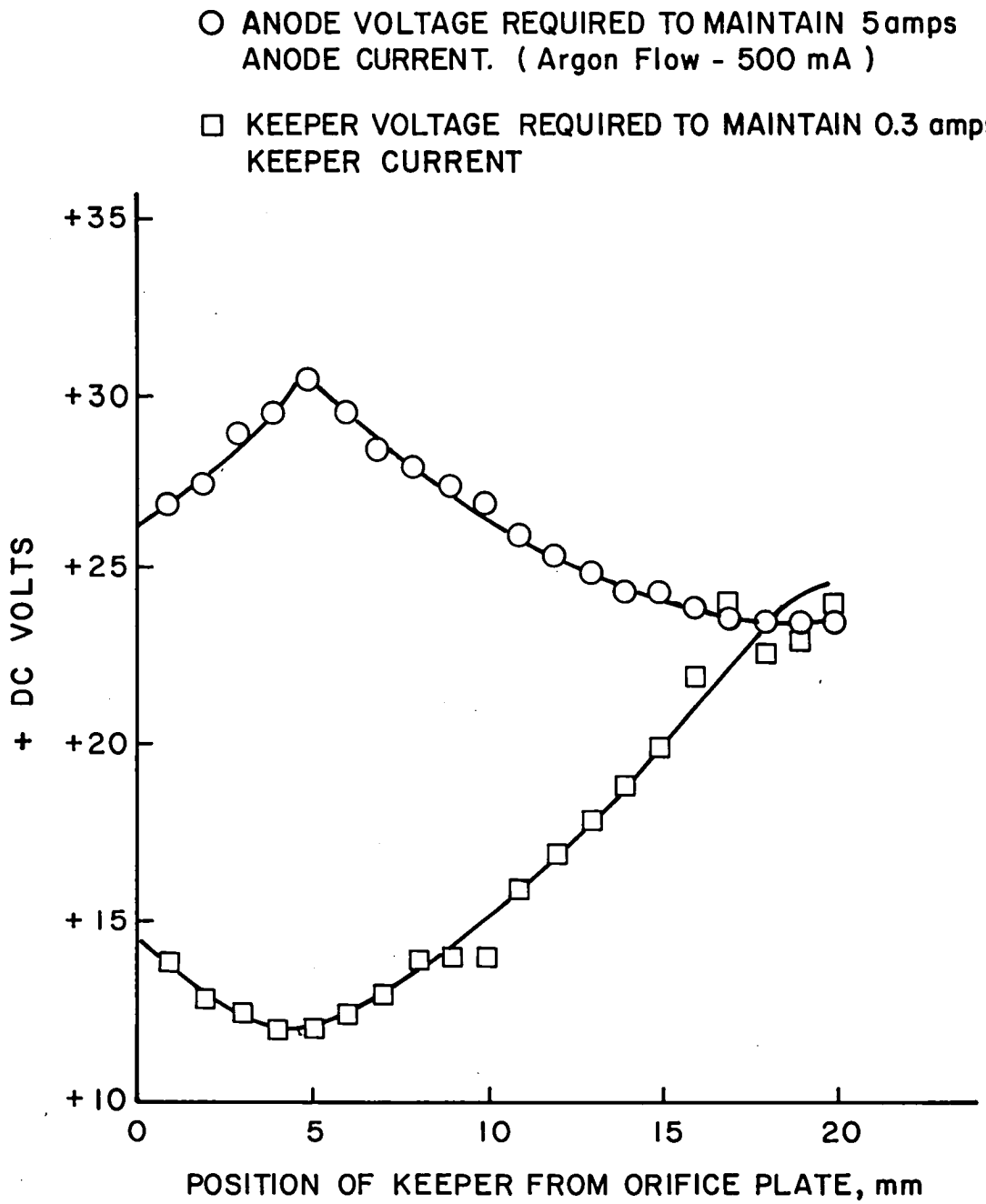

Fig. 4-6. Anode potential and keeper potential as a function of keeper position with anode and keeper currents held constant.

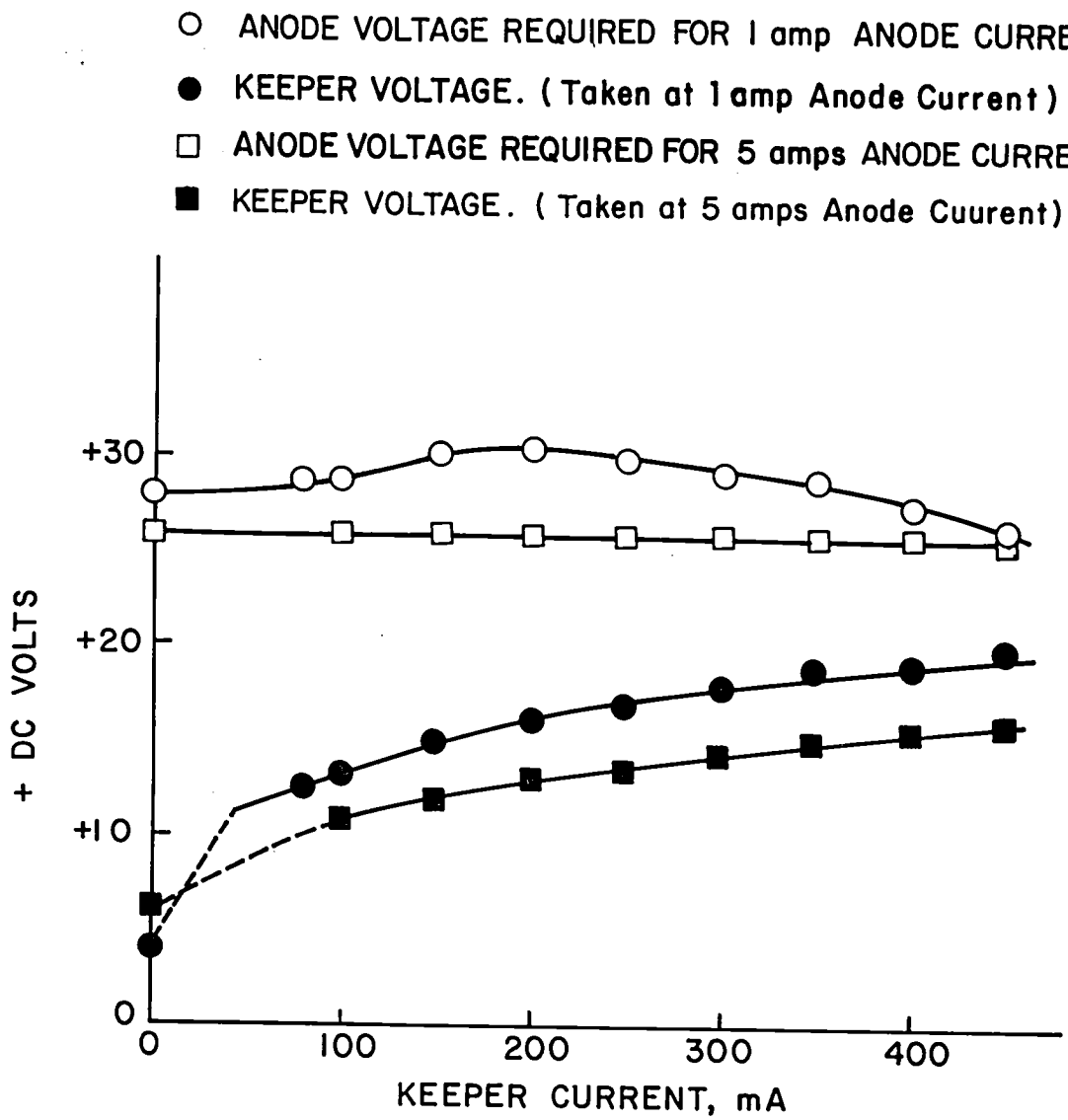

Fig. 4-7. Anode and keeper potential as a function of keeper current with anode current held constant.

an enclosed keeper. As the tests were repeated at several different flow rates, the data also provided a baseline for comparison against future variables.

Figures 4-8 and 4-9 display anode voltage versus anode current characteristics for the cathode operating with a tantalum wire ring keeper installed, while Figs. 4-10 and 4-11 show comparative data with the enclosed keeper installed. (See Fig. 4-3 for enclosed keeper detail.) In general, the use of an enclosed keeper did not cause any large change in operating characteristics. As shown in Fig. 4-12, however, it did raise orifice plate temperature approximately 100°C. Perhaps most important was the increased maximum emission at high propellant flow rates that was obtained with the enclosed keeper.

To determine what effect the boron nitride insulating cylinder may have had, it was removed, leaving the external heater in its original position 1 cm from the cathode tip. Another series of tests, as shown in Figs. 4-13, 4-14 and 4-15, reveal voltage and current characteristics similar to the previous tests, but as shown in Fig. 4-16 the orifice plate temperatures were approximately 50°C higher than the enclosed keeper tests. Boron nitride is known to be a reasonably good conductor of heat and was apparently providing some heat sinking effect for the cathode tip.

The cathode operating characteristics show that for each flow rate there is a well defined maximum current point. Since this maximum current point can be shifted somewhat by operating temperature, it is possible that this current limit is a function of cathode internal pressure, and possibly internal component dimensions as well.

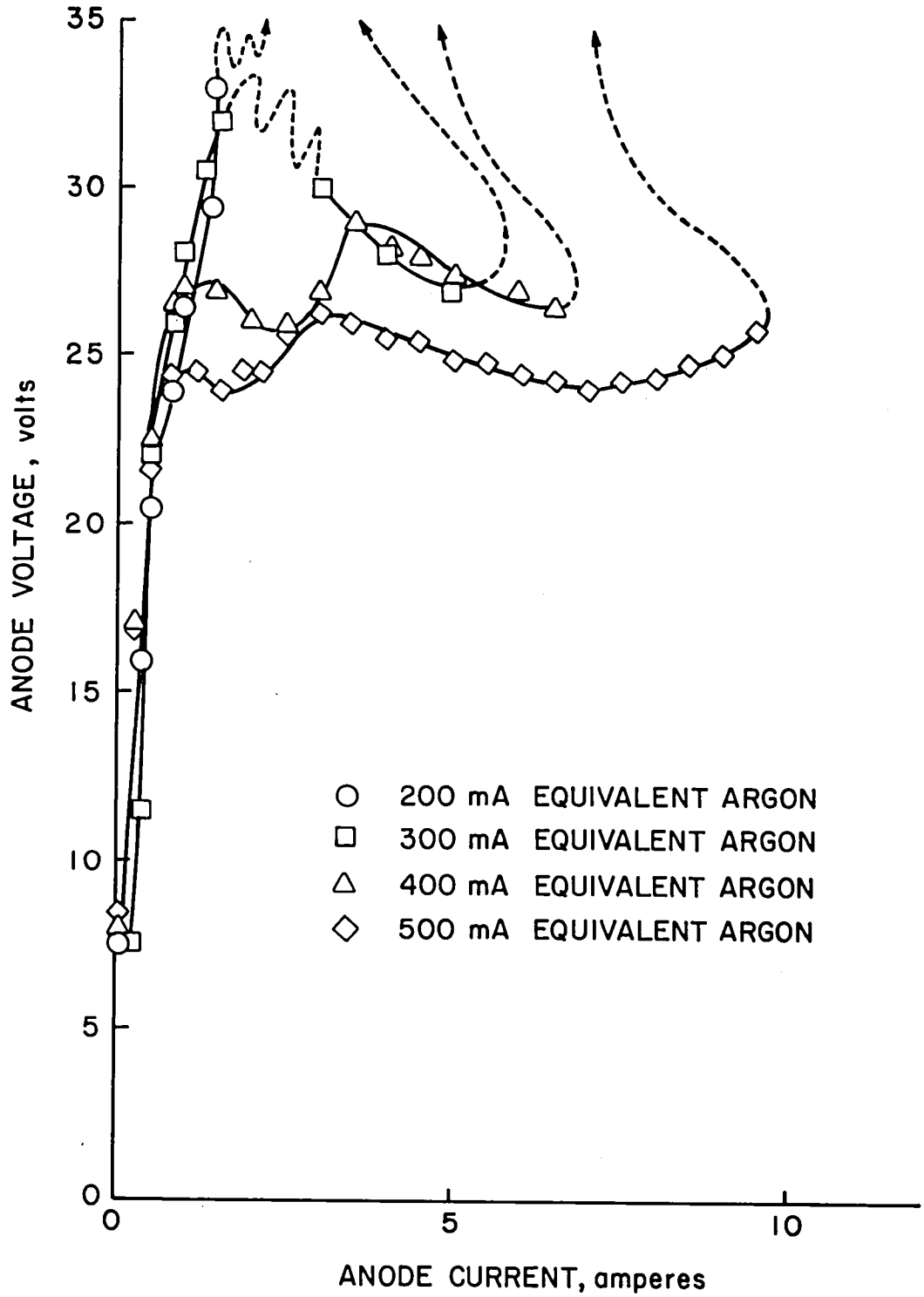

Fig. 4-8. Effect of Ar flow on cathode characteristics for ring keeper.

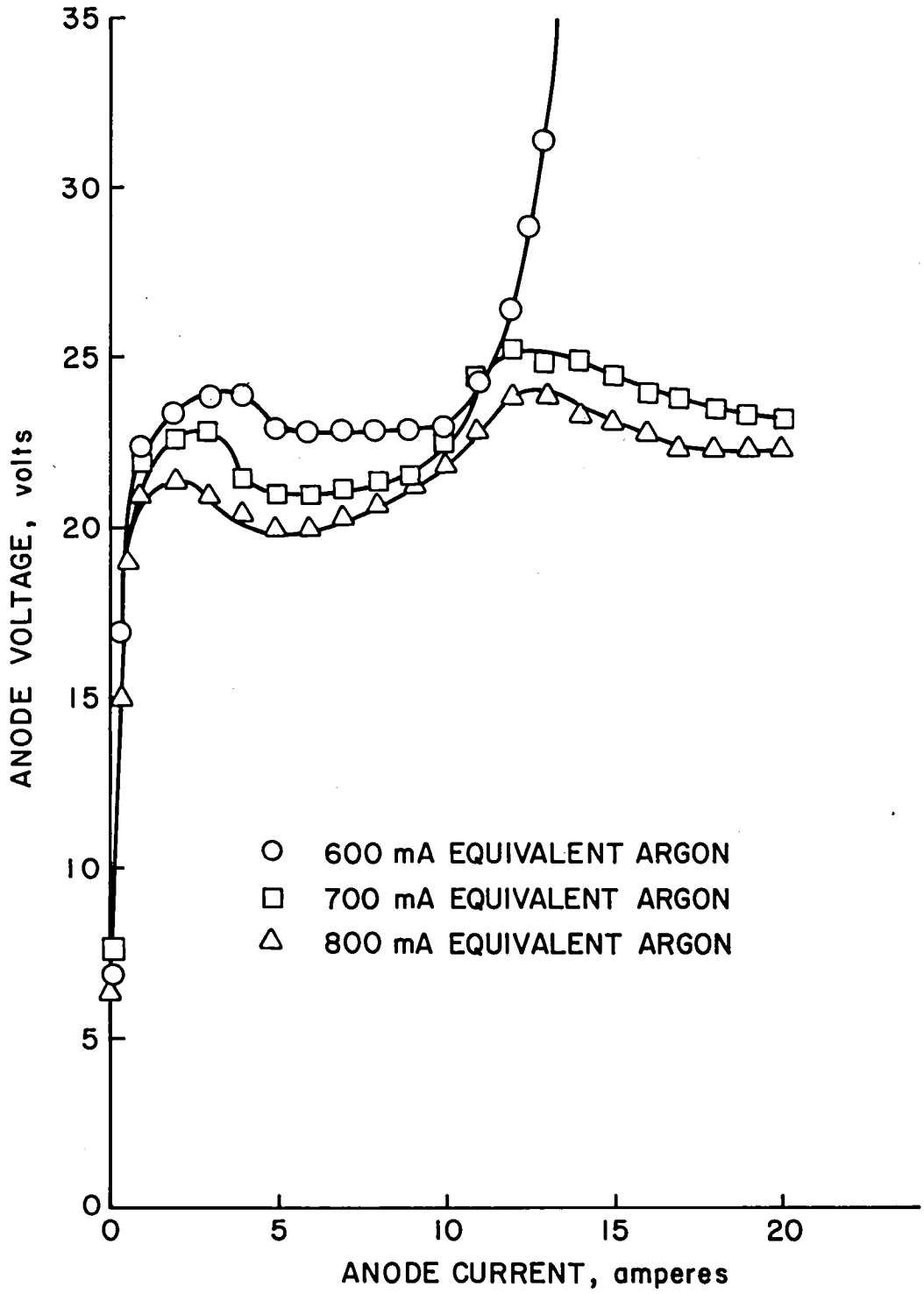

Fig. 4-9. Effect of Ar flow on cathode characteristics for ring keeper.

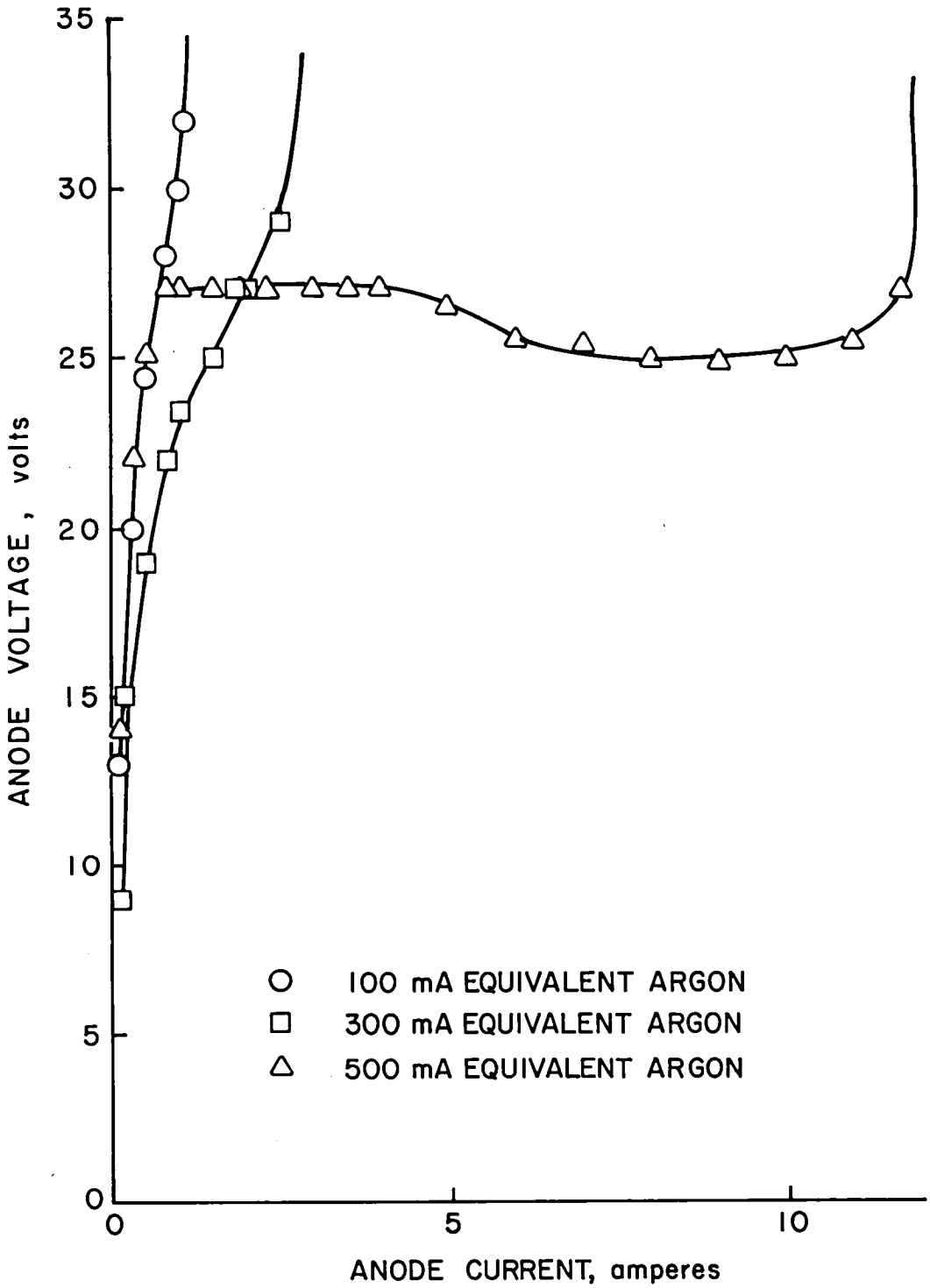

Fig. 4-10. Effect of Ar flow on cathode characteristics for enclosed keeper.

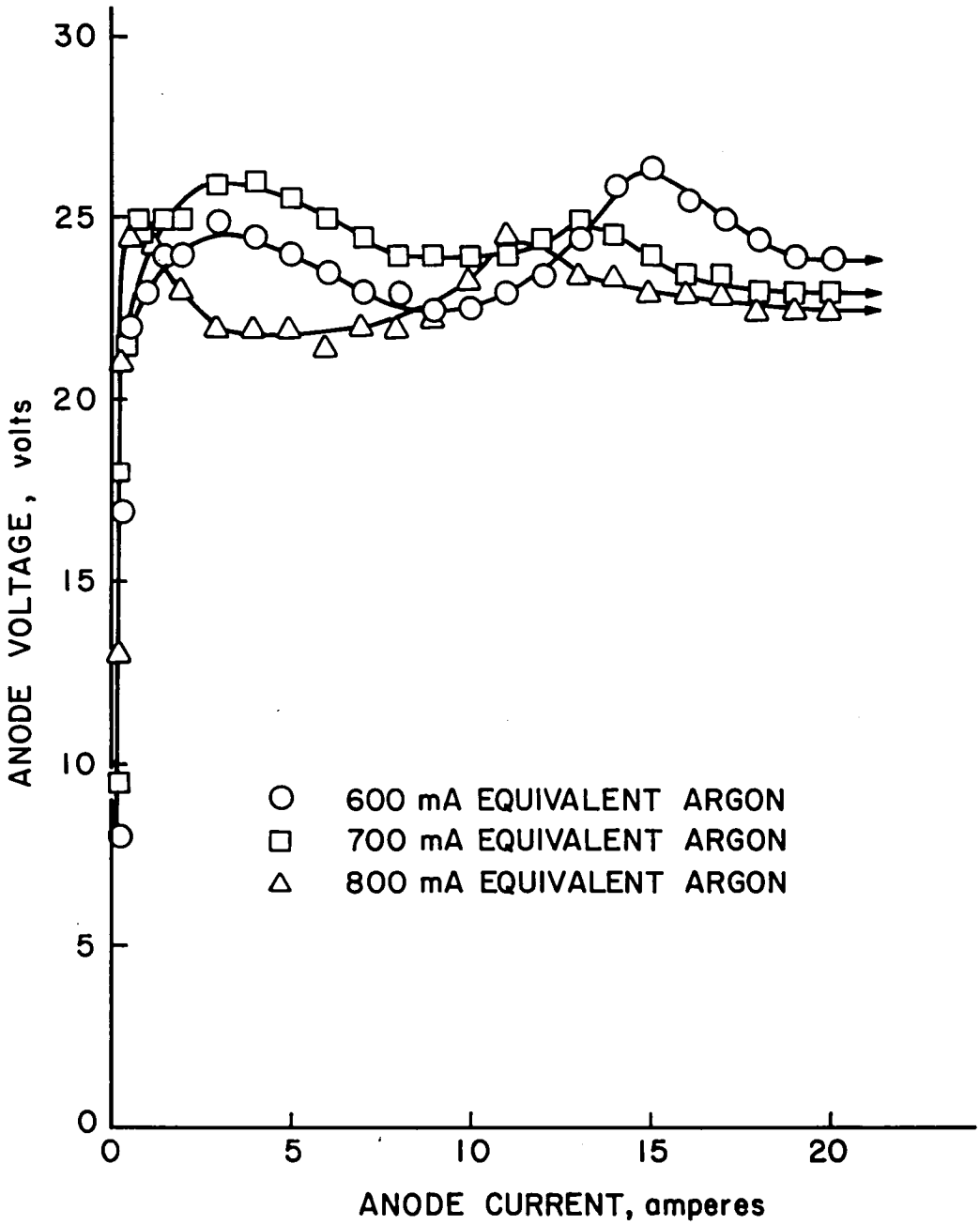

Fig. 4-11. Effect of Ar flow on cathode characteristics for enclosed keeper.

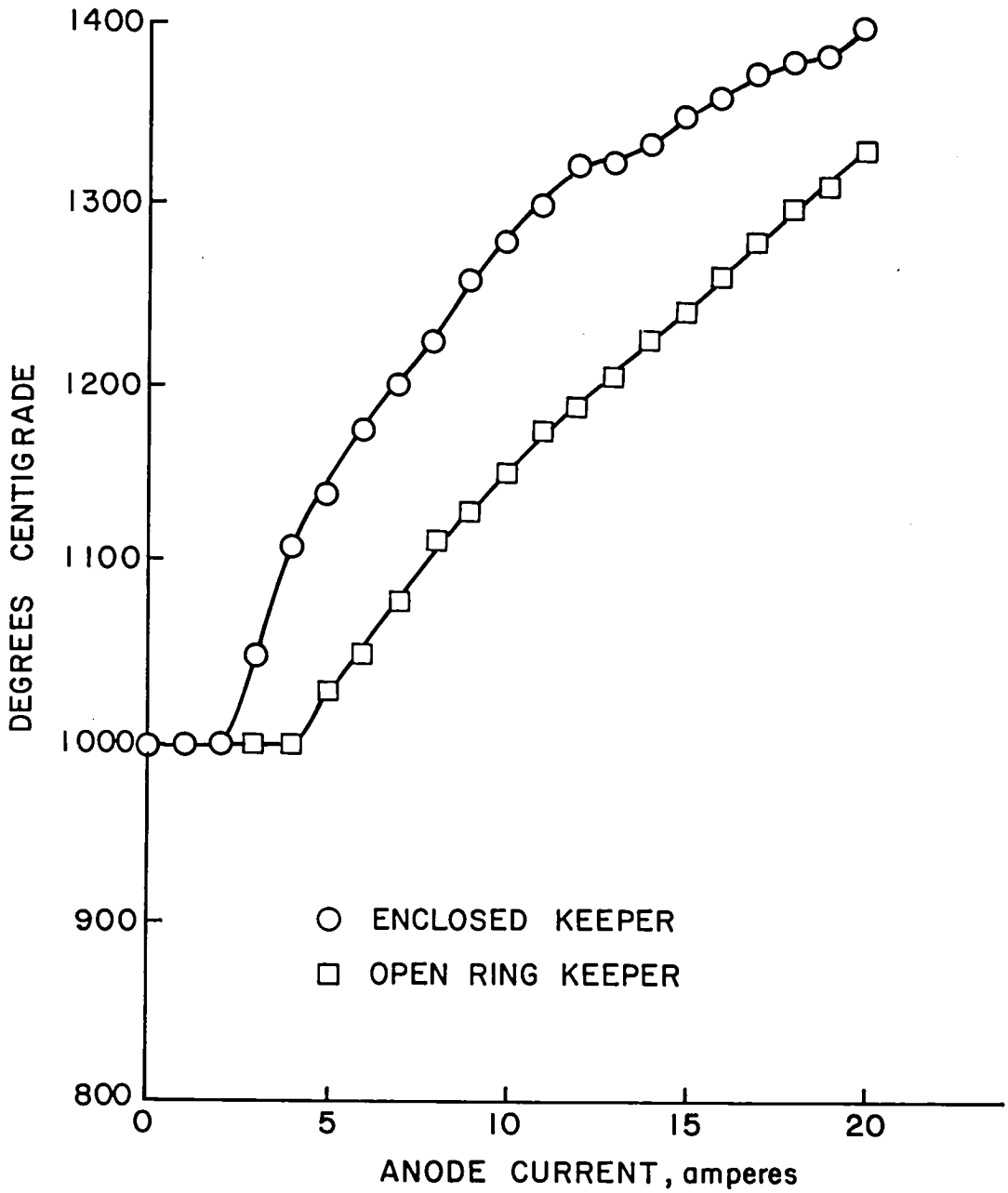

Fig. 4-12. Orifice plate temperature as a function of anode current for ring keeper and enclosed keeper.

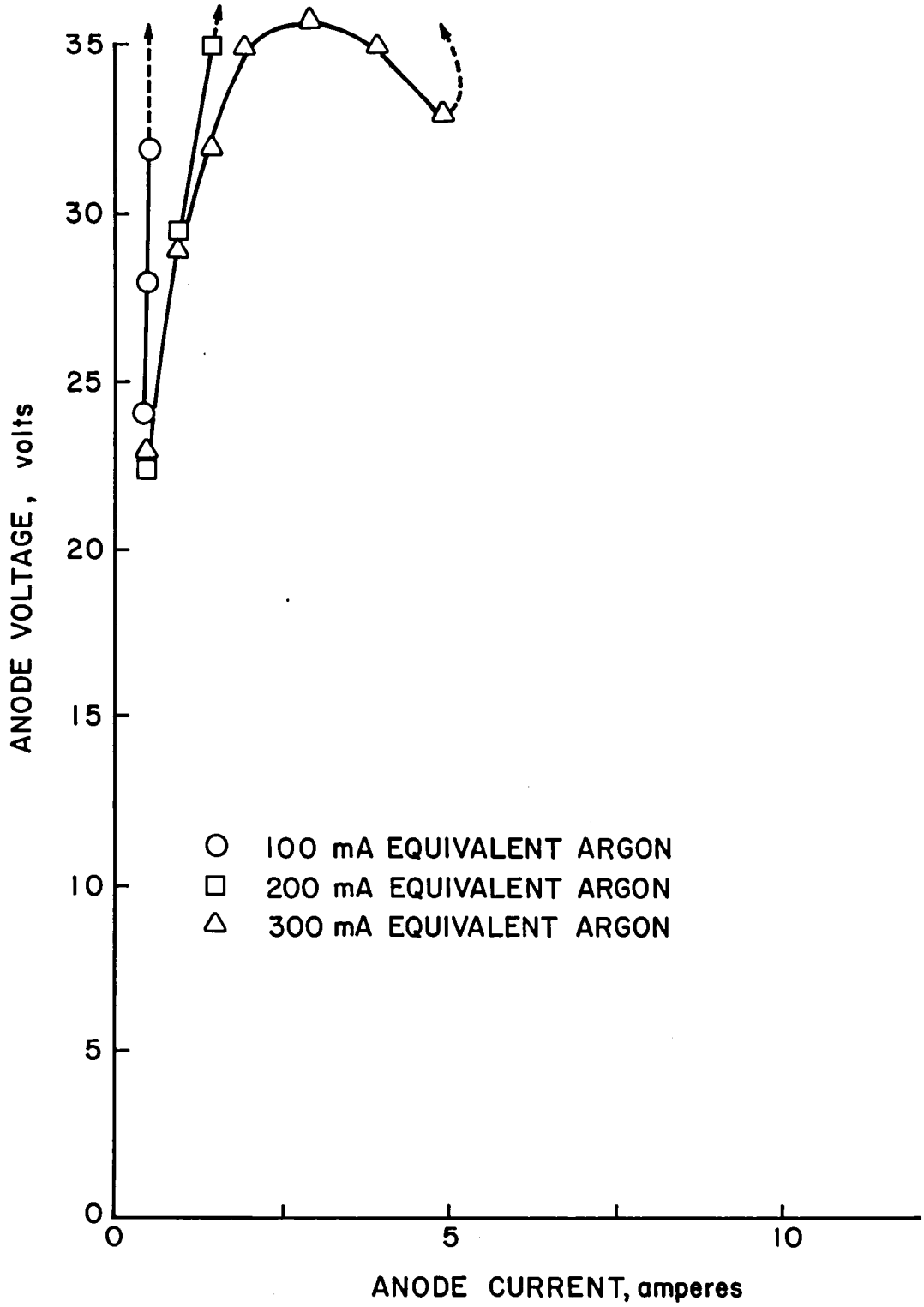

Fig. 4-13. Effect of Ar flow on cathode characteristics for ring keeper without heat sink.

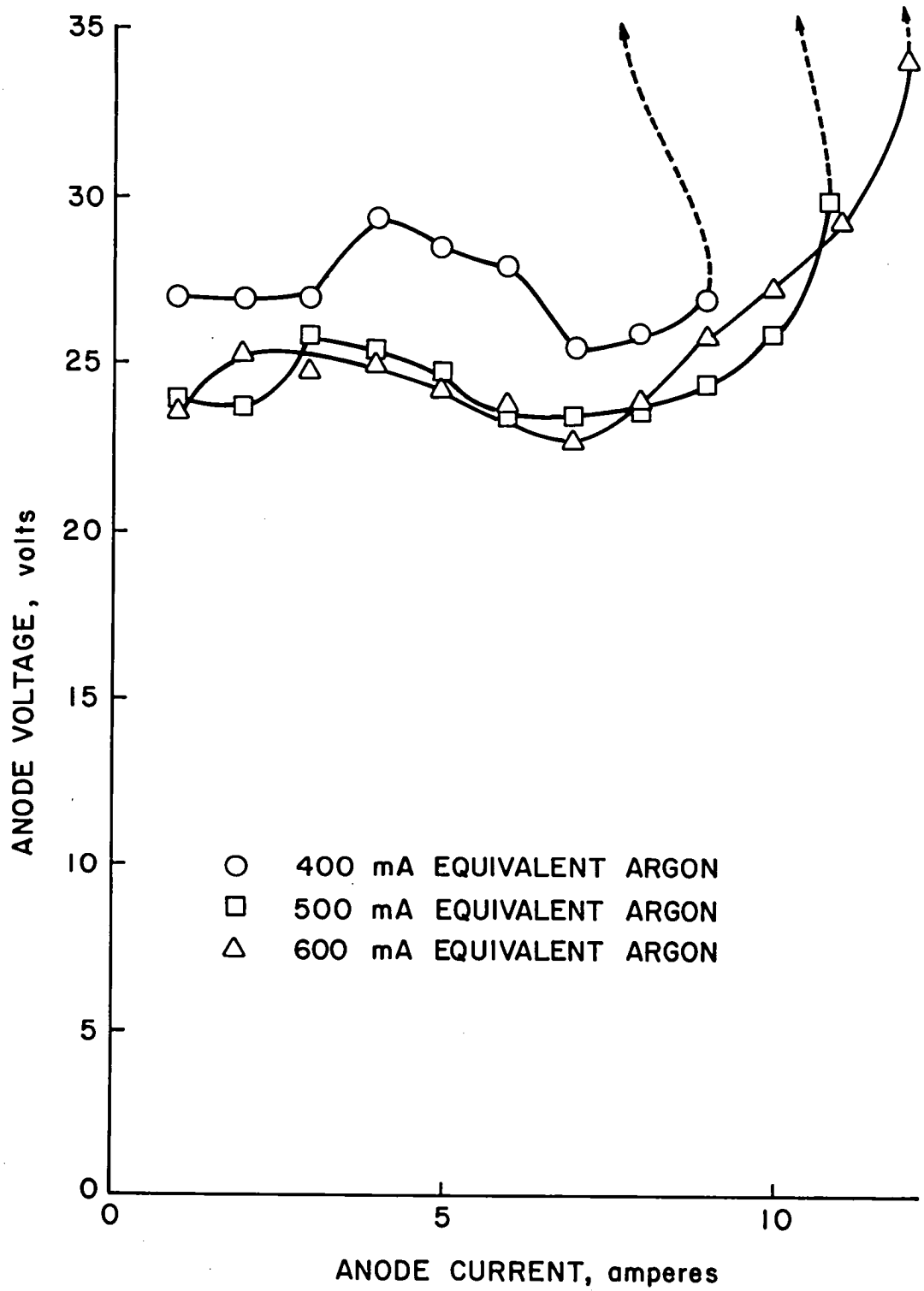

Fig. 4-14. Effect of Ar flow on cathode characteristics for ring keeper without heat sink.

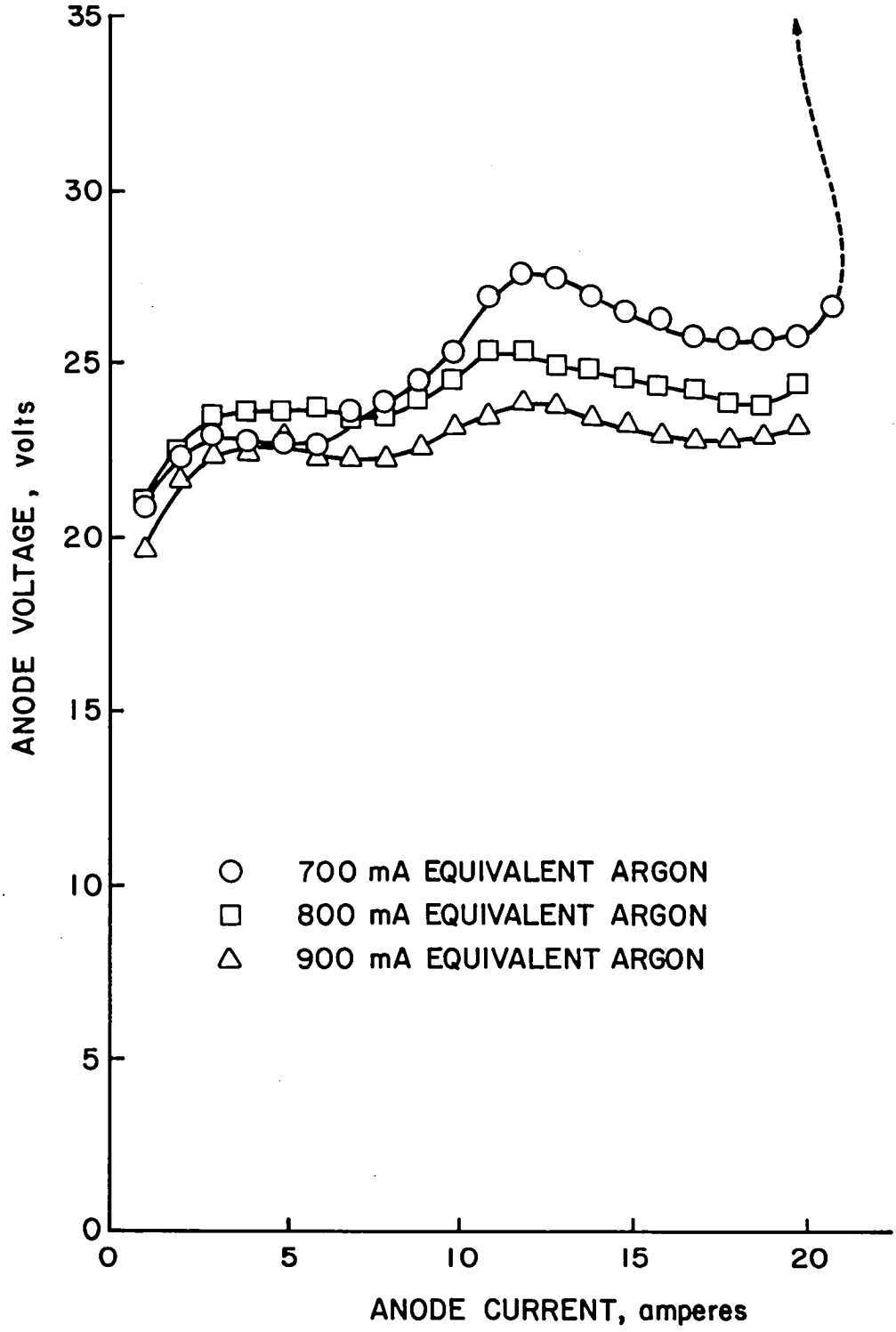

Fig. 4-15. Effect of Ar flow on cathode characteristics for ring keeper without heat sink.

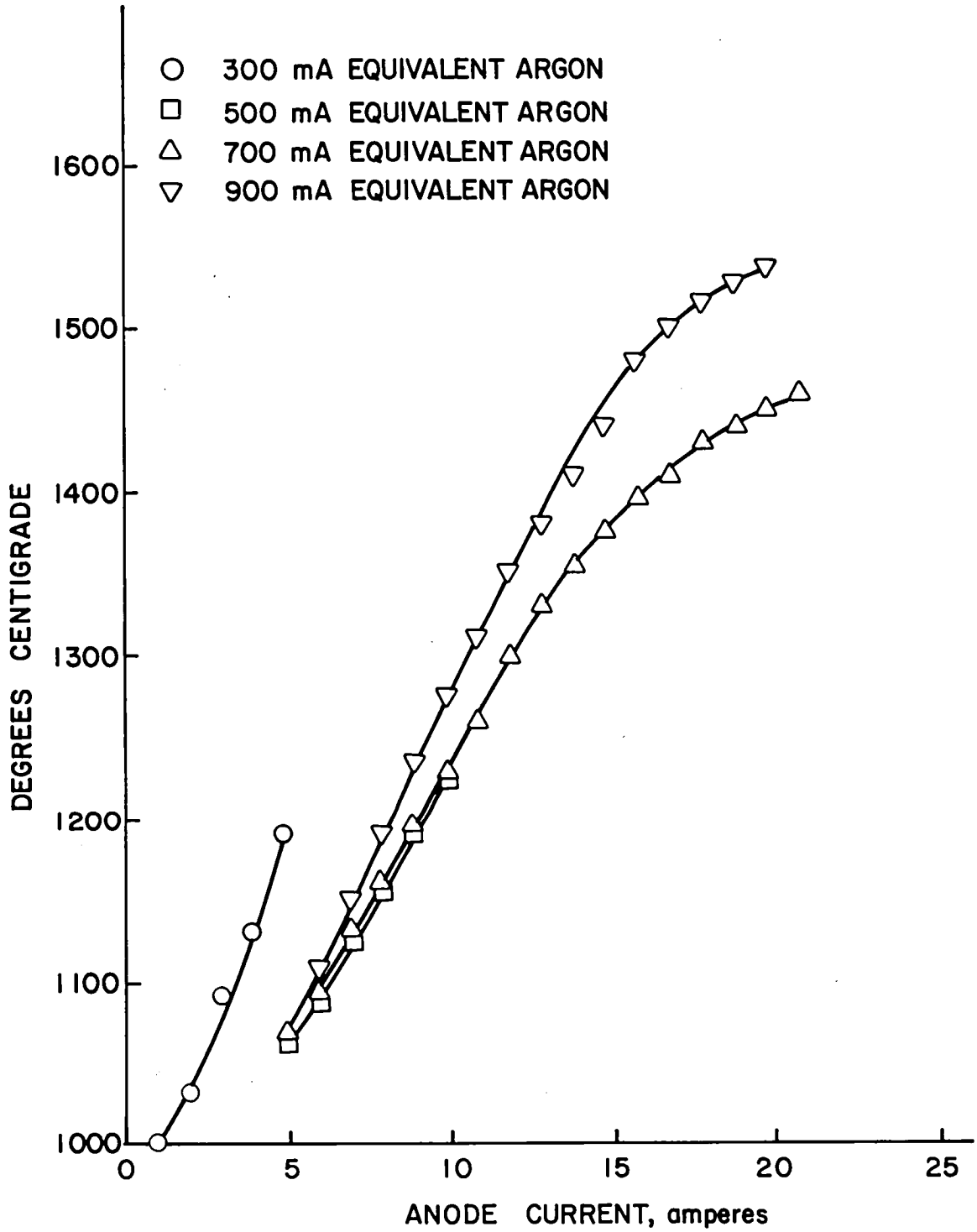

Fig. 4-16. Orifice plate temperature as a function of anode current for ring keeper without heat sink.

When a current limit is encountered in the current regulated mode, the power supply increases to its maximum voltage value of about 55 V without further increase in anode current, and in some cases a slight reduction in anode current. The normally clear and well defined plume exiting from the orifice becomes brighter but more diffuse, and the entire volume near the cathode, both inside and outside of the anode becomes lighted by glow discharge. Use of the voltage limited mode did permit some data to be obtained at the current limit, but operation was still erratic. It is not felt that this condition is directly related to the "plume" mode of mercury hollow cathodes or the similar "low current" (LI) regime of Delacroix and Trinade,[3] because neither of these modes has ever been reported as resulting from a discharge current increase when initially in the spot mode or equivalent. On the other hand, the brighter and more diffuse plume bears a strong resemblance to the plume mode. The similarity to plume operation also extends to the observance of increased electrical noise. During this high current condition, an oscilloscope connected to the keeper, anode, or a separate isolated probe displays a pattern of oscillations, as shown in Fig. 4-17. The bursts of high voltage, in this case from the high frequency noise, have a burst pulse width of approximately 5 msec, and a repetition rate of about 70 KHz. Voltage excursions of the bursts extend from about 40 V negative to over 300 V positive. Even when the oscilloscope was connected to the anode, these large voltages were observed. Because the maximum voltages exceeded DC power supply capability, some resonant phenomenon is probably involved. The observed burst repetition rate (about every 15 msec for the 70 KHz frequency) corresponds to an anode-cathode transit time for an argon ion of approximately 1 eV energy,

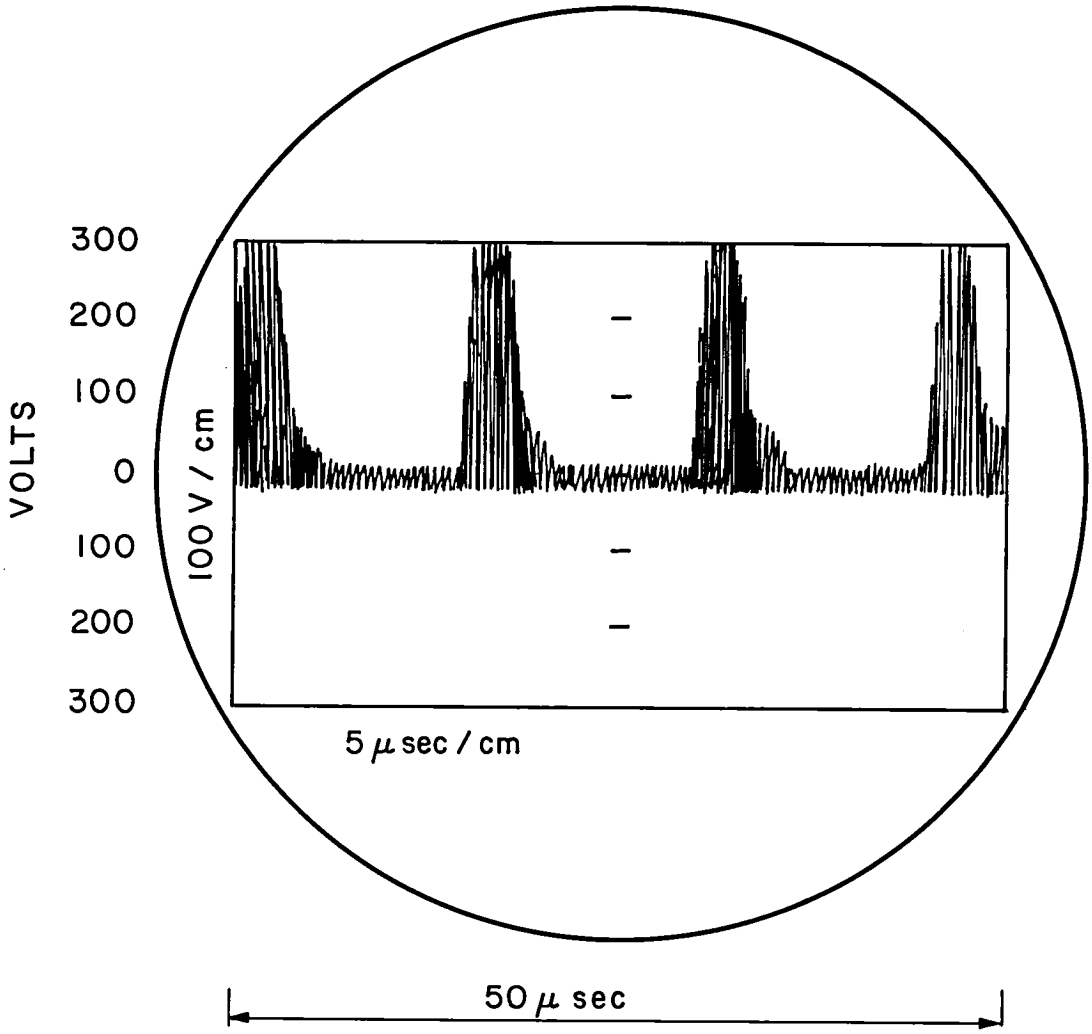

ANODE CURRENT = 10.5 amperes
ANODE VOLTAGE = 50 volts
ARGON FLOW = 500 mA EQUIVALENT
ORIFICE PLATE TEMPERATURE = 1290 °C

Fig. 4-17. Oscilloscope display when cathode is in current limited mode due to insufficient Ar flow.

which is about the plume electron temperature in the absence of oscillations. It is therefore proposed that the observed oscilloscope signal is the result of a population instability in the plume region. The large burst of noise is the result of electrons being injected from the anode or cathode into this region. The injection results in a rapid increase in plasma density, followed by cooling of the injected electrons. The ions escape consistent with cooled electron temperature. The electrons escape faster due to their higher velocity, eventually leading to a high plasma potential that produces another injection of electrons, etc.

The major assumption in this description of a population instability is that electrons are not readily available, or available only under certain conditions, from the cathode. A possible reason for this lack of electrons is that the discharge within the cathode becomes starved for electrons. In comparing mercury and inert-gas cross sections, the most noticeable difference is the much smaller collision cross sections for low energy electrons in inert gases (associated with the Ramsauer-Townsend effect). It is proposed that, at high emissions from inert-gas hollow cathodes, the electrons are extracted more rapidly than they are generated.

Figure 4-18 shows the current limits observed at each flow rate as a function of mass flow. It is conjectured that if these curves were normalized by the emission site temperatures, they might result in a near linear slope. This would support the views of Delacroix and Trinade[3] that emission site activity is affected by both pressure and neutral velocity. In any case, it is clear that higher ratios of emission to propellant flow are available at the higher propellant flow rates. Cathode performance for large thrusters may therefore be enhanced

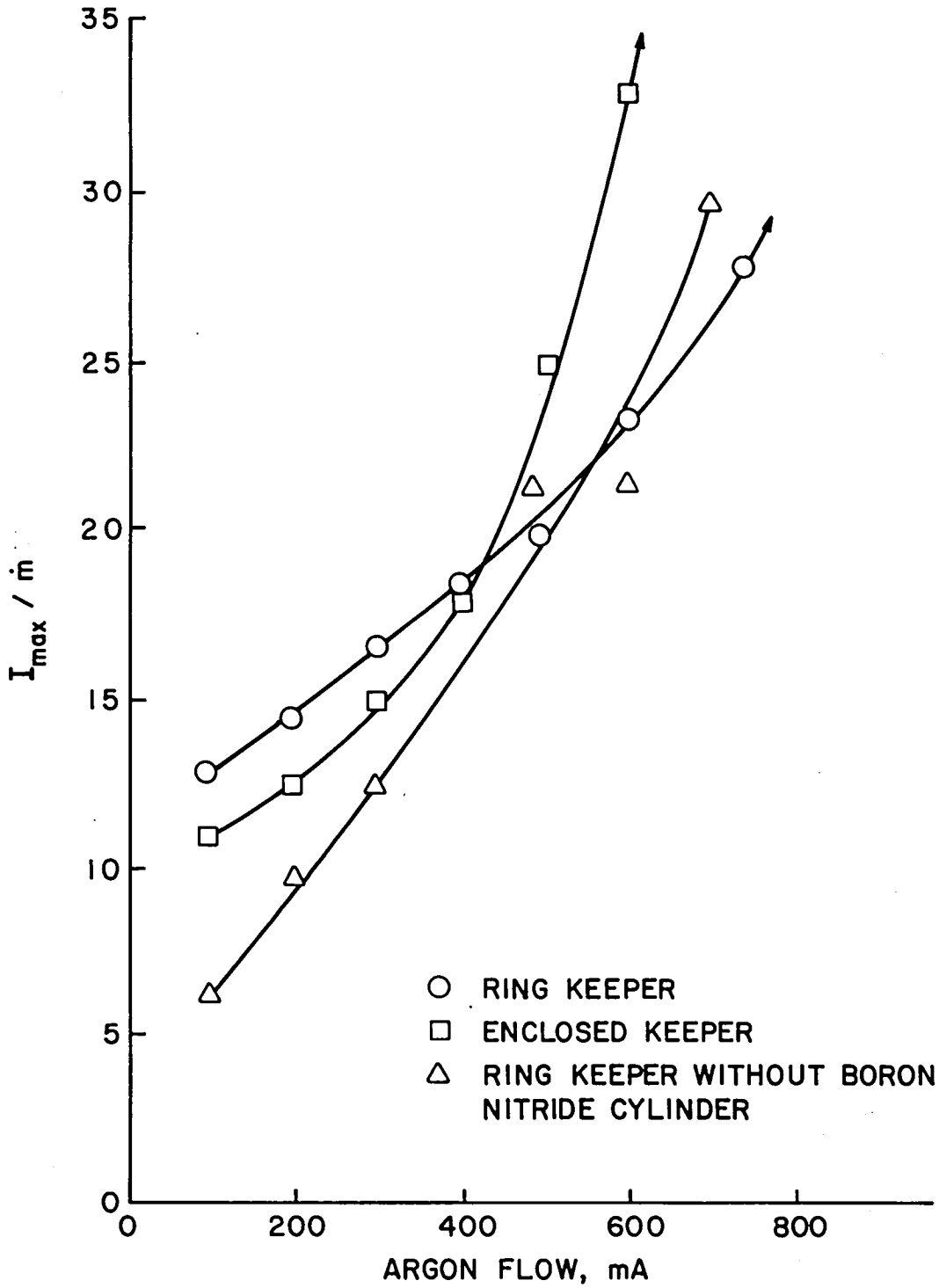

Fig. 4-18. Ratio of cathode emission current limit to Ar flow for different keeper configurations for a 0.75mm diameter orifice.

by increased flow rates, smaller insert diameters, and slightly larger orifices. These parameters should be among the first to be examined in future tests.

Of particular interest was the performance of the hollow cathode with an enclosed keeper in Fig. 4-18. The enclosed keeper offers an increased restriction to the flow, hence a higher pressure immediately downstream of the orifice. This higher pressure would offer more resistance to the escape of electrons, which might be expected to delay the starvation mode hypothesized above. At the higher flow rates, where this flow restriction might be expected to be more effective, Fig. 4-18 does, indeed, show higher ratios of emission to flow rate. Some optimization of the enclosed keeper configuration should therefore also be considered in future tests.

Summary

A major portion of these tests were accomplished to establish firm baseline data for argon hollow cathodes operated at emission currents up to 20 A. The components used were based on those components which have proved to be reliable and long lived when operated using mercury vapor as a propellant.

Well defined current limitations were observed for flow rates from 100 mA equiv. to 700 mA equiv. It is expected that current limitations also exist for flow rates above 700 mA but were beyond the 20 A limitation of the anode power supply used.

Anode currents up to 20 A were easily obtained with flow rates of 700 mA or more, and required anode voltages of 20 to 25 V. Curves of anode voltage versus anode current exhibited areas of negative slope,

probably as the result of a population instability related to some effect of high emission on the internal discharge.

At 20 A, tip temperatures ranged from 1325°C to 1525°C. It is hoped that variations in component dimensions will result in cooler and more efficient operation. Simple heat sinks or cooling fins would, of course, significantly reduce these temperatures.

The enclosed keeper tested proved to have an advantage at higher currents, in terms of maximum emission for a given propellant flow.

V. LARGE INERT-GAS THRUSTERS

Future electric propulsion missions include very large thrusters. This is particularly true for geocentric missions where inert-gas propellants are of interest for reduced environmental impact. Using assumptions consistent with current knowledge of thruster technology, performance predictions are made herein for very large thrusters. Detailed design considerations will almost certainly modify these predictions. But the general trends indicated should still be valuable in both directing future technology efforts and evaluating mission studies involving such large thrusters.

Calculation Procedure

Optimum discharge-chamber performance is normally obtained near the "knee" of the discharge-chamber performance curve. This is because operation at higher discharge losses will substantially increase the power loss for a much smaller increase in utilization. Conversely, operation at lower utilizations will decrease utilization more than the power loss will be decreased. The exact point near the knee that will prove optimum for a given operating condition will depend on that exact operating condition. For the purposes of this calculation, however, a single knee point will be used to simplify the iteration procedure. The error associated with this assumption should be less than the uncertainty in the discharge-chamber performance, when the latter is projected from a limited number of tests. For ease of calculation and rapid hardware development, the multipole type of discharge chamber was assumed.

Using previously obtained correlations obtained with argon and xenon,[1] together with the screen open-area fraction of 0.65 for the ion optics assumed, the knee discharge losses (eV/ion) used herein are

$$\Sigma = 73.\ (A_p/A_b) \qquad \text{(Ar)} \qquad (5\text{-}1a)$$

$$= 67.\ (A_p/A_b)\ . \qquad \text{(Xe)} \qquad (5\text{-}1b)$$

where A_b is the cross sectional area of the beam at the ion optics and A_p is the outside area of the primary electron region, (both in m^2). The corresponding neutral losses (A-equiv.) are

$$J_o(1-\eta_u) = 3.4\ A_o/(\Omega_p/A_p) \qquad \text{(Ar)} \qquad (5\text{-}2a)$$

$$= 0.41\ A_o/(\Omega_p/A_p)\ , \qquad \text{(Xe)} \qquad (5\text{-}2b)$$

where A_o is the effective open area of the ion optics (m^2), while Ω_p is the volume of the primary electron region (m^3). The effective open area, both herein and in ion optics designs with accel holes significantly smaller than the screen holes, is the accelerator open area times the Clausing factor[2] for the length-to-diameter ratio of the accelerator holes used. A simple cylindrical design was assumed for the discharge chamber, so that the primary electron region was assumed to be the cylinder that would just fit within the anodes, pole pieces, and screen grid. The form of equation used for Eqs. (5-2) is not evident from the correlation reference,[1] but can be derived from a more general expression given elsewhere.[3] A simpler expression was sufficient for the correlation because only a single chamber diameter and optics design were used.

A convenient starting point for the ion optics design is the screen hole diameter. In general, the smaller the screen holes, the larger the current capacity of the ion optics. A number of experimental studies have shown, though, that screen holes smaller than about 2 mm in diameter depart substantially from expected space-charge-flow performance.[4-6] A diameter of 1.9 mm is commonly used and is assumed to be the minimum diameter herein.

The choice of accelerator hole size is a compromise between the current carrying capacity and neutral loss, both of which increase as hole diameter is increased. To the first approximation, these variations are not dependent on the use of a two or three grid ion optics design, or the value of net-to-total voltage ratio, R, used. The beam current capacity is proportional to the normalized perveance, while the neutral loss is proportional to the effective open area of the accelerator grid. A performance index can therefore be obtained by dividing the normalized perveance by the effective open area of a single aperture. The effective open area also includes a Clausing factor, so a typical ratio of accel thickness to screen hole diameter of 0.2 is assumed. Expressing the accel hole area as a fraction of screen hole area, the performance index is $N.P./(d_a/d_s)^2 K_c$. Using two-grid experimental data for an R of 0.7,[7] a plot of this index against accel-to-screen hole diameter ratio, d_a/d_s, is shown in the following sketch. The normalized perveance used was for mercury propellant, but the d_a/d_s value for the maximum would be the same for other propellants. The significant point about the data shown in the sketch is the maximum near the data point for $d_a/d_s = 0.64$. More detailed ion optics data would probably give a slightly different value. In addition, the exact d_a/d_s would shift

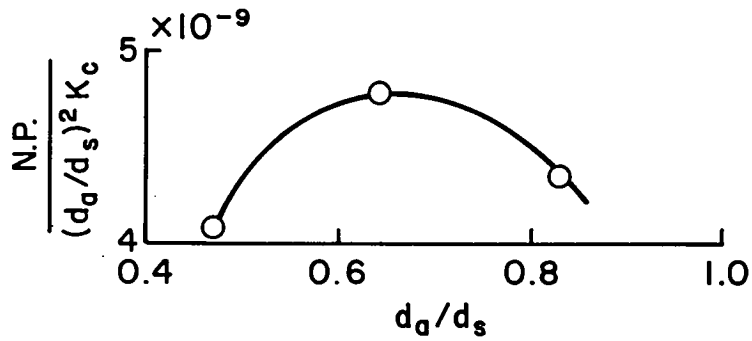

slightly for different operating conditions. For the purposes of this study, though, a value of $d_a/d_s = 0.64$ should be sufficiently precise.

For the maximum span-to-gap ratio, hence maximum thruster diameter, some form of ion optics using dished molybdenum grids will be assumed. As described in a preliminary study of large thrusters, a maximum span-to-gap ratio of about 600:1 can be assumed for this approach.[8] This maximum span-to-gap ratio is essentially determined by thermal/mechanical effects and will undoubtedly vary somewhat with size, power level, and the specific mechanical design used. As with other assumptions, however, the use of a single limit value is appropriate for this analysis.

Another ion optic parameter that must be selected is that of grid spacing relative to screen hole diameter, ℓ_g/d_s. We are not just interested in physically large thrusters, we also want them to have high performance. For high current and power densities it is necessary that the grid spacing be small. As shown in the following sketch, the benefits of small ℓ_g's are limited for $\ell_g/d_s \ll 1$. The best simple

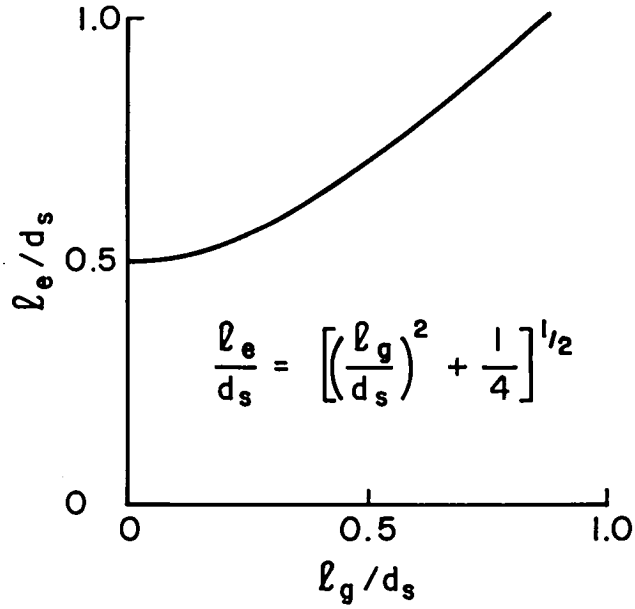

parameter for acceleration distance between a screen grid and an accelerator grid is the effective acceleration distance, ℓ_e, defined by the equation given in the sketch. The ratio ℓ_e/d_s decreases with decreasing ℓ_g/d_s, but the decrease becomes very small as ℓ_g/d_s approaches zero. A tradeoff is indicated because a small ℓ_e/d_s is desirable for high current density, but the tolerance and electrical breakdown problems become critical as ℓ_g/d_s approaches zero.

As a partially arbitrary assumption, a value of 0.5 was selected for ℓ_g/d_s. The argument given above for a small ℓ_g/d_s is most persuasive for low specific impulses, where the maximum electric fields are not a limit, even though the smallest permissible screen hole diameter is used. There is, though, a thermal expansion argument that is valid at all specific impulses. For the maximum span-to-gap ratio, thermal expansion would be a larger fraction of screen-hole diameter

if a larger value of ℓ_g/d_s were used. Specific designs (particularly high specific impulses at less than maximum span-to-gap ratio) may benefit from larger values of ℓ_g/d_s, but the value selected appears to be a reasonable choice for all designs.

For ion beam calculations, a normalized perveance of 3×10^{-9} (Ar)[7] appears to be a reasonable value. That is, high, but not so high as to risk serious accelerator impingement. For xenon, the normalized perveance was corrected by the square-root of atomic mass. Backstreaming calculations for the assumed geometry indicate a maximum R of 0.8,[9] while the minimum R was assumed for two grids to be 0.7 (for 15° half angle)[7] and for three grids to be 0.17 (same 15° half angle, $\ell_g = \ell_d$). For three grids, the decelerator grid should also have holes about 0.83 times the screen hole diameter.[7] The decelerator grid spacing was assumed equal to the accelerator grid spacing because, for the largest thrusters, both spacings should be subject to roughly the same limit in span-to-gap ratio.

For minimum screen hole diameter, then, the minimum gap is 0.5 × 1.9, or 0.95 mm. A safe limit on maximum electric field appears to be 2000 V/mm,[3,8] although further breakdown data with operating thrusters may show that this is too small for the smaller gaps. This 2000 V/mm limit was used for all calculations herein. For the smallest grid gap then, a total voltage of 1900 V (0.95 mm × 2000 V/mm) is permissible. The gap was increased above the 0.95 mm value if required to maintain (1) the permissible span-to-gap ratio of 600:1 or (2) to reduce the screen-accel electric field to 2000 V/mm.

For the preliminary calculations shown herein, no off-axis thrust loss was included, no neutralizer propellant loss was included, and the only power loss was assumed due to the discharge.

To avoid an unnecessary iteration, a performance calculation at a given specific impulse was started by assuming a propellant utilization. The net voltage necessary to obtain the required average propellant velocity was then calculated, followed by the complete ion optics performance, consistent with span-to-gap and electric field limits. Next, the discharge chamber length (or depth) required for the assumed utilization was calculated. (The neutral loss is actually the parameter of interest for this length, and is available from the assumed utilization and the calculated beam current. It should be noted that it is possible to initially assume a propellant utilization that is too high to be obtained by any discharge chamber length.) With the chamber length known, the discharge loss and thruster efficiency was calculated.

Double ion production was considered in this analysis, although not in detail. From the information presented earlier in this report, it was assumed that low discharge voltages would reduce double ion production to a level consistent with both long life and high performance. The present understanding of electron diffusion is also assumed to be sufficient to permit reaching the necessary low discharge voltages.

Calculated Performance

Calculated performance data are shown for argon propellant in Figs. 5-1 through 5-7 and for xenon propellant in Figs. 5-8 through 5-14. These data are also shown in Tables 5-1 through 5-14. For convenient reference, the figure and table numbers are the same for each set of data.

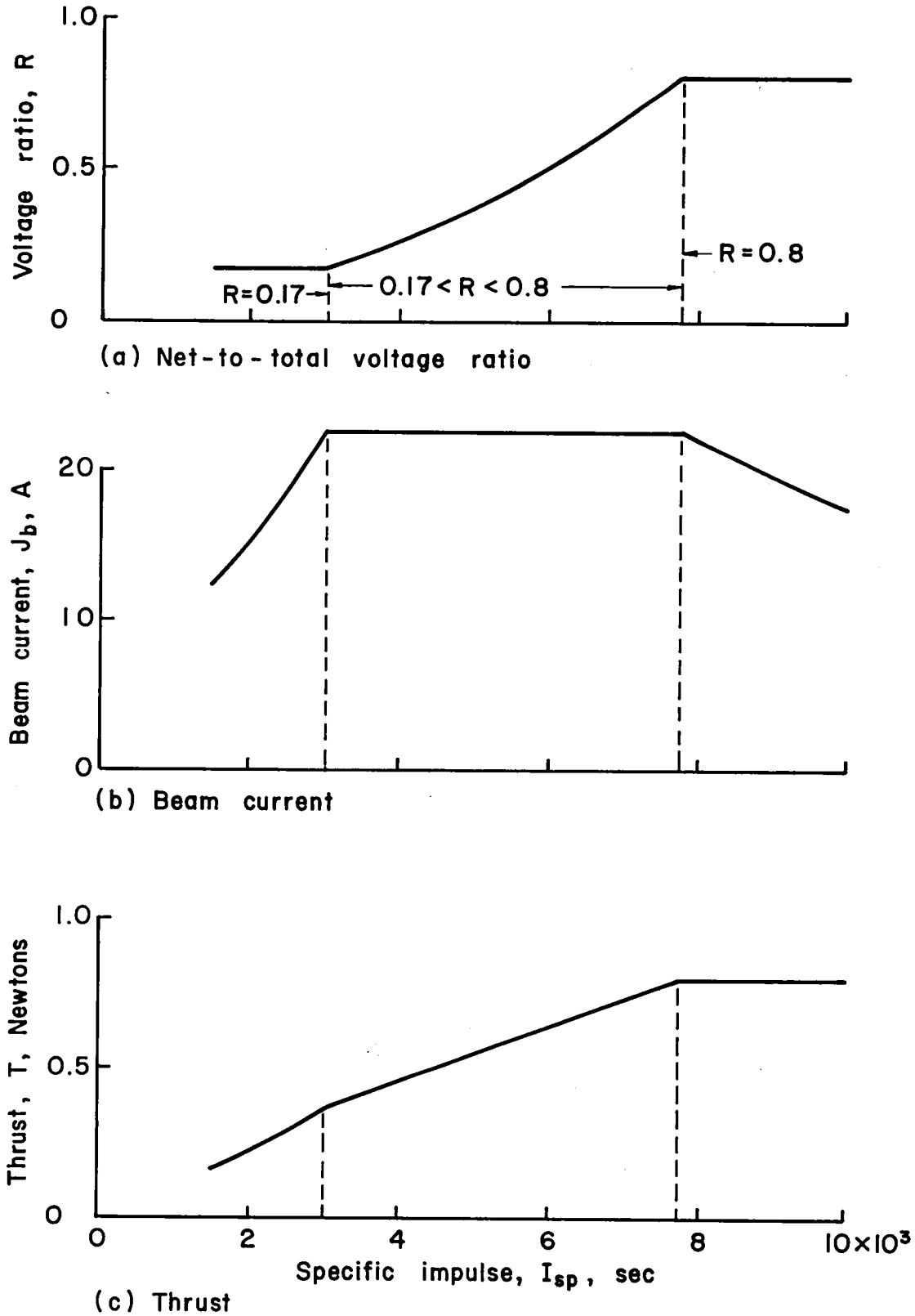

Fig. 5-1. Effect of specific impulse on performance. Propellant, argon; beam diameter, 0.5 m; propellant utilization, optimized for maximum thruster efficiency.

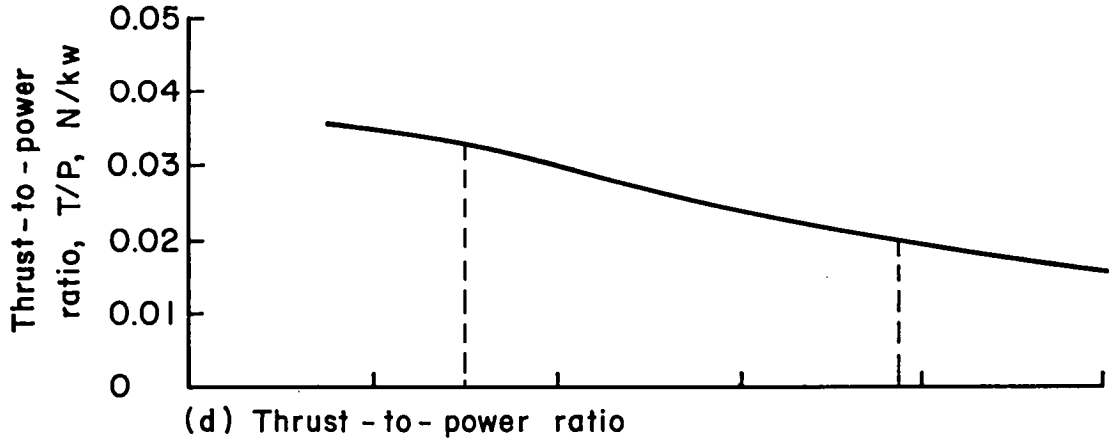

(d) Thrust-to-power ratio

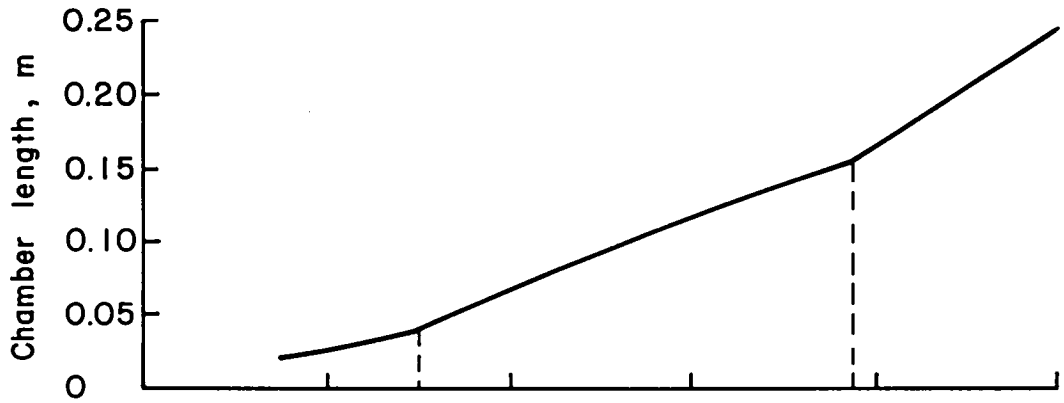

(e) Discharge chamber length

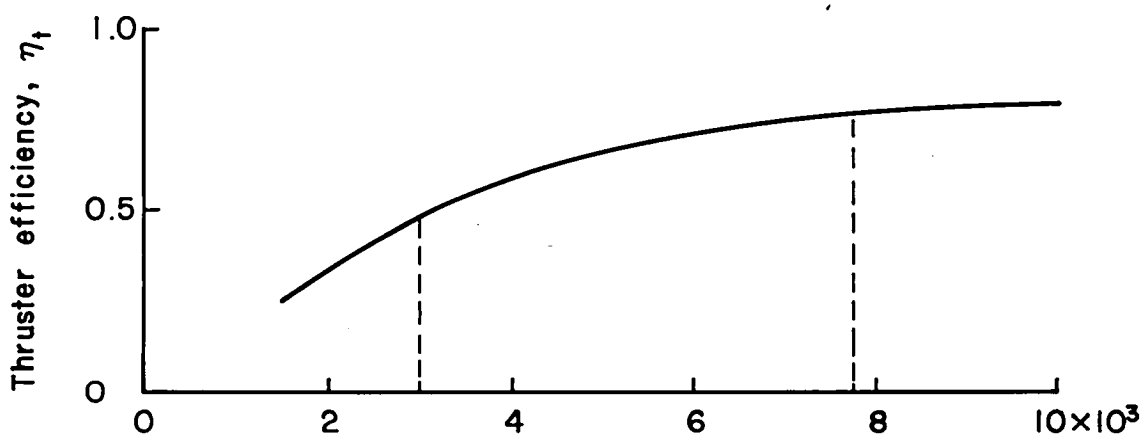

(f) Thruster efficiency

Fig. 5-1. Concluded

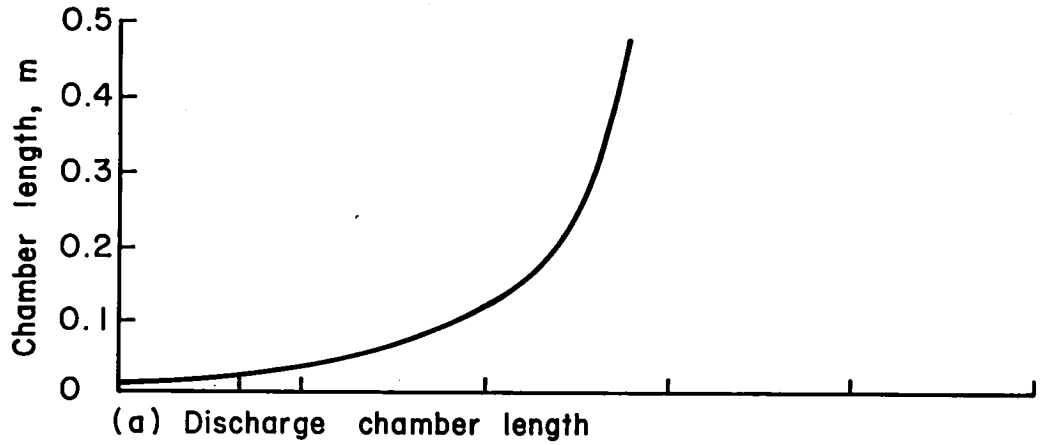

(a) Discharge chamber length

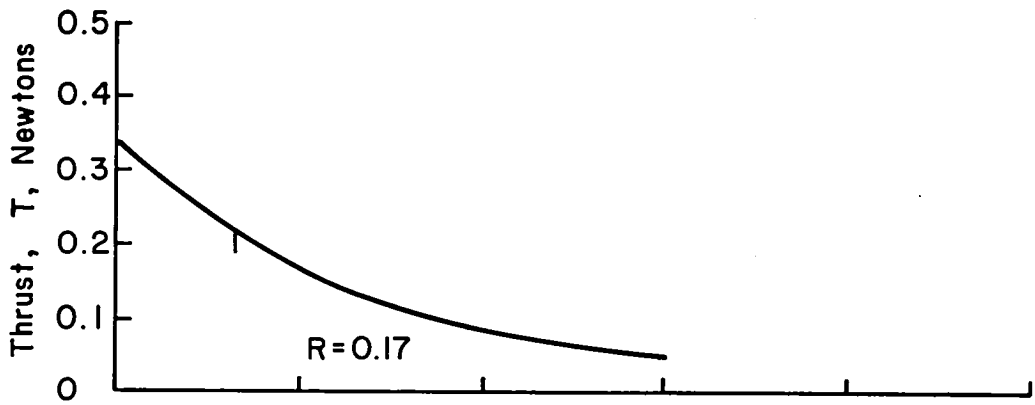

(b) Thrust

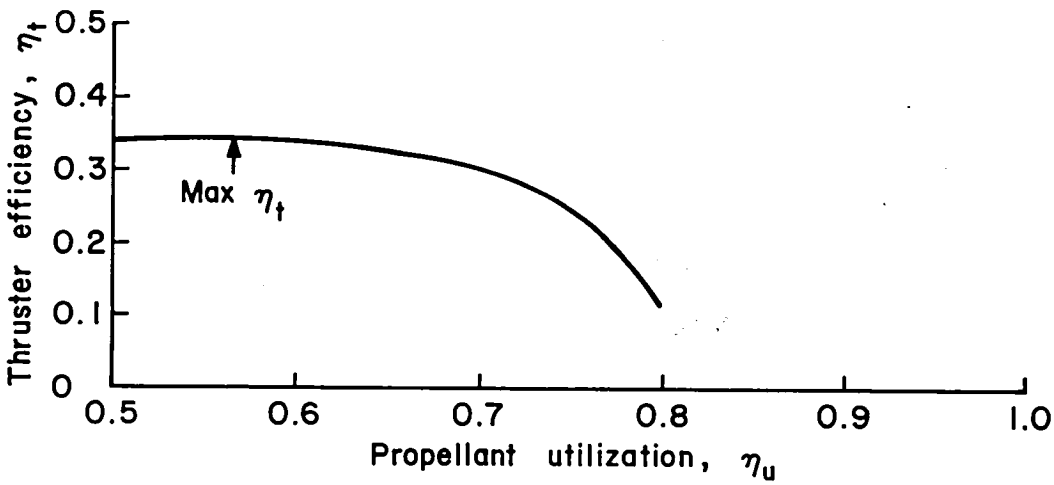

(c) Thruster efficiency

Fig. 5-2. Effect of propellant utilization on performance. Propellant, argon; beam diameter, 0.5 m; specific impulse, 2000 sec.

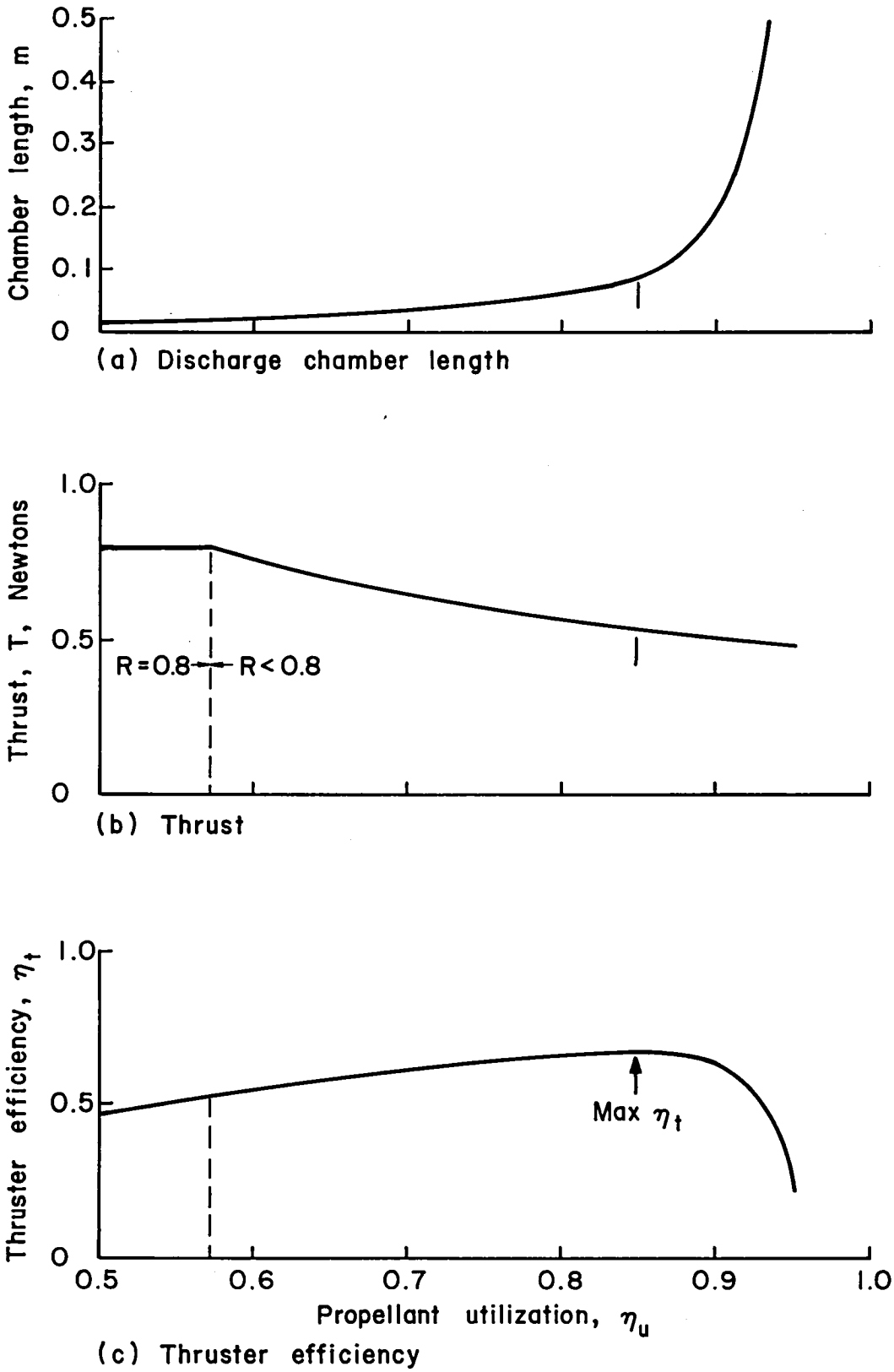

Fig. 5-3. Effect of propellant utilization on performance. Propellant, argon; beam diameter, 0.5 m; specific impulse, 5000 sec.

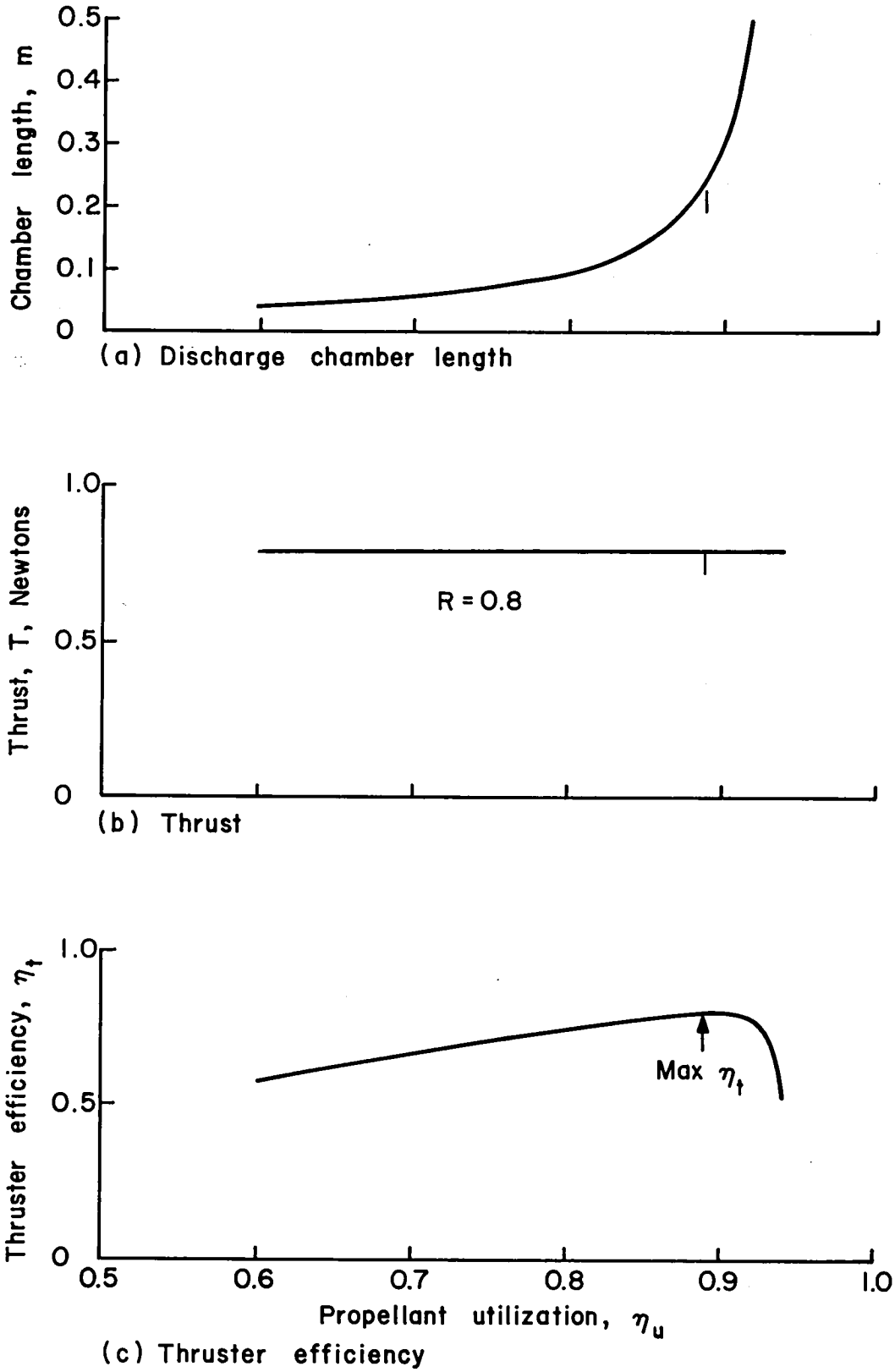

Fig. 5-4. Effect of propellant utilization on performance. Propellant, argon; beam diameter, 0.5 m; specific impulse, 10,000 sec.

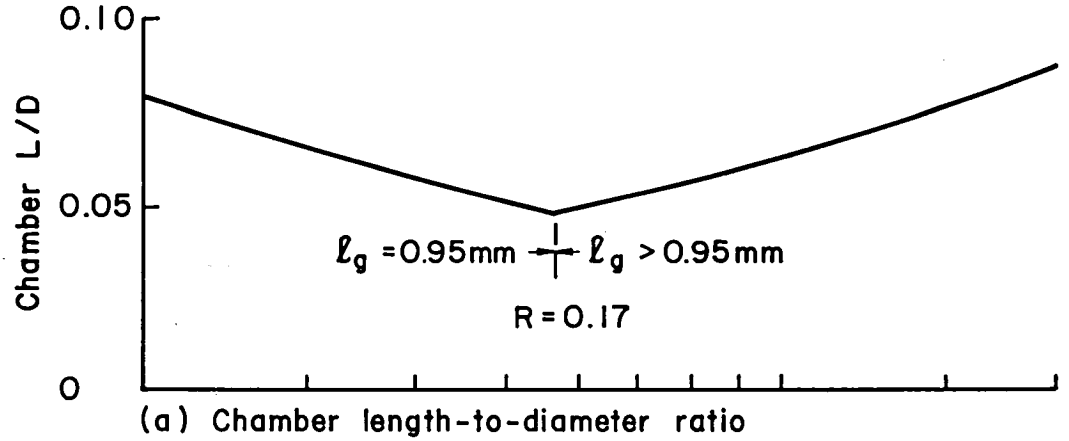

(a) Chamber length-to-diameter ratio

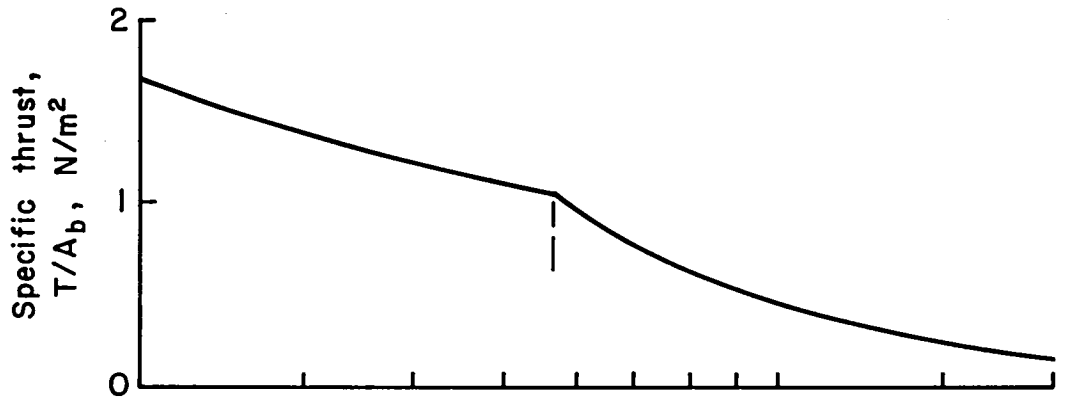

(b) Thrust-to-beam area ratio

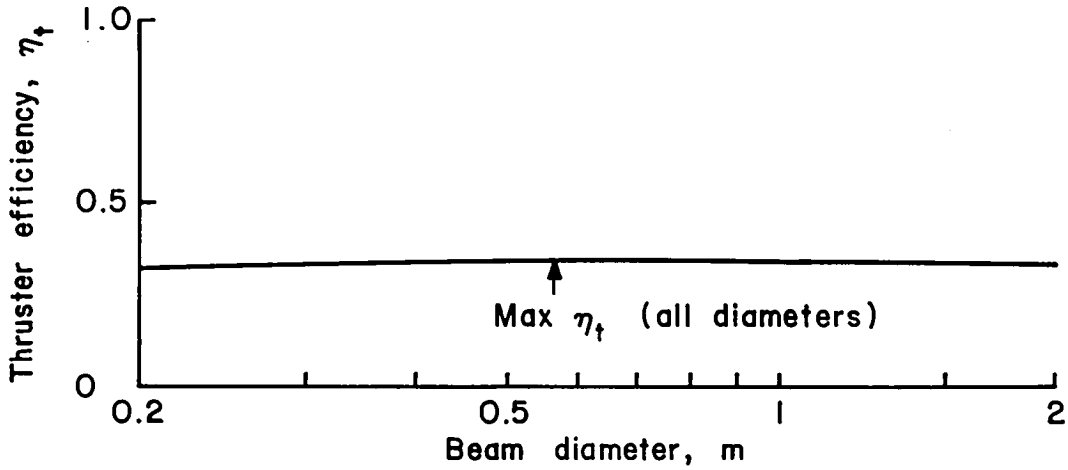

(c) Thruster efficiency

Fig. 5-5. Effect of beam diameter on performance. Propellant, argon; specific impulse, 2,000 sec; propellant utilization, optimized for maximum thruster efficiency.

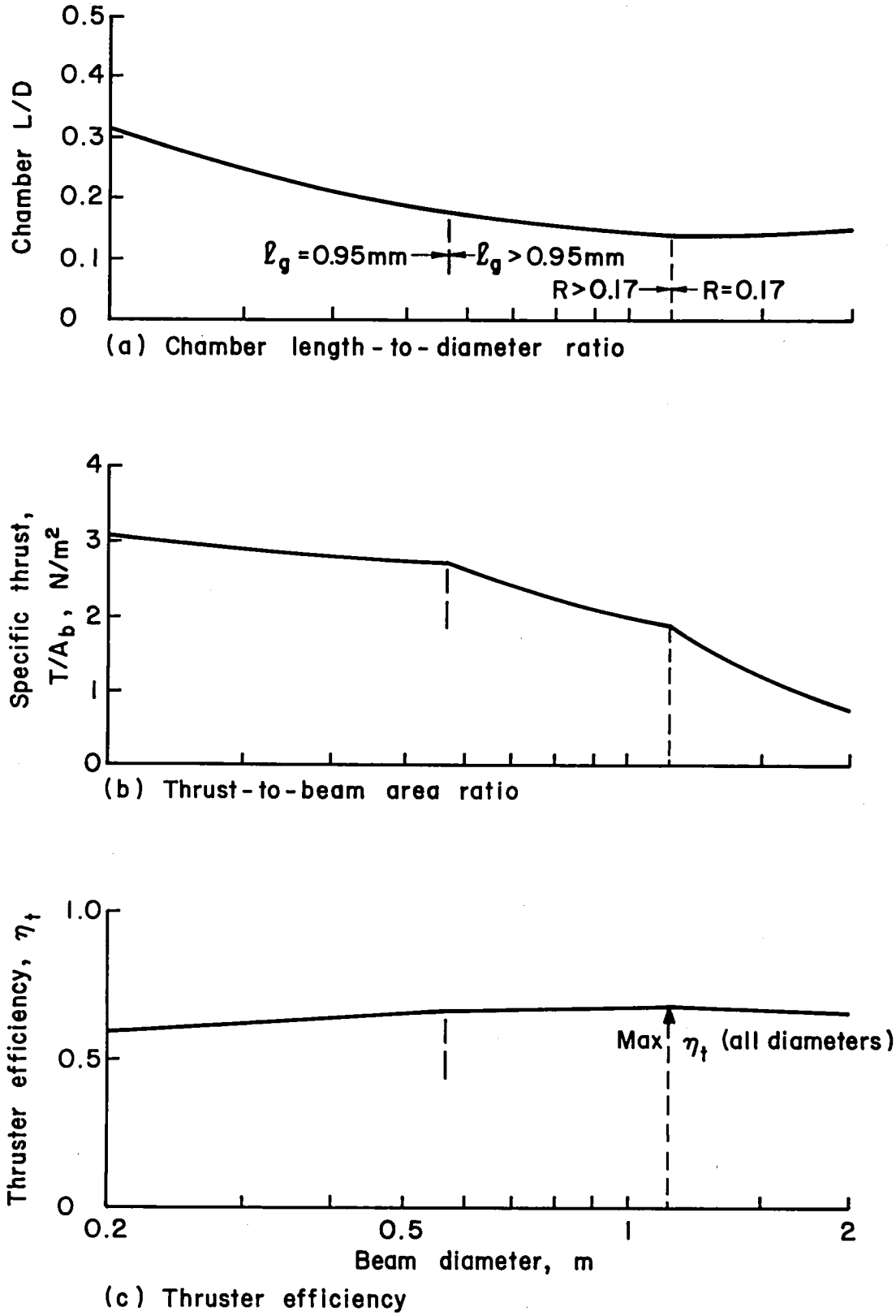

Fig. 5-6. Effect of beam diameter on performance. Propellant, argon; specific impulse, 5,000 sec; propellant utilization, optimized for maximum thruster efficiency.

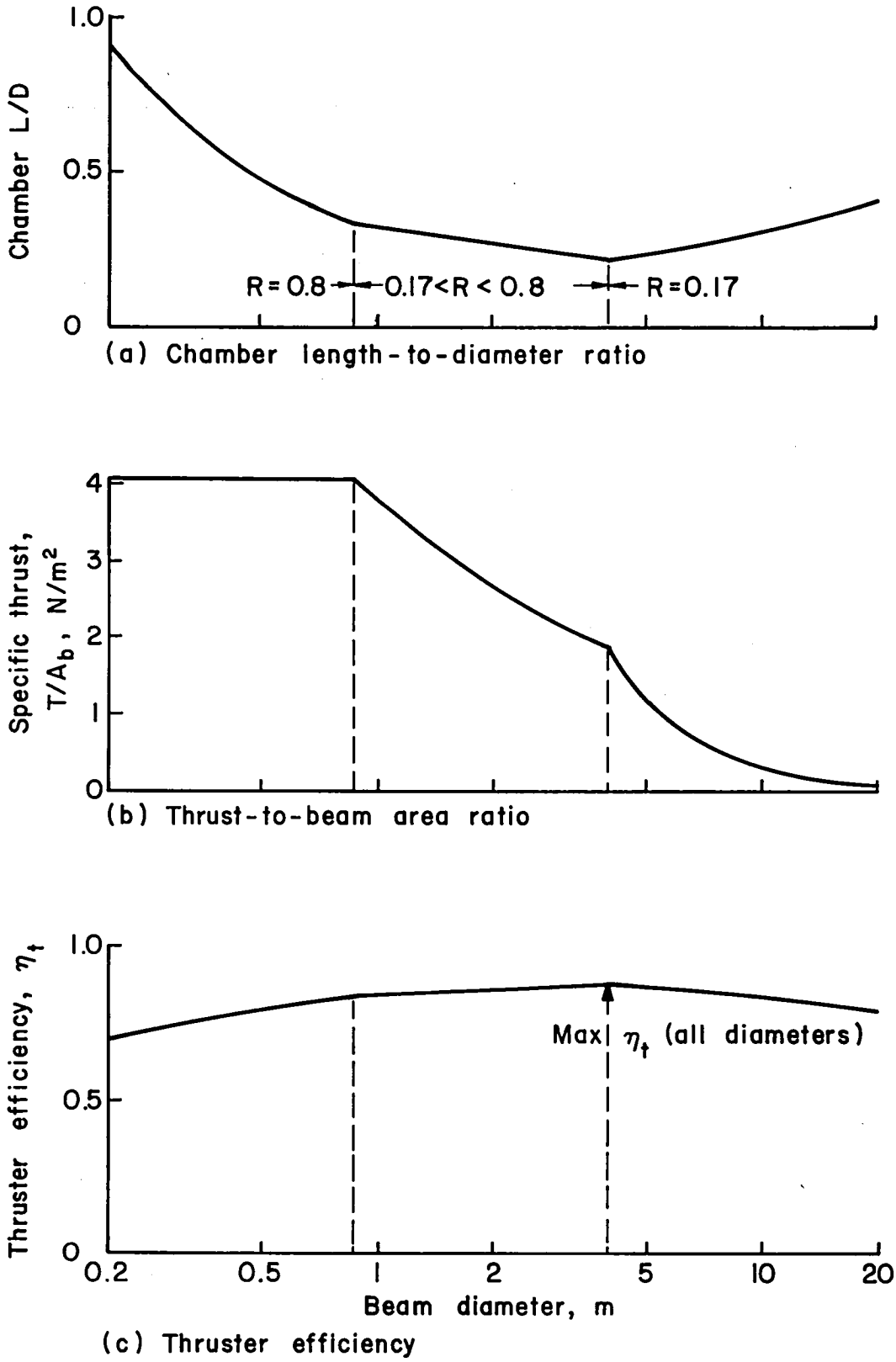

Fig. 5-7. Effect of beam diameter on performance. Propellant, argon; specific impulse, 10,000 sec; propellant utilization, optimized for maximum thruster efficiency.

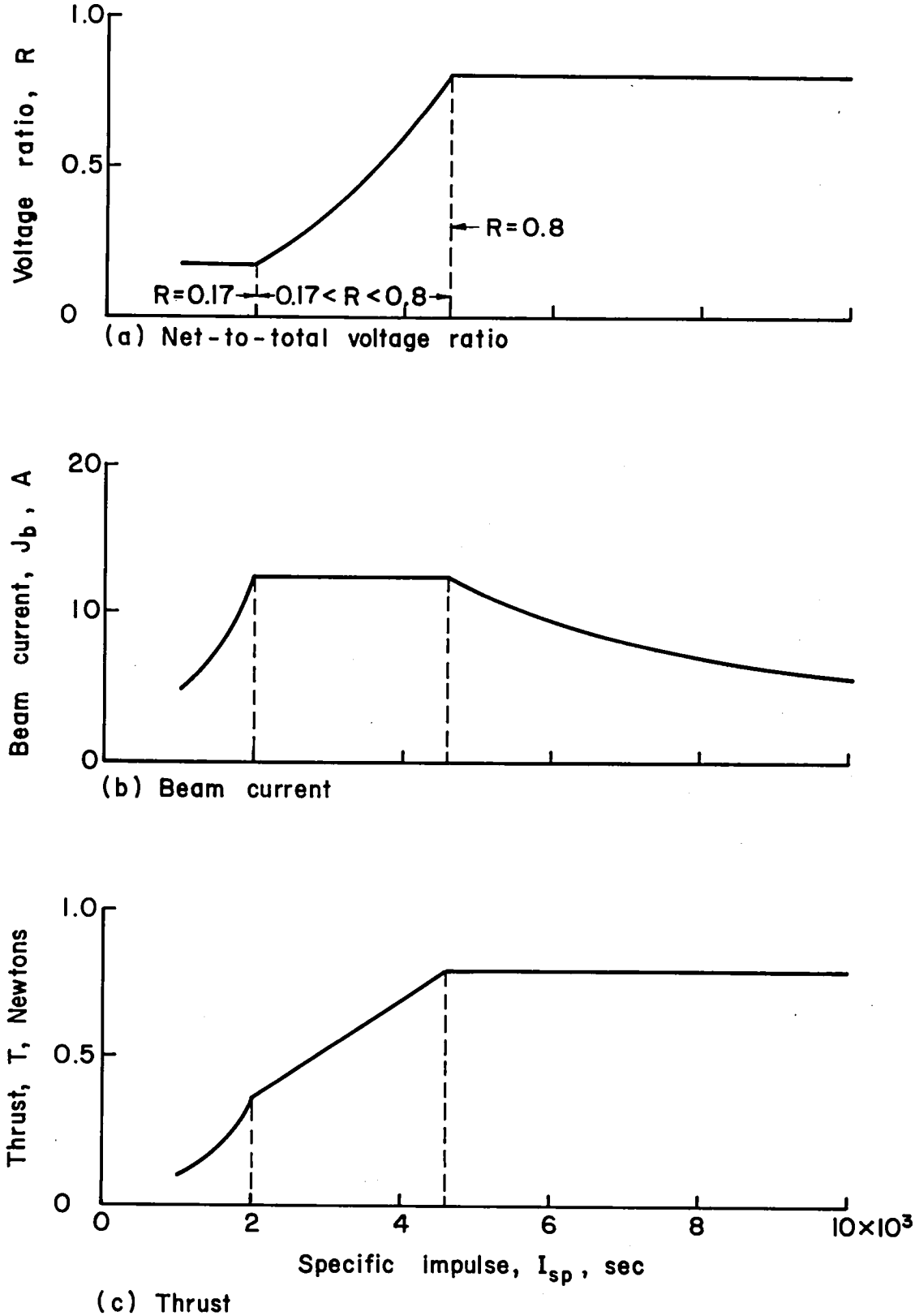

Fig. 5-8. Effect of specific impulse on performance. Propellant, xenon; beam diameter, 0.5 m; propellant utilization, optimized for maximum thruster efficiency.

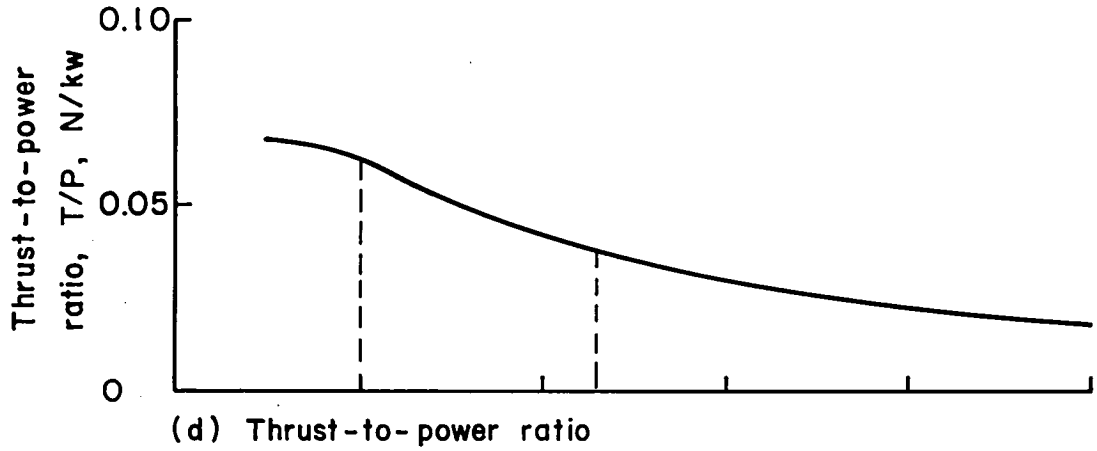

(d) Thrust-to-power ratio

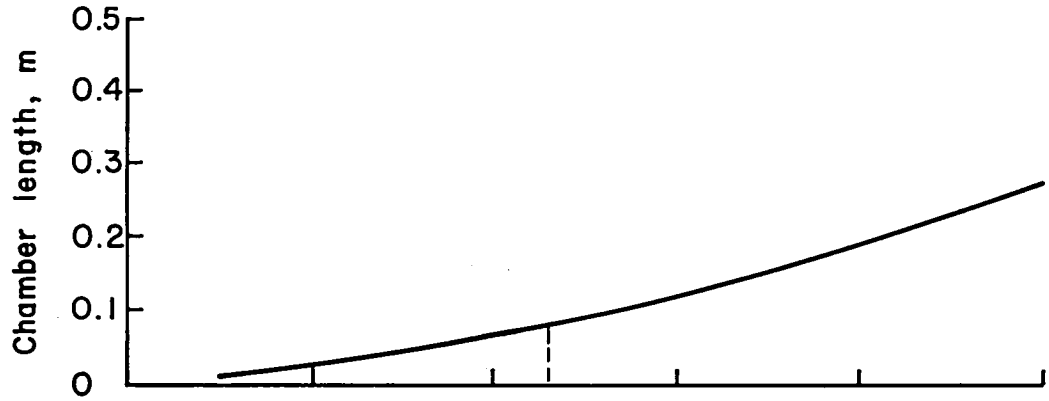

(e) Discharge chamber length

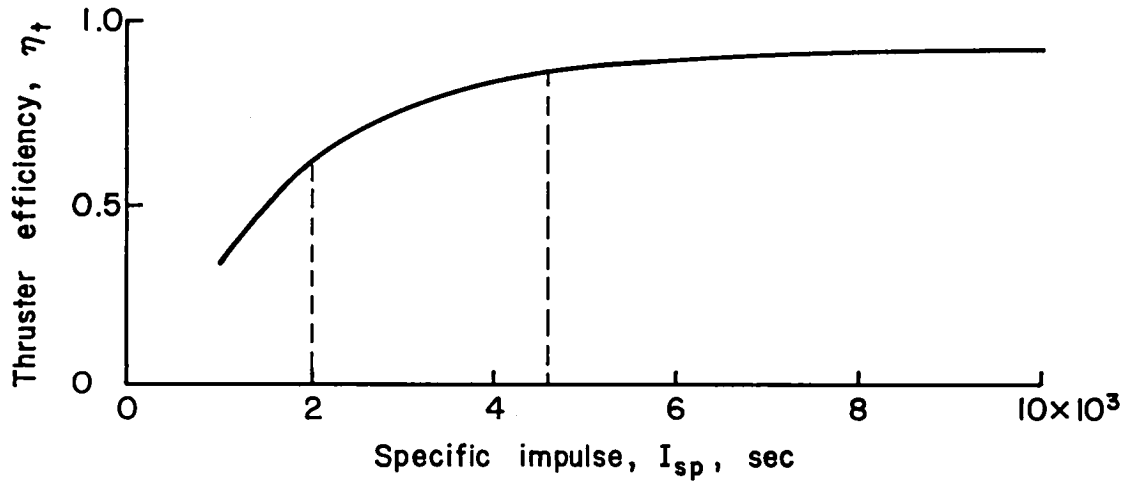

(f) Thruster efficiency

Fig. 5-8. Concluded

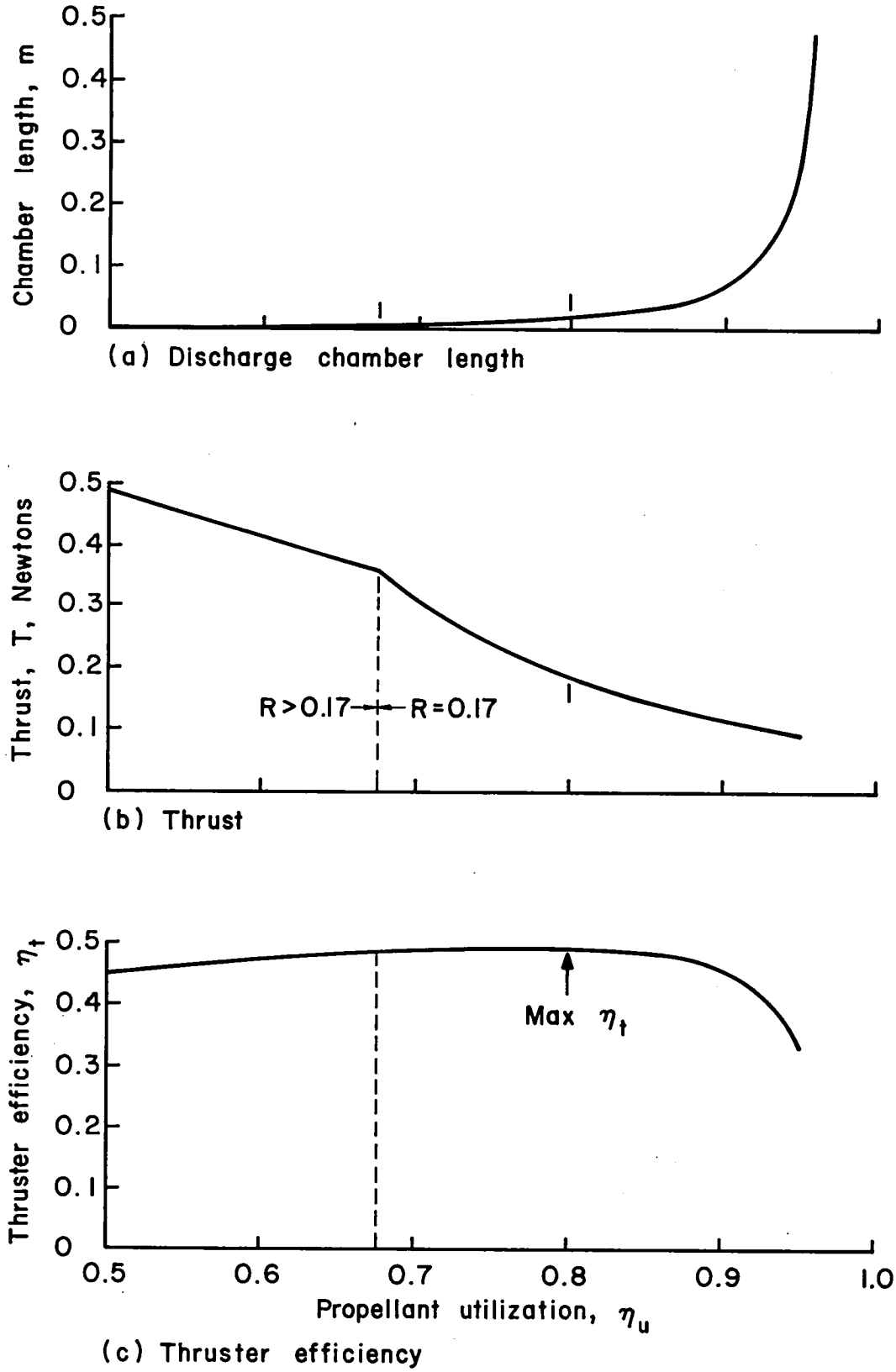

Fig. 5-9. Effect of propellant utilization on performance. Propellant, xenon; beam diameter, 0.5 m; specific impulse, 1,500 sec.

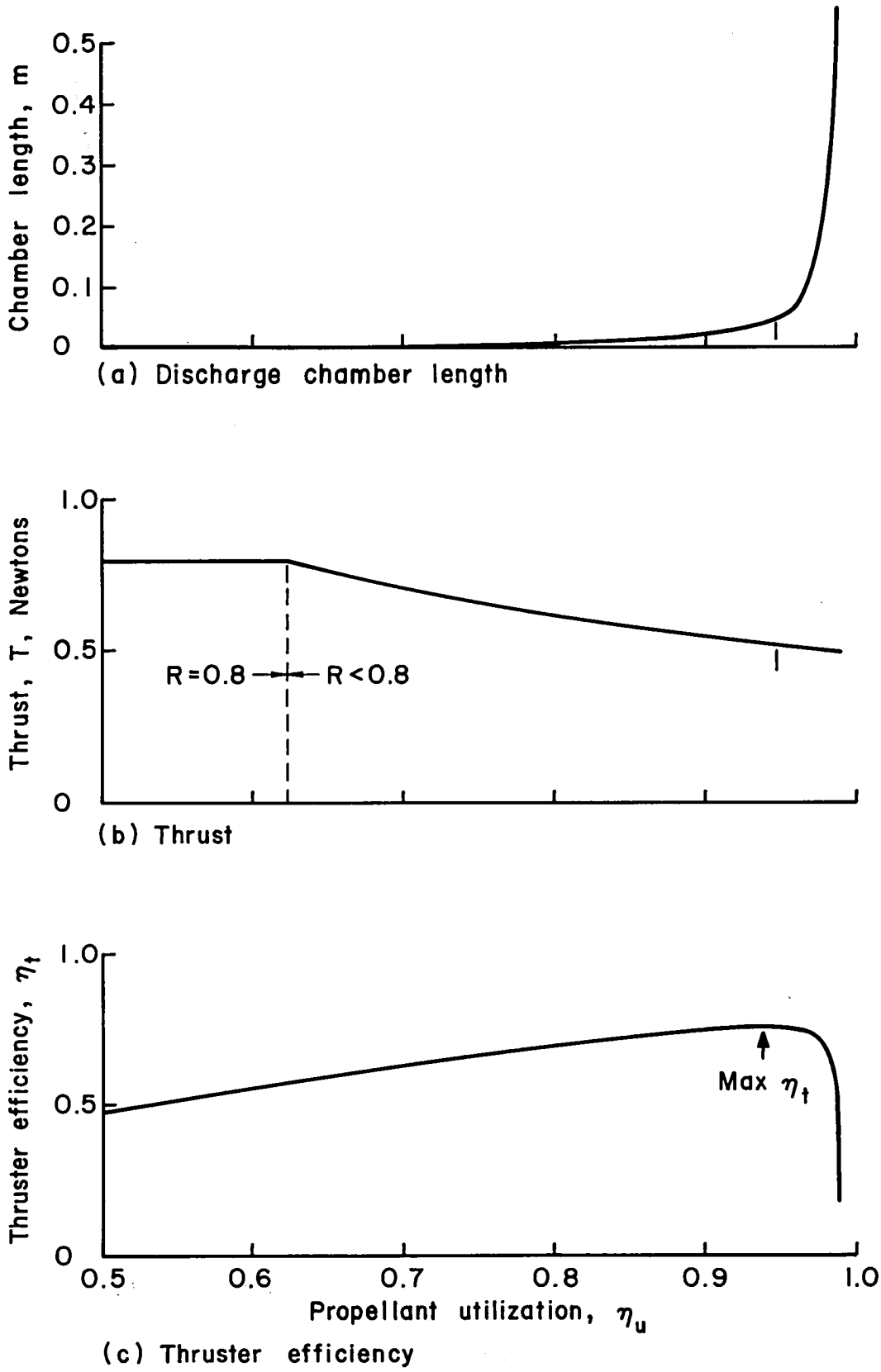

Fig. 5-10. Effect of propellant utilization on performance. Propellant, xenon; beam diameter, 0.5 m; specific impulse, 3,000 sec.

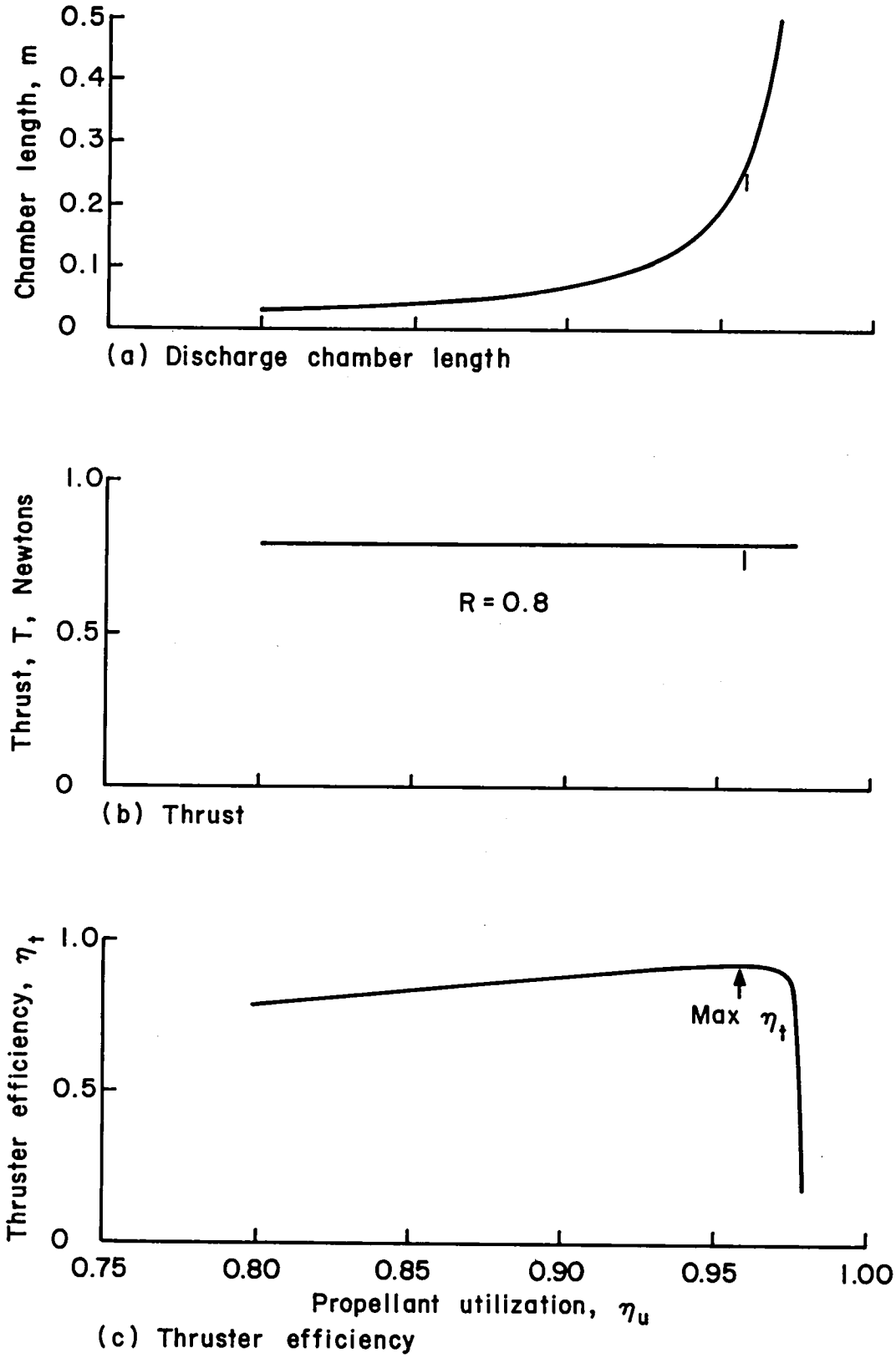

Fig. 5-11. Effect of propellant utilization on performance. Propellant, xenon; beam diameter, 0.5 m; specific impulse, 10,000 sec.

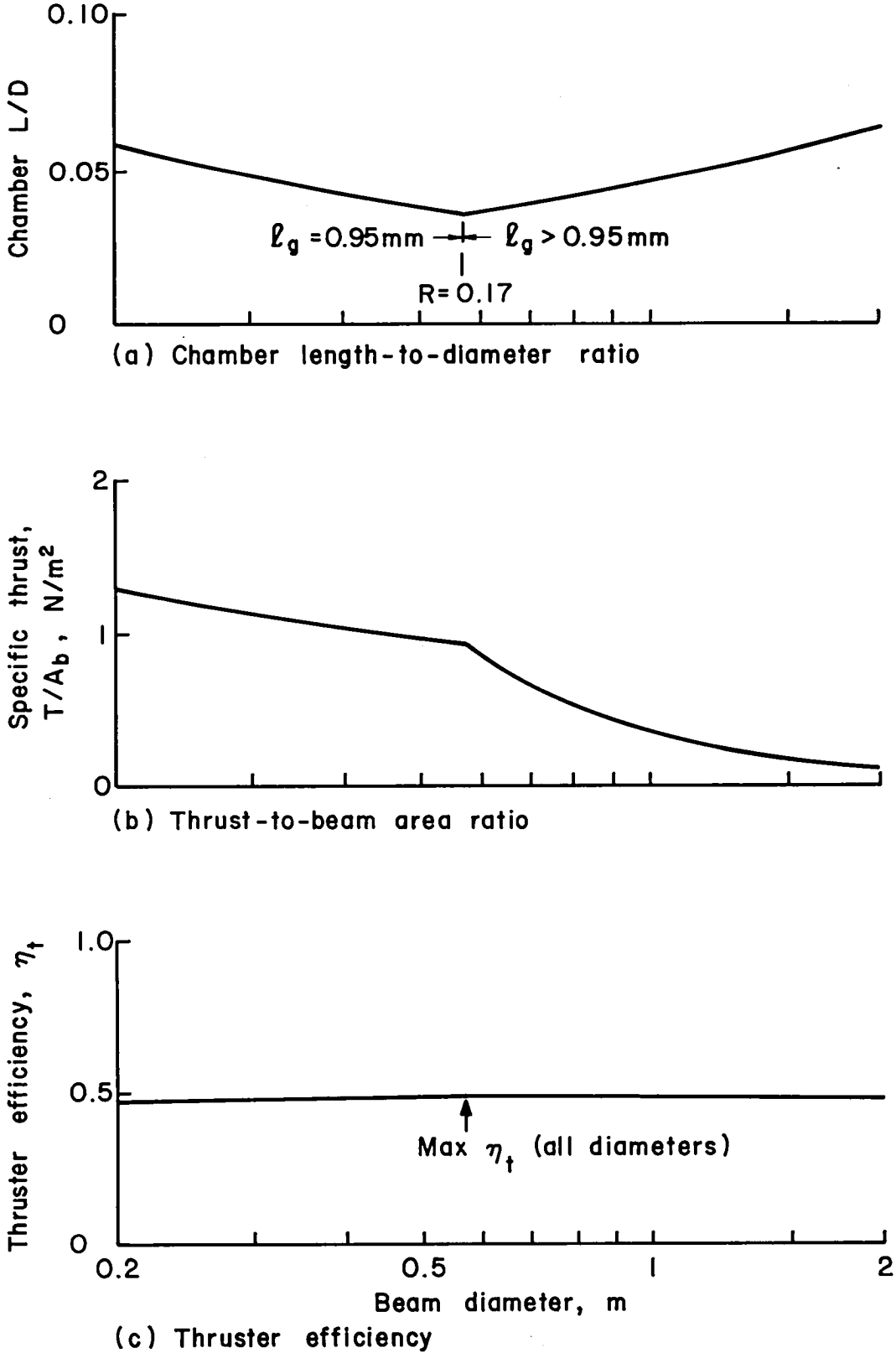

Fig. 5-12. Effect of beam diameter on performance. Propellant, xenon; specific impulse, 1,500 sec; propellant utilization, optimized for maximum thruster efficiency.

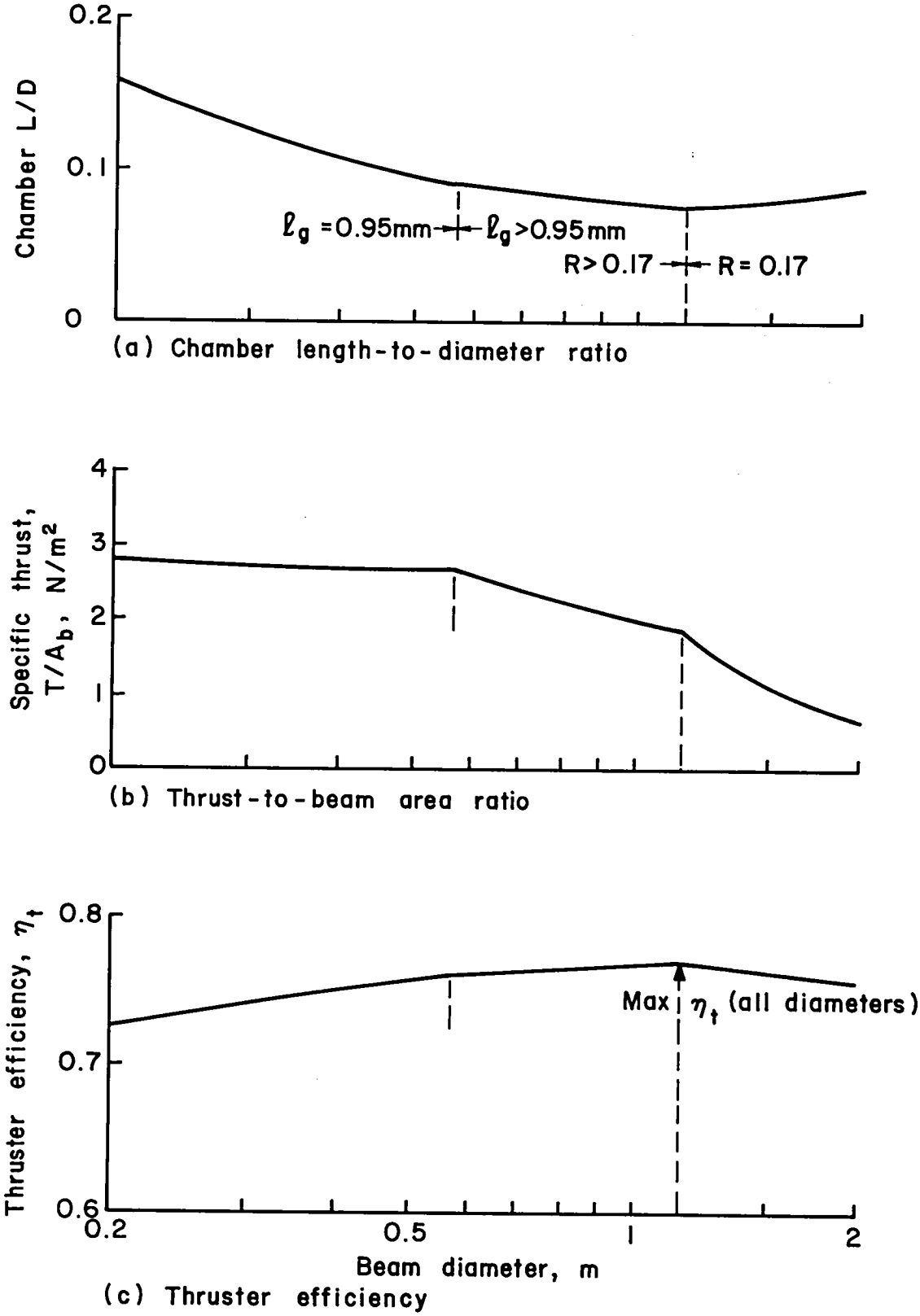

Fig. 5-13. Effect of beam diameter on performance. Propellant, xenon; specific impulse, 3,000 sec; propellant utilization, optimized for maximum thruster efficiency.

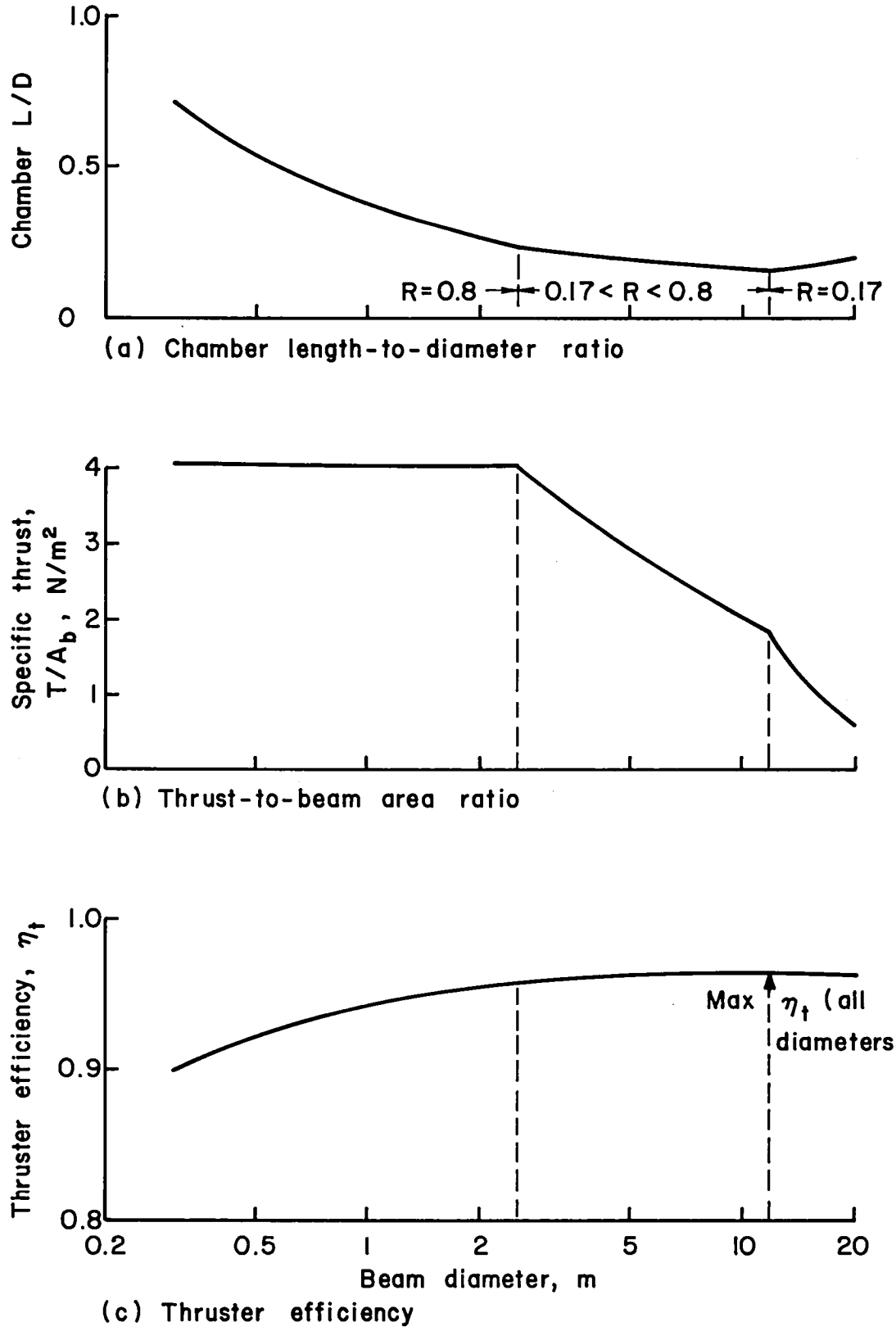

Fig. 5-14. Effect of beam diameter on performance. Propellant, xenon; specific impulse, 10,000 sec; propellant utilization, optimized for maximum thruster efficiency.

Beam Diameter, m	Specific Impulse, sec	Propellant Utilization, η_u	Thruster Efficiency, η_t	Power, KW	Thrust, N	Beam Current, A	Net Voltage, ΔV_n, V	Total Voltage, ΔV_t, V	Voltage Ratio, R	Grid Gap ℓ_g, mm	Chamber Length, m	Discharge Loss, eV/ion
Table 5-1. Argon Propellant, 0.5 m Beam Diameter, Optimum Propellant Utilization.												
	1500.	0.454	0.263	4.64	0.166	12.4	217.	1279.	0.1700	0.950	0.020	157.
	2000.	0.566	0.344	6.21	0.217	15.2	249.	1462.	0.1700	0.950	0.026	161.
	2500.	0.659	0.419	8.46	0.289	18.8	289.	1686.	0.1700	0.950	0.031	164.
	3000.	0.745	0.488	11.1	0.367	22.4	323.	1899.	0.1700	0.950	0.041	170.
	4000.	0.819	0.588	14.8	0.445	22.4	475.	1900.	0.2500	0.950	0.070	187.
	5000.	0.849	0.658	20.0	0.537	22.4	691.	1900.	0.3635	0.950	0.093	200.
	6000.	0.867	0.709	26.2	0.631	22.4	954.	1900.	0.5019	0.950	0.114	213.
	7000.	0.880	0.746	33.3	0.725	22.4	1260.	1900.	0.6631	0.950	0.137	226.
	7770.	0.889	0.769	39.5	0.796	22.4	1521.	1901.	0.8000	0.951	0.157	238.
	8000.	0.891	0.773	40.4	0.796	21.8	1605.	2007.	0.8000	1.003	0.170	245.
	9000.	0.890	0.787	44.6	0.796	19.4	2036.	2545.	0.8000	1.273	0.205	266.
	10000.	0.888	0.797	49.0	0.796	17.4	2525.	3156.	0.8000	1.578	0.242	288.
Table 5-2. Argon Propellant, 0.5 m Beam Diameter, 2000 sec.												
		0.40	0.307	14.6	0.465	22.4	498.	1900.	0.2620	0.950	0.008	151.
		0.50	0.337	10.4	0.357	22.0	319.	1874.	0.1700	0.950	0.013	154.
		0.566	0.344	6.21	0.217	15.2	249.	1462.	0.1700	0.950	0.026	161.
		0.60	0.342	4.94	0.172	12.7	221.	1301.	0.1700	0.950	0.036	167.
		0.70	0.303	3.01	0.0930	8.01	163.	956.	0.1700	0.950	0.115	213.
		0.75	0.246	2.82	0.0705	6.51	142.	833.	0.1700	0.950	0.248	291.
		0.77	0.207	3.01	0.0635	6.02	134.	790.	0.1700	0.950	0.377	366.
		0.80	0.114	4.70	0.0545	5.37	124.	732.	0.1700	0.950	1.036	751.
Table 5-3. Argon Propellant, 0.5 m Beam Diameter, 5000 sec.												
		0.50	0.464	42.1	0.796	19.6	1991.	2489.	0.8000	1.245	0.015	155.
		0.572	0.519	37.6	0.796	22.4	1521.	1902.	0.8000	0.951	0.017	156.
		0.60	0.539	34.6	0.759	22.4	1383.	1900.	0.7278	0.950	0.019	157.
		0.70	0.602	26.5	0.651	22.4	1016.	1900.	0.5347	0.950	0.032	164.
		0.80	0.649	21.5	0.570	22.4	778.	1900.	0.4094	0.950	0.060	181.
		0.849	0.658	20.0	0.537	22.4	691.	1900.	0.3635	0.950	0.093	200.
		0.90	0.634	19.6	0.506	22.4	615.	1900.	0.3235	0.950	0.191	258.
		0.93	0.546	22.0	0.490	22.4	576.	1900.	0.3029	0.950	0.444	405.
		0.95	0.231	51.0	0.480	22.4	552.	1900.	0.2903	0.950	2.697	1721.
Table 5-4. Argon Propellant, 0.5 m Beam Diameter, 10,000 sec.												
		0.60	0.582	67.1	0.796	11.8	5531.	6914.	0.8000	3.457	0.040	169.
		0.70	0.670	58.2	0.796	13.7	4064.	5080.	0.8000	2.540	0.056	179.
		0.80	0.751	52.0	0.796	15.7	3111.	3889.	0.8000	1.945	0.095	202.
		0.86	0.789	49.5	0.796	16.9	2692.	3365.	0.8000	1.683	0.162	241.
		0.88	0.796	49.0	0.796	17.3	2571.	3214.	0.8000	1.607	0.212	270.
		0.888	0.797	49.0	0.796	17.4	2525.	2007.	0.8000	1.578	0.242	288.
		0.90	0.795	49.1	0.796	17.6	2458.	3073.	0.8000	1.536	0.307	325.
		0.92	0.767	50.9	0.796	18.0	2353.	2941.	0.8000	1.470	0.554	470.
		0.93	0.716	54.5	0.796	18.2	2302.	2878.	0.8000	1.439	0.927	687.
		0.94	0.523	74.7	0.796	18.4	2254.	2817.	0.8000	1.408	0.283	1799.
Table 5-5. Argon Propellant, Optimum Propellant Utilization, 2000 sec.												
0.20		0.511	0.329	1.56	0.0524	3.30	305.	1794.	0.1700	0.950	0.016	169.
0.30		0.536	0.336	2.84	0.0973	6.42	277.	1631.	0.1700	0.950	0.020	165.
0.40		0.553	0.340	4.40	0.153	10.4	260.	1532.	0.1700	0.950	0.023	162.
0.50		0.566	0.344	6.21	0.217	15.2	249.	1462.	0.1700	0.950	0.026	161.
0.57		0.574	0.345	7.59	0.267	18.9	242.	1422.	0.1700	0.950	0.027	160.
0.60		0.574	0.345	7.60	0.267	18.9	242.	1422.	0.1700	1.000	0.031	161.
0.70		0.562	0.343	8.33	0.291	20.1	252.	1483.	0.1700	1.167	0.037	162.
0.80		0.554	0.341	8.87	0.308	21.0	260.	1527.	0.1700	1.333	0.046	163.
1.00		0.541	0.337	9.85	0.339	22.6	272.	1601.	0.1700	1.667	0.064	165.
2.00		0.498	0.325	14.2	0.472	28.9	321.	1889.	0.1700	3.333	0.174	171.

Beam Diameter, m	Specific Impulse, sec	Propellant Utilization, η_u	Thruster Efficiency, η_t	Power, KW	Thrust, N	Beam Current, A	Net Voltage, ΔV_n, V	Total Voltage, ΔV_t, V	Voltage Ratio, R	Grid Gap ℓ_g, mm	Chamber Length, m	Discharge Loss, eV/ion
Table 5-6. Argon Propellant, Optimum Propellant Utilization, 5000 sec.												
0.20		0.762	0.597	3.93	0.096	3.59	857.	1900.	0.4512	0.950	0.063	238.
0.30		0.805	0.627	7.96	0.204	8.08	766.	1900.	0.4033	0.950	0.075	219.
0.40		0.831	0.645	13.3	0.351	14.4	721.	1900.	0.3794	0.950	0.084	207.
0.50		0.849	0.658	20.0	0.537	22.4	691.	1900.	0.3635	0.950	0.093	200.
0.57		0.859	0.665	25.4	0.689	29.2	675.	1900.	0.3551	0.950	0.099	197.
0.70		0.866	0.670	34.0	0.931	39.7	664.	2333.	0.2845	1.167	0.114	194.
0.80		0.870	0.674	41.2	1.132	48.5	658.	2667.	0.2466	1.333	0.125	192.
1.00		0.877	0.679	56.7	1.569	67.8	647.	3333.	0.1942	1.667	0.147	189.
1.139		0.878	0.682	68.5	1.905	82.4	646.	3797.	0.1701	1.898	0.156	186.
1.50		0.855	0.672	77.4	2.120	89.3	681.	4006.	0.1700	2.500	0.204	186.
2.00		0.836	0.660	86.2	2.320	95.5	712.	4190.	0.1700	3.333	0.300	190.
Table 5-7. Argon Propellant, Optimum Propellant Utilization, 10,000 sec.												
0.20		0.787	0.697	8.96	0.127	2.47	3215.	4019.	0.8000	2.009	0.183	414.
0.50		0.888	0.797	49.0	0.796	17.4	2525.	3156.	0.8000	1.578	0.242	288.
0.879		0.922	0.835	144.	2.460	55.9	2342.	2930.	0.7994	1.465	0.296	244.
1.0		0.925	0.838	174.	2.975	67.8	2327.	3333.	0.6982	1.667	0.324	241.
2.0		0.940	0.854	476.	8.290	191.	2258.	6667.	0.3387	3.333	0.532	224.
3.90		0.949	0.867	1263.	22.34	522.	2211.	13000.	0.1701	6.500	0.838	209.
5.0		0.941	0.859	1320.	23.12	536.	2249.	13228.	0.1700	8.333	1.186	215.
10.		0.913	0.830	1541.	26.09	587.	2389.	14052.	0.1700	16.67	3.154	238.
20.		0.874	0.793	1920.	31.07	669.	2607.	15334.	0.1700	33.33	8.134	265.
Table 5-8. Xenon Propellant, 0.5 m Beam Diameter, Optimum Propellant Utilization.												
	1000.	0.613	0.340	1.54	0.107	4.90	174.	1025.	0.1700	0.950	0.011	140.
	1500.	0.799	0.492	2.80	0.187	7.47	231.	1357.	0.1700	0.950	0.019	144.
	2000.	0.900	0.617	5.83	0.367	12.4	323.	1900.	0.1701	0.950	0.026	148.
	2500.	0.926	0.700	7.82	0.446	12.4	477.	1900.	0.2511	0.950	0.038	154.
	3000.	0.939	0.758	10.3	0.528	12.4	668.	1900.	0.3517	0.950	0.048	160.
	4000.	0.953	0.830	16.4	0.694	12.4	1153.	1900.	0.6069	0.950	0.068	170.
	4620.	0.959	0.858	21.0	0.796	12.4	1519.	1900.	0.7996	0.950	0.082	180.
	5000.	0.959	0.870	22.4	0.796	11.4	1779.	2224.	0.8000	1.112	0.091	183.
	6000.	0.960	0.891	26.3	0.796	9.54	2557.	3196.	0.8000	1.598	0.122	200.
	7000.	0.960	0.904	30.2	0.796	8.18	3480.	4350.	0.8000	2.175	0.155	217.
	8000.	0.960	0.912	34.2	0.796	7.16	4546.	5682.	0.8000	2.841	0.195	238.
	9000.	0.959	0.918	38.3	0.796	6.36	5765.	7206.	0.8000	3.603	0.231	258.
	10000.	0.958	0.922	42.4	0.796	5.71	7132.	8915.	0.8000	4.458	0.272	280.
Table 5-9. Xenon Propellant, 0.5 m Beam Diameter, 1500 sec.												
		0.50	0.407	8.97	0.496	12.4	589.	1900.	0.3101	0.950	0.003	135.
		0.60	0.450	6.75	0.413	12.4	409.	1900.	0.2153	0.950	0.004	136.
		0.65	0.467	6.01	0.381	12.4	349.	1900.	0.1835	0.950	0.005	137.
		0.675	0.474	5.70	0.367	12.4	323.	1900.	0.1701	0.950	0.006	137.
		0.75	0.489	3.63	0.241	9.03	262.	1540.	0.1700	0.950	0.011	140.
		0.799	0.492	2.80	0.187	7.47	231.	1537.	0.1700	0.950	0.019	144.
		0.85	0.487	2.21	0.146	6.21	204.	1199.	0.1700	0.950	0.034	152.
		0.90	0.461	1.85	0.116	5.23	182.	1070.	0.1700	0.950	0.073	173.
		0.93	0.415	1.81	0.102	4.74	170.	1002.	0.1700	0.950	0.144	211.
		0.95	0.332	2.07	0.0937	4.45	163.	960.	0.1700	0.950	0.316	303.
Table 5-10. Xenon Propellant, 0.5 m Beam Diameter, 3000 sec.												
		0.50	0.473	24.8	0.796	9.94	2356.	2946.	0.8000	1.473	0.003	136.
		0.55	0.514	22.8	0.796	10.9	1948.	2434.	0.8000	1.217	0.004	136.
		0.623	0.572	20.5	0.796	12.4	1518.	1900.	0.7989	0.950	0.004	136.
		0.75	0.662	14.7	0.661	12.4	1047.	1900.	0.5512	0.950	0.008	138.
		0.85	0.724	11.9	0.583	12.4	815.	1900.	0.4292	0.950	0.016	143.

Beam Diameter, m	Specific Impulse, sec	Propellant Utilization, η_u	Thruster Efficiency, η_t	Power, KW	Thrust, N	Beam Current, A	Net Voltage, ΔV_n, V	Total Voltage, ΔV_t, V	Voltage Ratio, R	Grid Gap ℓ_g, mm	Chamber Length, m	Discharge Loss, eV/ion
Table 5-10. Xenon Propellant, 0.5 m Beam Diameter, 3000 sec. (Continued)												
		0.90	0.748	10.8	0.551	12.4	727.	1900.	0.3828	0.950	0.026	148.
		0.93	0.757	10.4	0.553	12.4	681.	1900.	0.3585	0.950	0.041	156.
		0.939	0.758	10.3	0.528	12.4	668.	1900.	0.3517	0.950	0.048	160.
		0.95	0.756	10.2	0.522	12.4	653.	1900.	0.3436	0.950	0.063	168.
		0.97	0.732	10.3	0.511	12.4	626.	1900.	0.3295	0.950	0.129	203.
		0.98	0.675	11.0	0.506	12.4	613.	1900.	0.3228	0.950	0.268	277.
Table 5-11. Xenon Propellant, 0.5 m Beam Diameter, 10,000 sec.												
		0.80	0.788	49.5	0.796	4.77	10228.	12785.	0.8000	6.392	0.031	150.
		0.85	0.836	46.7	0.796	5.07	9060.	11325.	0.8000	5.662	0.043	157.
		0.90	0.881	44.3	0.796	5.37	8081.	10102.	0.8000	5.051	0.070	172.
		0.93	0.907	43.1	0.796	5.55	7568.	9460.	0.8000	4.730	0.114	195.
		0.95	0.920	42.4	0.796	5.67	7253.	9066.	0.8000	4.533	0.195	238.
		0.958	0.922	42.4	0.796	5.71	7132.	8915.	0.8000	4.458	0.272	280.
		0.96	0.922	42.4	0.796	5.73	7103.	8878.	0.8000	4.439	0.302	296.
		0.97	0.905	43.1	0.796	5.79	6957.	8696.	0.8000	4.348	0.675	496.
Table 5-12. Xenon Propellant, Optimum Propellant Utilization, 1500 sec.												
0.20		0.744	0.477	0.615	0.0399	1.48	266.	1565.	0.1700	0.950	0.011	149.
0.30		0.769	0.484	1.19	0.0786	3.02	249.	1465.	0.1700	0.950	0.014	147.
0.40		0.787	0.489	1.92	0.127	5.00	238.	1399.	0.1700	0.950	0.017	145.
0.50		0.799	0.492	2.80	0.187	7.47	231.	1357.	0.1700	0.950	0.019	144.
0.57		0.807	0.494	3.48	0.224	9.42	226.	1330.	0.1700	0.950	0.020	143.
0.70		0.795	0.491	3.72	0.248	9.86	233.	1371.	0.1700	1.167	0.027	144.
1.0		0.774	0.485	4.19	0.276	10.7	246.	1446.	0.1700	1.667	0.046	146.
1.5		0.749	0.478	4.85	0.315	11.8	263.	1544.	0.1700	2.500	0.083	149.
2.0		0.730	0.472	5.44	0.349	12.7	276.	1626.	0.1700	3.333	0.125	151.
Table 5-13. Xenon Propellant, Optimum Propellant Utilization, 3000 sec.												
0.20		0.900	0.725	1.79	0.0881	1.98	727.	1900.	0.3828	0.950	0.031	176.
0.30		0.920	0.741	3.85	0.194	4.46	696.	1900.	0.3663	0.950	0.038	168.
0.40		0.931	0.751	6.68	0.341	7.92	680.	1900.	0.3577	0.950	0.043	163.
0.50		0.939	0.758	10.3	0.528	12.4	668.	1900.	0.3517	0.950	0.048	160.
0.57		0.943	0.761	13.2	0.683	16.1	662.	1900.	0.3487	0.950	0.052	158.
0.60		0.944	0.762	14.2	0.737	17.4	661.	2000.	0.3305	1.000	0.054	158.
0.70		0.946	0.764	17.8	0.927	21.9	658.	2333.	0.2821	1.167	0.060	157.
0.80		0.948	0.766	21.7	1.130	26.7	656.	2667.	0.2458	1.333	0.066	156.
1.0		0.951	0.768	30.1	1.574	37.4	651.	3333.	0.1954	1.667	0.078	155.
1.145		0.953	0.770	36.8	1.924	45.8	649.	3816.	0.1700	1.908	0.087	154.
1.5		0.943	0.764	38.6	2.007	47.3	662.	3897.	0.1700	2.500	0.119	155.
2.0		0.934	0.757	40.5	2.085	48.6	675.	3972.	0.1700	3.333	0.179	158.
Table 5-14. Xenon Propellant, Optimum Propellant Utilization, 10,000 sec.												
0.30		0.938	0.899	15.6	0.287	2.01	7440.	9300.	0.8000	4.650	0.215	326.
0.50		0.958	0.922	42.4	0.796	5.71	7132.	8915.	0.8000	4.458	0.272	280.
0.70		0.967	0.933	82.0	1.561	11.3	7000.	8750.	0.8000	4.375	0.315	255.
1.0		0.974	0.942	116.	3.185	23.2	6900.	8625.	0.8000	4.310	0.364	231.
1.5		0.981	0.951	370.	7.166	52.7	6802.	8502.	0.8000	4.251	0.468	218.
2.0		0.984	0.955	654.	12.74	93.9	6760.	8451.	0.8000	4.225	0.520	204.
2.52		0.986	0.958	1035.	20.23	149.	6733.	8416.	0.8000	4.208	0.567	194.
3.0		0.987	0.959	1343.	26.27	194.	6719.	10000.	0.6719	5.000	0.662	193.
5.0		0.989	0.962	2875.	56.41	418.	6692.	16667.	0.4015	8.333	0.977	186.
7.0		0.990	0.964	4749.	93.35	692.	6679.	23333.	0.2862	11.67	1.239	181.
11.76		0.991	0.966	10308.	203.1	1507.	6665.	39200.	0.1700	19.60	1.701	173.
15.0		0.990	0.964	10374.	203.9	1512.	6679.	39287.	0.1700	25.00	2.587	180.
20.0		0.988	0.961	15075.	205.6	1522.	6706.	39446.	0.1700	33.33	3.940	187.

In Figs. 5-1 and 5-8, performance is shown over a range of specific impulse for a thruster with a 0.5 m beam diameter. At each specific impulse the propellant utilization was iterated to the nearest 0.001 to maximize thruster efficiency. The beam diameter of 0.5 m is large, but not so large that the minimum grid spacing is increased above 0.95 m due to span-to-gap ratio. The maximum efficiency also required that the ion optics for each specific impulse be optimized, although this optimization did not require any iteration.

Optimized in this manner, the data of Figs. 5-1 and 5-8 show the minimum net-to-total voltage ratio, R, at low specific impulses, the maximum of 0.8 at high specific impulses, and intermediate values between the two regions. At low specific impulses (below about 2000 sec for Ar and below about 3000 sec for Xe), the minimum spacing of 0.95 mm is used, but the screen-accel electric field is less than the maximum of 2000 V/mm. The use of the minimum permissible R is necessary to obtain maximum beam current which, in view of neutral-loss theory, is required to obtain maximum utilization and thruster efficiencies.

In the intermediate specific impulse range (about 3000 to 7770 sec for Ar and about 2000 to 4620 sec for Xe), the maximum beam current is obtained by keeping the minimum gap dictated by the span-to-gap ratio and decreasing total voltage to agree with the electric field limit. This conclusion can be shown by Child's law, with current varying as $\Delta V_t^{3/2}/\ell_e^2$. Using a gap larger than the minimum, while maintaining maximum electric field, will result in ℓ_e^2 increasing more than $\Delta V_t^{3/2}$, thus decreasing maximum current. With the gap fixed at the minimum and the electric field at the maximum, the extracted ion current is also a constant in this specific impulse range (see Figs. 5-1(b) and 5-8(b)).

In the high specific impulse range (above about 7770 sec for Ar and about 4620 sec for Xe), the net voltage is so high that R will increase above the backstreaming limit if the gap is maintained at the minimum value. The maximum beam current in this range is obtained by increasing the gap (at maximum electric field) until the total voltage, with the calculated net voltage, corresponds to the maximum permissible R. This region also corresponds to constant thrust (see Figs. 5-1(c) and 5-8(c)). In a space-charge-limited condition the electric field force at the accelerator corresponds to the time-rate-of-change of charged particle momentum between the emitter and the accelerator. With constant electric field, then, the thrust force at the accelerator is constant. With R also constant, a constant fraction of this thrust appears as thrust after deceleration.

Although the number of grids is not indicated, three grid ion optics are assumed for any R below 0.7. In the R range from 0.7 to 0.8, either two or three grid optics could be used.

The thrust-to-power ratio (see Figs. 5-1(d) and 5-8(d)) generally rises as specific impulse is reduced, which one would expect from the reduced kinetic energy requirements of lower specific impulses. What is less obvious is the leveling off of thrust-to-power ratio at low specific impulses. For a constant discharge loss and a constant propellant utilization, the thrust-to-power ratio will actually show a maximum at a net voltage equal to the discharge loss in eV/ion (power efficiency of 0.5). The optimization of propellant utilization used herein prevents this maximum from being evident. As the specific impulse is decreased below the value where this maximum might be expected, the optimization procedure selects increasingly lower propellant utilizations. For example, argon at 1500 sec gives a optimum propellant

utilization of 0.454, while xenon at 1000 sec gives 0.613. The thrust-to-power ratio rises slightly at these low specific impulses because the low utilizations are obtained by using very shallow discharge chambers which, in turn, give very low discharge losses. For argon at 1500 sec the 0.5 m diameter chamber has a depth of only 2 cm, while for xenon at 1000 sec the depth is only 1.1 cm.

Optimum operation at very low specific impulses is, in effect, obtained by operating at near optimum electrical values and throwing away increasing fractions of non-ionized propellant as specific impulse is decreased. Such operation will generally not be of interest in mission analysis. If such operation does appear to be preferred, it usually indicates that a stage mismatch exists. That is, overall performance would be increased by using a smaller mass for the electric propulsion stage and operating the thruster at a high specific impulse. Such a mismatch may exist in any case where a thruster efficiency less than about 0.5 is indicated as being desirable.

The effects of variations of propellant utilization about the optimum values are shown in Figs. 5-2 through 5-4 for argon and Figs. 5-9 through 5-11 for xenon. In the low specific impulse range (R = 0.17 at optimum utilization), shown in Figs. 5-2 and 5-9, relatively large departures from optimum propellant utilization cause small decreases from maximum thruster efficiency. The fact that the optimization was for thruster efficiency, not thrust, is clearly indicated by Figs. 5-2(b) and 5-9(b). Small decreases in thruster efficiency from maximum can be exchanged for relatively large increases in thrust. These thrust increases correspond to operating at higher net and total voltages, so that the increased thrusts result from the increased

current capacities of the ion optics at the higher voltages. At a sufficiently low propellant utilization, the total voltage can reach the maximum electric field value and the R must increase above 0.17. Although shown only for xenon, the same change in R occurs at lower propellant utilization than covered in Fig. 5-2 for argon.

The effect of varying propellant utilization away from optimum has a more pronounced effect on thruster efficiency at higher specific impulses, as shown in Figs. 5-3, 5-4, 5-10, and 5-11. Decreasing propellant utilization from the optimum value increases thrust slightly in the intermediate specific impulse range (Figs. 5-3 and 5-10), and not at all in the high specific impulse range (Figs. 5-4 and 5-11).

The effects of varying thruster diameter are shown in Figs. 5-5 through 5-7 and Figs. 5-12 through 5-14. All data shown in these figures were optimized for maximum thruster efficiency at each thruster diameter. As with the effect of propellant utilization variations, the nature of diameter effects depend on the specific impulse range under consideration.

At the lowest specific impulses, Figs. 5-5 and 5-12, the grid gap remains at the 0.95 mm value until a beam diameter of 0.57 m is reached. Above this diameter, the span-to-gap limit required that the gap be increased proportionally with the diameter. The effect on thrust can best be understood by first ignoring the effect of propellant utilization changes. For beam diameters less than 0.57 m, the grid gap is fixed at 0.95 mm and the thrust per unit area should be constant at constant specific impulse. At beam diameters larger than 0.57 m, all ion optics dimensions are increased in proportion to the beam diameter.

At constant propellant utilization, the voltages would again be constant. A classic space-charge-flow calculation has shown that beam current (and thrust) are independent of ion optics size when all dimensions are changed in proportion with voltages held constant.

We will now include the additional effects of changing propellant utilization. As beam diameter is decreased from 0.57 m, the primary electron region volume-to-area ratio, Ω_p/A_p, tends to decrease. (A_o also decreases, but beam current also decreases about the same amount, leaving little net effect of A_o and beam current on propellant utilizations.) This tendency to decrease Ω_p/A_p can be partially offset by an increase in discharge chamber L/D. But, because an increase in L/D also results in an increase in discharge losses, the increase in L/D must be a compromise between maintaining propellant utilization and increasing discharge losses. This compromise results in a net decrease in optimized thruster efficiency. There is also a net loss in propellant utilization as beam diameter is decreased below 0.57 m. This loss results in increases in net and total voltages, which are the cause of the increased thrust-to-beam area ratio as beam diameter is decreased.

When beam diameter is increased above 0.57 m, the ratio Ω_p/A_p tends to increase. But this is more than offset by the increase in A_o, which increases with the beam diameter squared. But with beam current tending to remain constant as beam diameter is increased, the propellant utilization must suffer a net decrease. This net decrease, in turn, results in a decrease in optimized thruster efficiency as beam diameter is increased above 0.57 m.

Maximum thruster efficiency (all beam diameters) in the low specific impulse range thus corresponds to the maximum beam diameter

for which the minimum grid gap can be maintained. The thruster mass has not been discussed, but it normally increases somewhat less rapidly than beam area.[11] It appears that maximum thrust-to-weight ratio would also be found at a beam diameter of 0.57 m. Further, the mass penalty for going above 0.57 m appears to be substantial. Large thrust applications in this specific impulse range thus strongly indicate the use of the maximum beam diameter consistent with the minimum grid gap.

The tradeoffs are slightly different for beam diameter variations in the intermediate specific impulse range (Figs. 5-6 and 5-13). Above a beam diameter of 0.57 m, the grid gap again increased above the 0.95 mm value. The freedom to decrease R as the grid gap is increased, though, more than offsets any thruster efficiency loss that might be expected from the grid gap increase. The efficiency tradeoff shifts when the R is decreased to 0.17, in that further diameter increases result in a net loss in optimized thruster efficiency, as well as a rapid loss in thrust-to-beam area ratio.

The variation in thrust-to-mass ratio is probably not great in the diameter range with $\ell_g > 0.95$ mm and R>0.17. The need for both maximum thruster efficiency and minimum parts count (for increased reliability and reduced cost) would thus indicate a beam diameter for large thrust systems such that an R of 0.17 is just reached. That is, the beam diameter is such that the grid gap (from the span-to-gap limit) corresponds simultaneously to maximum electric field and an R of 0.17.

Except for having a region with R = 0.8, the qualitative effects of varying beam diameter in the high specific impulse range (Figs. 5-7 and 5-14) are similar to the effects described above. Again the optimum beam diameter appears to correspond to maximum electric field and

an R of 0.17 at a grid gap given by the span-to-gap limit. The optimum beam diameter at 10000 sec, however, is quite large - 3.90 m for argon and 11.76 m for xenon. The power levels are even larger for this optimum beam diameter - 1.26 MW for argon and 10.31 MW for xenon.

Conclusions

Much of the significance of the large thruster analysis presented herein lies in the specific performance values obtained. These values are adequately presented in the various figures and tables that have been included and need not be repeated here. There are other significant results, however, that may not be as obvious.

One result was the extremely shallow depths obtained for optimum discharge chambers. At 5000 sec, for example, the optimum depths for 0.5-m diameter chambers were less than 10 cm for both argon and xenon. At lower specific impulses the optimum chamber depths were even less than 10 cm. The analysis of propellant utilization effects indicates that small increases in depth from the optimum value will result in even smaller losses in efficiency. Even so, the optimum depths are well below what might be expected without detailed analysis. Only at specific impulses approaching 10,000 sec do the length-to-diameter ratios of the discharge chambers approach values normally expected.

The distribution of electrons to a chamber with an L/D of 0.2, or less, is another aspect that deserves mention. Obtaining a uniform distribution of primaries from a single baffle annulus is probably beyond present technology even if multiple cathodes are used to provide more uniform current from a single annulus.

The effect of beam diameter on thruster performance was examined at low, intermediate, and high specific impulses. The optimum choice

of beam diameter for very large systems was indicated for these three ranges. The optimum choice of beam diameter can also be described in terms of simultaneously satisfying multiple limits. These limits are minimum net-to-total voltage ratio, maximum span-to-gap ratio, and either minimum gap or maximum electric field. Further examination of these limits should obviously be considered in future technology studies.

The size, power, and efficiency limits indicated by this study are clearly much more restrictive at low specific impulses. Alternatives to "conventional" discharge chambers and ion optics could offer substantial advantages at these low specific impulses, and should therefore be considered.

VI. CONCLUDING REMARKS

The recent progress in understanding electron diffusion across a magnetic field has been substantial. The basic model that is associated with this progress is a two-step one in which the first step is density-gradient driven and the second step (if any) encompasses the potential difference. In electron diffusion to anodes, presented herein, the second step consists of single-particle escape orbits. If the diffusion is to a downstream region of substantial plasma density, as is the case for diffusion through a baffle gap to a discharge chamber, then constant-density diffusion should be used for this second step, with the constant density at the value required for the downstream region.[1]

The production of doubly charged ions has been correlated using parameters derived from a previous comprehensive approach that required detailed knowledge of plasma properties.[2] The correlation presented herein should find wider use in that only overall performance parameters are used. The use of this correlation is therefore possible in even the design stage, where detailed plasma properties cannot be available.

In argon hollow cathode tests, a noisy high voltage mode was found at high emission currents. Although this mode has some similarities to the plume mode, it is encountered by initially being in the spot mode and increasing emission. No similar high current mode has been observed with mercury propellant. It is suspected that the low collision cross section of inert gases at the electron temperatures of interest is involved in the occurrence of this mode with argon. This mode also serves to limit the maximum ratio of electron emission to propellant flow rate. Inasmuch as similar discharge voltage increases have been observed at high emissions with xenon, it is expected that a similar

noisy mode will also be found with xenon. An enclosed keeper has been found to increase maximum cathode emission over open keeper designs for a given argon flow.

A detailed analysis of large inert gas thruster performance was carried out using both the results of previous inert gas investigations and more general ion optics studies. The results are presented in both tabular and graphical form. For maximum thruster efficiency at most specific impulses, the optimum beam diameter corresponds to simultaneously satisfying maximum span-to-gap ratio, maximum electric field, and minimum net-to-total voltage ratio. At low specific impulses, the optimum beam diameter corresponds to simultaneously satisfying maximum span-to-gap ratio, minimum interelectrode spacing, and minimum net-to-total voltage ratio. The optimum beam diameter and power level, as defined above, change drastically with specific impulse, ranging from less than a meter at 2000 sec to several meters at 10,000 sec, and from a few kilowatts to megawatts for the same specific impulse range. A general result of the analysis that should be noted is the small optimum chamber depth for these large diameter thrusters. The length-to-diameter ratio was typically under 0.2, so that a uniform distribution of primary electrons might be difficult to obtain from a single baffle annulus. It should be kept in mind that the various limits used in the analysis are reasonable by today's technology standards, but may be revised by future developments. For example, thermal expansion is intimately involved in the present limit for span-to-gap ratio. If a grid set were designed to come into alignment only after a warmup period with no high voltage applied, it might be possible to substantially increase the maximum span-to-gap ratio.

REFERENCES

Section I

1. Kaufman, H. R.; "Inert Gas Thrusters," NASA Contr. Rep., CR-159527, Nov. 1978.

2. Kaufman, H. R. and Robinson, R. S.; "Plasma Processes in Inert Gas Thrusters," AIAA Paper, No. 79-2055, Oct./Nov. 1979.

3. Wilbur, P. J.; "Argon-Xenon Discharge Chamber Model for the Production of Doubly Charged Ions," Inert Gas Thrusters (H. R. Kaufman, ed.); NASA Contr. Rep., CR-135226, July 1977.

Section II

1. Bohm, D., Burhop, E. H. S., and Massey, H. S. W.; "The Use of Probes for Plasma Exploration in Strong Magnetic Fields," in The Characteristics of Electrical Discharges in Magnetic Fields (A. Guthrie and R. K. Wakerling, eds.); McGraw-Hill Book Co., 1949, pp. 13-76.

2. Brophy, J. R. and Wilbur, P. J.; "Electron Diffusion through the Baffle Aperture of a Hollow Cathode Thruster," AIAA Paper, No. 79-2060 (1979).

3. Kaufman, H. R.; Experimental Investigations of Argon and Xenon Ion Sources; NASA CR-134845, June 1975.

4. Isaacson, G. C. and Kaufman, H. R.; "15-cm Multipole Gas Ion Thruster," J. Spacecr. Roc., Vol. 14, pp. 469-473 (1977).

5. Isaacson, G. C.; Multipole Gas Thruster Design; NASA CR-135101, June 1977.

6. Robinson, R. S. and Kaufman, H. R.; "Ion Thruster Technology Applied to a 30-cm Multipole Sputtering Ion Source," AIAA Journal, Vol. 15, pp. 702-706 (May 1977).

7. Ramsey, W. D.; "12-cm Argon/Xenon Ion Source," J. Spacecr. Roc., Vol. 16, pp. 252-257 (July-August 1979).

8. Kaufman, H. R.; "Inert Gas Thrusters," NASA Contr. Rep., CR-159527, Nov. 1978, pp. 10-27.

9. Spitzer, L., Jr.; Physics of Fully Ionized Gases, 2nd ed.; Interscience Publishers, N. Y., 1962, pp. 47-48.

10. Chen, F. F.; Introduction to Plasma Physics; Plenum Press, N. Y., 1974, p. 169.

11. Robinson, R. S.; "Plasma Probe Measurements in the 30-cm Discharge Chamber," in Industrial Ion Source Technology, (H. R. Kaufman, ed.); NASA Contr. Rep. CR-135353, Nov. 1977, pp. 3-17.

12. Robinson, R. S.; "Thirty cm Ion Source," in Industrial Ion Source Technology, (H. R. Kaufman, ed.), NASA Contr. Rep. CR-135149, Nov. 1976, pp. 1-59.

13. Isaacson, G. C.; "Multipole Gas Thruster Design," NASA Contr. Rep. CR-135101, June 1977, pp. 45-51.

14. Haynes, C. M.; "Fifteen cm Ion Source," in Industrial Ion Source Technology, (H. R. Kaufman, ed.), NASA Contr. Rep. CR-135353, Nov. 1977, pp. 18-23.

15. Kaufman, H. R.; "Charge-Exchange Plasma Generated by an Ion Thruster," NASA Contr. Rep. CR-135318, Dec. 1977.

16. Chen, F. F.; Introduction to Plasma Physics; Plenum Press, N. Y., pp. 165-173.

17. Robinson, R. S.; Physical Processes in Directed Ion Beam Sputtering; NASA CR-159567, March 1979, Appendix A.

18. Moore, R. D.; "Magneto-Electrostatically Contained Plasma Ion Thruster," AIAA Paper No. 69-620 (1969).

19. Ramsey, W. D.; "12-cm Magneto-Electrostatic Containment Mercury Ion Thruster Development," J. Spacecr. Roc., Vol. 9, pp. 318-321 (1972).

20. Wilbur, P. J.; NASA Contr. Rep. CR-159784, Dec. 1979.

Section III

1. Peters, R. R.; "Double Ion Production in Mercury Thrusters," NASA Contr. Rep. CR-135019, April 1976.

2. Wilbur, P. J.; "Inert Gas Thrusters," (H. R. Kaufman, ed.); NASA Contr. Rep. CR-135226, July 1977, pp. 46-64.

3. Wilbur, P. J. and Kaufman, H. R.; "Scaling Relationships for Mercury and Gaseous Propellant Ion Thrusters," AIAA Paper 78-667, April 1978.

4. Isaacson, G. C.; "Multipole Gas Thruster Design," NASA Contr. Rep. CR-135101, June 1977.

5. Robinson, R. S.; in "Industrial Ion Source Technology," NASA Contr. Rep. CR-135353, Nov. 1977, pp. 3-23.

6. Rehn, L. A.; in "Inert Gas Thrusters," (H. R. Kaufman, ed.), NASA Contr. Rep. CR-159527, Nov. 1978, pp. 33-49.

7. Ramsey, W. D.; "12-cm Magneto-Electrostatic Containment Mercury Ion Thruster Development," J. Space. Rockets, Vol. 9, May 1972, pp. 318-321.

Section IV

1. Siegfried, D. E. and Wilbur, P. J.; "An Investigation of Mercury Hollow Cathode Phenomena," AIAA Paper No. 78-705, April 25-27, 1978.

2. Siegfried, D. and Wilbur, P. J.; "Studies on an Experimental Quartz Tube Hollow Cathode," AIAA Paper No. 79-2056, Oct. 30-Nov. 1, 1979.

3. Delacroix, Jean-Loup and Trinade, Armando Rocha; "Hollow Cathode Arcs," in Advances in Electronics and Electron Physics, (L. Martin, ed.) Vol. 35; Academic Press, N. Y., 1974.

Section V

1. Isaacson, G. C.; "Multipole Gas Thruster Design," NASA Contr. Rep. CR-135101, June 1977.

2. Clausing, P.; Ann. Phys. (Leipzig), Vol. 12, pp. 961-989 (1932).

3. Kaufman, H. R.; "Technology of Electron-Bombardment Ion Thrusters," in Advances in Electronics and Electron Physics (L. Marton, ed.), Vol. 36; Academic Press, N. Y. (1974).

4. Rawlin, V. K., Banks, B. A., and Byers, D. C.; J. Spacecr. Rockets, Vol. 10, pp. 29-35 (1973).

5. Rawlin, V. K.; AIAA Paper No. 73-1086 (1973).

6. Aston, G., Kaufman, H. R., and Wilbur, P. J.; "Ion Beam Divergence Characteristics of Two-Grid Accelerator Systems," AIAA J. Vol. 16, pp. 516-524, May 1978.

7. Aston, G. and Kaufman, H. R.; "The Ion Optics of a Two-Grid Electron-Bombardment Thruster," AIAA Paper No. 76-1029, Nov. 1976.

8. Wilbur, P. J. and Kaufman, H. R.; "Sealing Relationships for Mercury and Gaseous Propellant Ion Thrusters," AIAA Paper No. 78-667, April 1978.

9. Kaufman, H. R.; "Accelerator System Solutions for Broad-Beam Ion Sources," AIAA J., Vol. 15, pp. 1025-1034, July 1977.

10. Aston, G. and Kaufman, H. R.; "Ion Beam Divergence Characteristics of Three-Grid Accelerator Systems," AIAA J., Vol. 17, pp. 64-70, Jan. 1979.

11. Kaufman, H. R.; "Inert Gas Thrusters," NASA Contr. Rep. CR-135100, July 1976.

Section VI

1. Wilbur, P. J.; NASA CR-159784, December 1979.

2. Wilbur, P. J.; "Argon-Xenon Discharge Chamber Model for the Production of Doubly Charged Ions," in Inert Gas Thrusters (H. R. Kaufman, ed.), NASA Contr. Rep. CR-135226, July 1977.

DISTRIBUTION LIST

	No. of Copies
National Aeronautics and Space Administration Washington, DC 20546	
Attn: RPE/Mr. Wayne Hudson	1
Mr. Daniel H. Herman, Code SL	1
National Aeronautics and Space Administration Lewis Research Center 21000 Brookpark Road Cleveland, OH 44135	
Attn: Research Support Procurement Section	
Mr. L. Light, MS 500-306	1
Technology Utilization Office, MS 3-19	1
Report Control Office, MS 5-5	1
Library, MS 60-3	2
N. T. Musial, MS 600-113	1
Spacecraft Propulsion & Power Division, MS 501-7	
Dr. F. Teren	1
Mr. R. Finke	1
Mr. D. Byers	1
Mr. B. Banks	1
Mr. N. Grier	1
Mr. F. Terdan	1
Mr. W. Kerslake	20
Mr. V. Rawlin	1
Chief Scientist, MS 3-12	1
Dr. M. Goldstein	1
National Aeronautics and Space Administration Marshall Space Flight Center Huntsville, AL 35812	
Attn: Mr. Jerry P. Hethcoate	1
Mr. John Harlow	1
NASA Scientific and Technical Information Facility P. O. Box 8757 Baltimore/Washington International Airport Baltimore, MD 21240	40
Case Western Reserve University 10900 Euclid Avenue Cleveland, OH 44106	
Attn: Dr. Eli Reshotko	1
Royal Aircraft Establishment Space Department Farnborough, Hants, ENGLAND	
Attn: Dr. D. G. Fearn	1

NASA JSC
Houston, TX 77058
Attn: Mr. H. Davis 1

United Kingdom Atomic Energy Authority
Culham Laboratory
Abingdom, Berkshire, ENGLAND
Attn: Dr. P. J. Harbour 1
Dr. M. F. A. Harrison 1
Dr. T. S. Green 1

National Aeronautics and Space Administration
Goddard Space Flight Center
Greenbelt, MD 20771
Attn: Mr. W. Isley, Code 734 1
Mr. A. A. Yetman 1
Dr. D. H. Suddeth 1

SAMSO
Air Force Unit Post Office
Los Angeles, CA 90045
Attn: Capt. D. Egan/ SYAX 1

Comsat Laboratories
P. O. Box 115
Clarksburg, MD 20734
Attn: Mr. B. Free 1
Mr. O. Revesz 1

Roket Propulsion Laboratory
Edwards AFB, CA 93523
Attn: LKDA/Mr. Tom Waddell 1
LKDH/Dr. R. Vondra 1

DFVLR - Institut für Plasmadynamik
Technische Universitat Stuttgart
7 Stuttgart-Vaihingen
Allmandstr 124
WEST GERMANY
Attn: Dr. G. Krülle 1

Giessen University
1st Institute of Physics
Geissen, WEST GERMANY
Attn: Professor H. W. Loeb 1

Jet Propulsion Laboratory
4800 Oak Grove Drive
Pasadena, CA 91102
Attn: Dr. Kenneth Atkins 1
Technical Library 1
Mr. Eugene Pawlik 1
Dr. Graeme Aston 1
Dr. Kevin Rudolph 1

Electro-Optical Systems, Inc.
300 North Halstead
Pasadena, CA 91107
Attn: Mr. R. Worlock 1
Mr. E. James 1
Mr. W. Ramsey 1

Boeing Aerospace Company
P. O. Box 3999
Seattle, WA 98124
Attn: Mr. Donald Grim 1
Mr. Russel Dod 1

Lockheed Missiles and Space Company
Sunnyvale, CA 94088
Attn: Dr. William L. Owens
Propulsion Systems, Dept. 62-13 1
Mr. Carl Rudey 1

Fairchild Republic Company
Farmingdale, NY 11735
Attn: Dr. William Guman 1

COMSAT Corporation
950 L'Enfant Plaza S.W.
Washington, DC 20024
Attn: Mr. Sidney O. Metzger 1

Electrotechnical Laboratory
Tahashi Branch
5-4-1 Mukodai-Machi, Tanashi-Shi
Tokyo, JAPAN
Attn: Dr. Katsuva Nakayama 1

Office of Assistant for Study Support
Kirtland Air Force Base
Albuquerque, NM 87117
Attn: Dr. Calvin W. Thomas OAS Ge 1
Dr. Berhart Eber OAS Ge 1

Bell Laboratories
600 Mountain Avenue
Murray Hill, NJ 07974
Attn: Dr. Edward G. Spencer 1
Dr. Paul H. Schmidt 1

Massachusetts Institute of Technology
Lincoln Laboratory
P. O. Box 73
Lexington, MA 02173
Attn: Dr. H. I. Smith 1

Sandia Laboratories
Mail Code 5742
Albuquerque, NM 87115
Attn: Mr. Ralph R. Peters 1

TRW, Inc.
TRW Systems
One Space Park
Redondo Beach, CA 90278
Attn: Dr. M. Huberman 1
Mr. H. Ogawa 1
Mr. S. Zafran 1

National Aeronautics and Space Administration
Ames Research Center
Moffett Field, CA 94035
Attn: Technical Library 1

National Aeronautics and Space Administration
Langley Research Center
Langley Field Station
Hampton, VA 23365
Attn: Technical Library 1

Hughes Research Laboratories
3011 Malibu Canyon Road
Malibu, CA 90265
Attn: Dr. J. Hyman 1
Mr. J. H. Molitor 1
Dr. R. L. Poeschel 1
Mr. R. Vahrenkamp 1
Dr. John R. Beattie 1
Dr. W. S. Williamson 1

United States Air Force
Office of Scientific Research
Washington, DC 20025
Attn: Mr. M. Slawsky 1

Princeton University
Princeton, NJ 08540
Attn: Dean R. G. Jahn 1
Dr. K. E. Clark 1

Joint Institute for Laboratory Astrophysics
University of Colorado
Boulder, CO 80302
Attn: Dr. Gordon H. Dunn 1

Service du Confinement des Plasma
Centre d'Etudes Nucléaires - F.A.R.
B. P. 6
92260 Fontenay-aux-Roses
FRANCE
Attn: Dr. J. F. Bonal 1

International Business Machines Corporation
Thomas J. Watson Research Center
P. O. Box 218
Yorktown Heights, NY 10598
Attn: Dr. Jerome J. Cuomo 1
Dr. James M. E. Harper 1

IBM East Fishkill
D/42K, Bldg. 300-40F
Hopewell Junction, NY 12533
Attn: Dr. Charles M. McKenna 1

DFVLR-Forschungszentrum Braunschweig
Inst. A, Flughafen
3300 Braunschweig
WEST GERMANY
Attn: Dr. H. A. W. Bessling 1

Ion Beam Equipment, Inc.
P. O. Box O
Norwood, NJ 07648
Attn: Dr. W. Laznovsky 1

Optic Electronics Corporation
11477 Pagemill Road
Dallas, TX 75243
Attn: Bill Hermann, Jr. 1

Circuits Processing Apparatus, Inc.
725 Kifer Road
Sunnyvale, CA 94086
Attn: Spencer R. Wilder 1

Ion Tech, Inc.
1807 E. Mulberry
P. O. Box 1388
Fort Collins, CO 80522
Attn: Dr. Gerald C. Isaacson 1

Physicon Corporation
221 Mt. Auburn Street
Cambridge, MA 02138
Attn: H. von Zweck 1

Commonwealth Scientific Corporation
500 Pendleton Street
Alexandria, VA 22314
Attn: George R. Thompson 1

Veeco Instruments Inc.
Terminal Drive
Plainview, NY 11803
Attn: Norman Williams 1

CVC Products
525 Lee Road
P. O. Box 1886
Rochester, N.Y. 14603
Attn: Mr. Georg F. Garfield, Jr. 1